

December 2020

Developing Highly Reversible Li Metal Anode with Mossy/ Dendritic Li Suppression in High Energy Density Batteries

Xi Chen
University of Wisconsin-Milwaukee

Follow this and additional works at: <https://dc.uwm.edu/etd>



Part of the [Materials Science and Engineering Commons](#), and the [Oil, Gas, and Energy Commons](#)

Recommended Citation

Chen, Xi, "Developing Highly Reversible Li Metal Anode with Mossy/Dendritic Li Suppression in High Energy Density Batteries" (2020). *Theses and Dissertations*. 2478.
<https://dc.uwm.edu/etd/2478>

This Dissertation is brought to you for free and open access by UWM Digital Commons. It has been accepted for inclusion in Theses and Dissertations by an authorized administrator of UWM Digital Commons. For more information, please contact open-access@uwm.edu.

DEVELOPING HIGHLY REVERSIBLE LI METAL ANODE WITH
MOSSY/DENDRITIC LI SUPPRESSION IN HIGH ENERGY
DENSITY BATTERIES

by
Xi Chen

A Dissertation Submitted in
Partial Fulfillment of the
Requirements for the Degree of

Doctor of Philosophy
in Engineering

at

The University of Wisconsin-Milwaukee

December 2020

ABSTRACT

DEVELOPING HIGHLY REVERSIBLE LI METAL ANODE WITH MOSSY/DENDRITIC LI SUPPRESSION IN HIGH ENERGY DENSITY BATTERIES

by Xi Chen

The University of Wisconsin-Milwaukee, 2020
Under the Supervision of Professor Junjie Niu

Lithium-ion battery technology has wide impact on our daily life. However, most of the commercial batteries with limited energy density are unable to meet the growing demand of electrical vehicles, portable electronic devices and other energy storage systems. Therefore, the development of new electrode materials with high energy density and reliable performance has become a critical mission for researchers. Particularly replacing graphite anode with Li metal is one of most viable approaches to break the limitation of energy density in batteries. Metallic lithium is one of the most promising anode materials, which has a high theoretical specific capacity of 3860 mAhg^{-1} and a low electrochemical potential of -3.04V versus the standard hydrogen electrode. however, the growth of mossy/dendritic Li that can induce internal short circuiting, is considered as the main safety concern. Another challenge is the uncontrollable solid electrolyte interphase (SEI) that leads to a low columbic efficiency and thus a poor cycling performance.

In this dissertation, the history and motivation of Li metal are discussed, and challenges in Li metal are stated. The characterizations of Li metal including the root cause of Li metal nucleation and dendrite growth are discussed. The current state of art of Li metal efforts including electrolyte engineering, interfacial engineering and 3D Li host configuration are reviewed. In main body of this dissertation, several Li pretreatment methods are explored to suppress the Li dendrite growing from the most primitive Li metal nucleation state. This dissertation also aims to explore the methods for stabilizing SEI of lithium metal anode in liquid electrolyte-based Li-ion batteries. Also, the interfacial evolution of metallic lithium between one typical solid-state electrolyte-LiPON was investigated. The following projects for developing highly reversible Li metal anode are introduced: (1) A mass controllable Li carbon fiber fabric (LiCFF) composites is developed, which displayed excellent Li dendrite suppression by reducing effective current density in 3D carbon fiber fabric configuration. This novel all-in-one LiCFF composite has low electrical resistivity of $1.1 \times 10^{-3} \Omega \text{ cm}$. The large surface area of porous carbon fiber combined with good electrical conductivity can reduce effective current density in 3D conductive host for mossy/dendritic Li suppression. The excellent interfacial Li^+/e^- transport provides low Li metal nucleation/growth energy barrier. (2) An inter-layer-calated thin Li metal MXene hybrid electrode was developed, which has significant improvement in battery capacity retention and dendrite suppression. The high surface area 2D lamination structure of MXene as a hybrid interlayer and intercalation Li storage host, which provides enough space for reliable Li plating/stripping by regulating the Li ion flux. The excellent electrical conductivity also reduces the effective local current density, thus leading to a homogenous Li deposition/dissolution and thin inorganic part of SEI conformation. (3) Electro-chemo-mechanical stable artificial pre-SEI on Li metal anode with enhanced cycling performance was developed via a facile drop coating

method. The artificial pre SEI has high uniformity nanoscale organic components, inorganic lithium compounds and local high concentration Li salt, thus leading to homogenous Li ion transport and enhanced mechanical stability to deal with the fracture caused by Li cycling volume expansion. (4) Thin film solid state electrolyte LiPON showed excellent stability and compatibility with Li metal. We revealed the interfacial evolution between Li metal anode and LiPON by using *in-situ* transmission electron microscope configuration. A thin 60 nm interfacial passivation layer was found to be stable under 5 V voltage, which exhibited high conductivity and excellent mechanical strength to suppress Li dendrite growth.

© Copyright by Xi Chen, 2020
All Rights Reserved

To
my parents

TABLE OF CONTENTS

LIST OF FIGURES	x
LIST OF TABLES	xiv
LIST OF ABBREVIATIONS	xv
ACKNOWLEDGEMENTS	xviii
CHAPTER 1 Introduction	1
1.1 Next generation high energy density batteries with 500 Wh/kg	1
1.2 History of Li metal anode	4
1.3 Challenges in Li metal anode	6
1.4 Characterizations of Li metal and SEI.....	13
1.4.1 Morphology of Li dendrites	13
1.4.2 Characterization of Li metal SEI	16
1.5 Current state of art in Li metal anode efforts	20
1.5.1 Electrolyte engineering	20
1.5.2 Interfacial engineering	25
1.5.3 Li hosts with 3D configuration	29
1.6 Rationale of Li metal modification	35
CHAPTER 2 Design Strategies and Preparation of Li Metal Anode with Dendrite Suppression, Stable Interface and Improved Cyclability	37
2.1 Introduction	37
2.2 A lithiotropic mass controllable conductive Li-carbon fiber fabrics (LiCFF) composites design	37
2.2.1 Design principle of LiCFF.....	37
2.2.2 LiCFF electrode preparation.	40
2.3 Rolling $Ti_3C_2T_x$ MXene into Ultrathin Li Metal: Inter-layer-calated Li (ILC-Li) Anode.....	42
2.3.1 Design principle of ILC-Li electrode.....	42
2.3.2 Fabrication of the ILC-Li electrode.	44
2.4 An electro-chemo-mechanical stable artificial pre SEI design for high performance Li metal	45
2.4.1 Design principle of reinforced artificial SEI coated Li metal.....	45
2.4.2 Fabrication of reinforced artificial pre SEI coated Li metal	47

CHAPTER 3: Multiscale Characterization of Modified Li Metal Anode with Dendrites Suppression and High Reversibility	49
3.1 Multiscale Characterization of LiCFF	49
3.1.1 Mutiscale characterization of pristine LiCFF	49
3.1.2 Morphology evolution of LiCFF after Li plating/stripping	53
3.2 Multiscale characterization of ILC-Li.....	58
3.2.1 Morphology of MXene and pristine ILC-Li	58
3.2.2 Mechanism of inter-layer-calation.....	60
3.2.3 Morphology evolution of ILC-Li electrode	63
3.2.4 X-ray photoelectron spectroscopy characterization of SEI in ILC-Li and Li foil	66
3.3 Characterization of reinforced artificial pre SEI-Li.....	70
3.3.1 Reaction of ACN and Li metal	70
3.3.2 Composition characterization of reinforced artificial pre SEI.....	73
3.3.3 Morphology evolution of reinforced artificial pre SEI	76
3.4 Experimental details	79
3.4.1 Experimental details of LiCFF characterization.....	79
3.4.2 Experimental details of ILC-Li characterizations.....	80
4.4.3 Experimental details of reinforced artificial pre SEI characterization.....	81
3.5 Discussion.....	83
CHAPTER 4: Electrochemical Performance of Modified Li Metal Anode with Dendrites Suppression and High Reversibility	85
4.1 Electrochemical performance of LiCFF electrode.....	85
4.1.1 Electrochemical stability of LiCFF in symmetric cell.....	85
4.1.2 Full cell performance of LiCFF/NMC 622 and LiCFF-Sulfur batteries.....	90
4.2 Electrochemical characterization and batteries performance of ILC-Li	93
4.2.1 Electrochemical stability of ILC-Li.....	93
4.2.2 Full batteries performance of ILC-Li paired with NMC 532	96
4.2.3 Full batteries performance of ILC-Li paired with NCA under lean electrolyte condition	98
4.3 Electrochemical performance of reinforced artificial pre SEI-Li metal anode	101
4.3.1 Electrochemical stability.....	101
4.3.2 Batteries performance under lean electrolyte condition	103

4.4 Experimental details	106
4.4.1 Experimental details of LiCFF electrochemical performance.	106
4.4.2 Experimental details of ILC-Li.	107
4.4.3 Experimental details of reinforced artificial pre SEI	109
4.5 Conclusion.....	111
CHAPTER 5 Li Metal-LiPON Interface Evolution Observation by <i>in-situ</i> TEM	115
5.1 Introduction	115
5.2 Experiments details.....	117
5.3 results and analysis	119
5.4 Conclusion.....	124
CHAPTER 6 Summary and Outlooks	125
REFERENCES.....	128
CURRICULUM VITAE.....	140

LIST OF FIGURES

Figure 1. 1 Calculation of specific energy versus cell parameters in cell level. (Copyright 2019 Nature Publishing Group) ³	2
Figure 1. 2 Weight distributions of all cell components in the Li metal pouch cell. (Copyright 2019 Nature Publishing Group) ⁴	3
Figure 1. 3 Schematic of history before Li ion batteries. ⁹	4
Figure 1. 5 Schematic of the lithium growth mechanisms and Li penetration interaction with the nanoporous ceramic separator. (Copyright 2019, Cell Press publishing group) ³¹	9
Figure 1. 6 Failure mechanism of Li metal during Li deposition/dissolution induced by SEI cracks and components consumption. (Copyright 2000, American Chemical Society) ¹¹	11
Figure 1. 7 Schematic of the Li metal nucleation and mossy/dendritic growth processes with issues of uncontrollable SEI cracks, dead Li isolation and porous structure. ⁴¹	12
Figure 1. 8 Schematic showing the correlation between morphology and electrochemical response of a Li-Li symmetric cell during Li plating and stripping. ⁴²	14
Figure 1. 9 Schematic of Li whisker nucleation, root growth and kink forming via real time in-situ liquid cell observation. ³²	15
Figure 1. 10 Atomic-resolution TEM of Li metal dendrites by using cryo-TEM and standard TEM. ⁴³	16
Figure 1. 11 Cryo-TEM images and schematic of mosaic-type SEI in conventional carbonate electrolyte (a) and multilayer structure SEI in electrolyte with FEC as additives (b). ⁴³	17
Figure 1. 12 (a) Schematic of TGC method for inactive Li capacity contribution detection, (b) Analysis of capacity usage in different type electrolyte system. ⁴⁶	18
Figure 1. 13 Schematic of SEI formation corresponding to in-situ SIMS depth profiles with positive and negative ion counts. ⁴⁷	19
Figure 1. 14 Schematic of Li deposition process based on the self-healing electrostatic shield mechanism. (Copyright 2013, American Chemical Society) ¹³	21
Figure 1. 15 SEM images of the morphologies of Li metal after plating on Cu substrates in different electrolytes. (a,b) 1M LiPF ₆ -PC. (c,d) 4M LiFSI-DME. (Copyright 2015 Nature Publishing Group) ¹⁵	23
Figure 1. 16 A popular solid state electrolyte comparison tables with ionic conductivity and their advantages and disadvantages. (Copyright 2017 Nature Publishing Group) ⁶¹	24
Figure 1. 17 Mechanism study of hollow carbon nanosphere layer coating for stabilizing the SEI layer and regulating the Li ion flux. (Copyright 2014 Nature Publishing Group) ²¹	26
Figure 1. 18 Schematic of the LBASEI design with the Li nucleation and growth processes with LBASEI. (Copyright 2018 Nature Publishing Group) ⁶²	26
Figure 1. 19 Illustration of Li and SEI formation in bare Li and Li ₃ PS ₄ -Li (Left), the electron/ion transfer process (Center), and the proposed profile (Right) of the Anion/cation concentration, electric field and potential (Copyright 2019, Cell Press publishing group) ⁶⁷	29

Figure 1. 20 Fabrication of a layered Li-rGO composite film and galvanostatic cycling of a symmetric Li-rGO electrode and Li anode. (Copyright 2016 Nature Publishing Group) ²⁵	31
Figure 1. 21 Illustration of the proposed electrochemical deposition processes of Li metal on (a) planar current collector and (b) 3D current collector and electrochemical performance. (Copyright 2015 Nature Publishing Group) ²⁸	32
Figure 2. 1 Mechanism of Li plating/stripping on Li foil, single-side and double-side infused LiCFFs. Illustration of mossy/dendritic Li nucleation/growth on Li foil, single-side and double-side infused LiCFFs. ⁷	39
Figure 2. 2 Ironing process lead to a limited/controllable molten Li infusion to single side CFF. ⁷	41
Figure 2. 3 Li loading control experiments of LiCFF. ⁷	41
Figure 2. 4 Rolling process for ILC-Li fabrication and images of thin Li foil and digital images of Li foil, ILC-Li top/side view, respectively. ⁹⁰	45
Figure 2. 5 Schematic comparison of conventional SEI and reinforced artificial SEI upon Li metal.....	47
Figure 2. 6 Schematic of drop coating process for producing reinforced artificial SEI-Li electrode.	48
Figure 3. 1 Fabrication and morphology of the LiCFF electrode. Schematic of ironing molten lithium into CFF to form the LiCFF electrode. The insets show the Li-rich (top) and Li-poor (bottom) sides of the sample after ironing and SEM cross-section images.....	50
Figure 3. 2 LiCFF with variety of Li loading and thickness.....	51
Figure 3. 3 Characterizations of the pristine CFF and LiCFF electrode.....	52
Figure 3. 4 XPS spectra of Li-CFF interface.	53
Figure 3. 5 Ex-situ morphology evolution of LiCFF after 10 th cycle Li plating/stripping.	54
Figure 3. 6 Ex-situ morphology evolution of LiCFF after 100 th cycle Li plating/stripping.	55
Figure 3. 7 In-situ capillary cell observation setup and Li plating morphology evolution comparison of Li foil and LiCFF.	57
Figure 3. 8 Schematic of Ti ₃ C ₂ T _x MXene and SEM images, TEM images and HR TEM images.	59
Figure 3. 9 TEM and STEM images of non-delaminating Ti ₃ C ₂ T _x MXene and EDX mapping..	59
Figure 3. 10 SEM cross-section images of ILC-Li with 300 μm Li foil and 30 μm MXene loaded and 30 μm Li and 15 μm MXene film.	60
Figure 3. 11 Inter-layer distance expansion of MXene after cycling.	61
Figure 3. 12 XRD patterns for showing the inter-layer expansion under different current density/cycling capacity and different cycle numbers.	62
Figure 3. 13 Morphology evolution of ILC-Li and Li foil upon Li plating/stripping and its surface roughness measurements.....	64

Figure 3. 14 Cross-section image at MXene-Li interface.....	64
Figure 3. 15 Nitrogen sorption–desorption isotherm of pristine MXene.	65
Figure 3. 16 In-situ capillary cell observation of Li dendrites growth/depletion upon Li plating/stripping.....	66
Figure 3. 17 XPS depth profile of ILC-Li electrode from surface to 1680s etching time (which corresponding to depth of 739nm).....	67
Figure 3. 18 XPS depth profile of Li foil from surface to 900s etching time (which corresponding to depth of 396nm).....	68
Figure 3. 19 Schematic of organic-rich SEI inorganic-rich SEI distribution in Li foil and ILC-Li.	70
Figure 3. 20 Fourier-transform infrared spectroscopy of ACN reacted Li metal and Li foil.	72
Figure 3. 21 (a) Digital image comparison of before and after ACN Li-metal reaction. (b) SEM image of pristine ACN reacted Li metal.	73
Figure 3. 22 SEM image of pristine reinforced artificial SEI Li metal by using precursor of 5% ACN (1M LiTFSI dissolved in) and 95% HFE (a), precursor of 10% ACN (1M LiTFSI dissolved in) and 90% HFE (b) and precursor of 20% ACN (1M LiTFSI dissolved in) and 80% HFE (c).	74
Figure 3. 23 Morphology characterization of reinforced artificial SEI. (a) STEM ADF image of reinforced artificial SEI (b) EDS elemental mapping of reinforced artificial SEI. (c) HR-TEM images of reinforced artificial SEI including low-mag TEM images and high-mag TEM images with lattices of LiF and LiCN. (d-f) Li, C and N K-edge EELS spectra of reinforced artificial SEI.	76
Figure 3. 24 Morphology evolution of the Li foil and reinforced artificial SEI coated Li metal electrodes upon Li plating/stripping at different current densities after 10 cycles.	78
Figure 4. 1 Schematic of symmetric cell.	85
Figure 4. 2 Electrochemical stability of LiCFF electrode.....	87
Figure 4. 3 Galvanostatic cycling of single-side (red), double-side (blue) infused LiCFFs and Li foil (black) at 1 mAcm ⁻² in symmetric cells.	88
Figure 4. 4 Galvanostatic cycling LiCFFs at up to 10 mAcm ⁻² , 10 mAhc m ⁻² in symmetric cells.....	89
Figure 4. 5 EIS Nyquist plots of LiCFF and Li foil in symmetric cell before cycling.	90
Figure 4. 6 Battery performance of LiCFF/NMC and Li foil/NMC full cells.....	91
Figure 4. 7 EIS Nyquist plots of pristine and cycled LiCFF/NMC622 and Li foil/NMC622 full cells.	92
Figure 4. 8 Li-sulfur battery performance by using LiCFF and Li foil.	93
Figure 4. 9 Electrochemical stability of ILC-Li. (a) Galvanostatic cycling of symmetric cells with ILC-Li electrode and Li foil. (b) EIS Nyquist plots in pristine Li foil and ILC-Li. (c) EIS Nyquist plots in 10 th cycled and 100 th cycled Li foil and ILC-Li.....	95
Figure 4. 10 Voltage profile comparison of Li metal with different coatings.	97
Figure 4. 11 Battery and electrochemical interface performance of ILC-Li/NMC full cells and EIS measurements. NMC622 loading: 10 mg cm ⁻²	98

Figure 4. 12 Battery performance at lean electrolyte condition of ILC-Li/NCA full cells and anode free deposition of Li in ILC-Cu/Cu current collector at 0.5mA/cm ² and 1mAh/cm ²	101
Figure 4. 13 Electrochemical stability of reinforced artificial SEI Li metal. (a) Galvanostatic cycling of symmetric cells with reinforced artificial SEI Li.....	103
Figure 4. 14 Battery performance of full cells at lean electrolyte conditions. Cycling capability and voltage profile of the Li foil/NCA battery and the reinforced artificial SEI Li metal/NCA battery NCA loading: 20.5 mg/cm ²	105
Figure 4. 15 Nyquist plots of pristine reinforced artificial SEI-Li (a) and Li foil (b) vs NMC 532 full cells from EIS measurements.	106
Figure 4. 16 Anode volume capacity, gravimetric capacity and areal capacity estimation in Graphite, Li foil single-side and double side LiCFF.	111
Figure 5. 1 Experimental setup for observing the interface between metallic Li and LiPON by using <i>in-situ</i> S/TEM and TEM images.	118
Figure 5. 2 The TEM images of interfacial reaction of LiPON-Li, which start from pristine LiPON and Li metal before contacting, after contacting to 40 seconds.	120
Figure 5. 3 LiPON-Li interfacial reaction area expansion ratio as a function of time.	121
Figure 5. 4 EELS Li K-edge, P K-edge, N K-edge and O K-edge spectra analysis of pristine LiPON and LiPON-Li interface after interfacial reaction.	123

LIST OF TABLES

Table 3. 1 Li metal atomic ratio and mole ratio in Li foil and ILC-Li at different depth.....	69
Table 4. 1 Energy density estimation based on the ILC-Li NCA full-cell battery at lean electrolyte conditions.....	100
Table 5. 1 Volume of $\text{Li}_{2.9}\text{PO}_{3.3}\text{N}_{0.46}$, Li_3P , Li_3N and Li_2O based on standard molar mass and density.....	122

LIST OF ABBREVIATIONS

SEI	Solid electrolyte interphase
LIBs	Lithium ion batteries
LiCFF	Li carbon fiber fabric
LiPON	Lithium phosphorous oxy-nitride
NMC	$\text{LiNi}_x\text{Mn}_y\text{Co}_z\text{O}_2$
NCA	$\text{LiNi}_x\text{Co}_y\text{Al}_z\text{O}_2$
N/P	Negative/positive
CE	Coulombic efficiency
LiMO	Lithium transition metal oxide
J_{lim}	Limited diffusion current density
z_c	Charge number
c_0	Bulk electrolyte concentration
F	Faraday constant
D_{app}	Apparent diffusion coefficient
t_a	Transference number of the anion
L	Inter-electrode distance
J_{cc}	First critical current density
DFT	Density function theory
XRD	X-ray diffraction
TEM	Transmission electron microscopy
SEM	Scanning electron microscopy
MRI	Magnetic resonance imaging
AFM	Atomic force microscopy

LiTFSI	Lithium bis(trifluoromethanesulfonyl)imide
FEC	Fluoroethylene carbonate
TGC	Titration gas chromatography
SIMS	Secondary ion mass spectrometry
LiFSI	Lithium bis(fluorosulfonyl)imide
SSE	Solid state electrolyte
PEO	Polyethylene oxide
NASICON	Sodium superionic conductor
LiSICON	Lithium superionic conductor
rGO	Reduced graphene oxides
ALD	Atomic layer deposition
NMP	N-methyl-2-pyrrolidone
CNT	Carbon nanotube
AAO	Anodic aluminum oxide
EDS	Energy-dispersive X-ray spectroscopy
DEC	Diethyl carbonate
DMA	Dynamic memory analysis
EC	Ethylene carbonate
EIS	Electrochemical impedance spectroscopy
PVDF	Poly(vinylidene fluoride)
XPS	X-ray photon spectroscopy
HAADF	High-angle annular dark-field
STEM	Scanning transmission electron microscopy
ILC	Inter-layer-calated
UHV	Ultrahigh vacuum

EMC	Ethyl methyl carbonate
VC	Vinylene carbonate
ACN	Acetonitrile
HFE	Hydrofluoroethers
EELS	Electron energy loss spectroscopy
FTIR	Fourier-transform infrared spectroscopy

ACKNOWLEDGEMENTS

Foremost, I would like to express my sincere thanks to my PhD supervisor, professor Junjie Niu for his patient advisory and supporting during my PhD career at UW-Milwaukee. He spent a lot of time to provide mentorship, give me a lot of freedom for doing research. His deep knowledge and rigorous attitude made my PhD study a valuable experience. I believe it will benefit my life forever.

I would like to give my special thanks to my committee members Professor Pradeep Rohatgi, Professor Benjamin Church, Professor Nathan Salowitz and Professor Yi Hu for serving as my thesis defense committee members. Their thoughtful suggestions helped me to accomplish this high-quality dissertation.

I would like to acknowledge my deep gratitude to Dr. Miaofang Chi for serving as my co-advisor and her group members Dr. Zachary Hood, Dr. Xiaoming Liu, Prof. Wenpei Gao, other friends to provide kind guidance of electron microscopy at Oak Ridge National Laboratory. I'm also grateful to Prof. Akihiro Kushima to provide professional in-situ TEM training at MIT. I also thank to Prof. Jinyun Liu from UIUC and Chinese Academy of Science, provide excellent samples for in-situ TEM characterization.

I also would like to thank Dr. Steven Hardcastle at UWM AAF, Dr. Heather Owen at UWM biology department EM lab, Mr. Donald Robertson at UWM Physics department TEM lab. Dr. Anna Benko at UWM chemical department Shimadzu Lab, Dr. Alan Nicholls and Dr. Fengyuan Shi at UIC RRC, Dr. Xiaobing Hu and Dr. Xinqi Chen at Northwestern University

NUANCE. Their valuable materials characterization instruments training and supporting made my dissertation benefit from advanced characterization technology.

Moreover, I would like to express my appreciation to all formal and current group members, including Dr. Yongsuk Kim, Dr. Shuai Kang, Dr. Fan Xia, Dr. Yingying Lv, Mingwei Shang and all other members to support all encouragement, experimental help and valuable discussion. I also grateful to my schoolmate and friends at UWM.

Last, I would like to express my best thanks to my parents and grandpa for your supporting and everlasting love. You will always be the most precious in my life.

CHAPTER 1 Introduction

1.1 Next generation high energy density batteries with 500 Wh/kg

Science and technology are changing people's daily lives, the emergence of rechargeable lithium ion batteries and its development is a typical example. Now days, the rapid growing demand for high-energy density energy storage systems in electrical vehicles and portable electric devices has greatly promoted the developing of lithium ion batteries.^{1,2} The U.S. Department of Energy (DoE) declared > 500 Wh/kg target for next generation high energy density lithium-ion batteries³ in 2016, compared to the ~200-265 Wh/kg in commercialized electric vehicle battery, this goal have almost double the current batteries' specific energy density. This ambitious goal far exceeds the inherent limits of existing commercialized electrode materials, which are graphite as anode materials, $\text{LiNi}_x\text{Mn}_y\text{Co}_z\text{O}_2$ (NMC)/ $\text{LiNi}_x\text{Co}_y\text{Al}_z\text{O}_2$ (NCA) as cathode materials. Indeed, replacing all components especially higher proportion anode, cathode and electrolyte by advanced materials is the only way to boost the energy density in lithium ion batteries. From increasing the weight contents of active materials in lithium ion batteries perspective, the engineers are making a lot of efforts on increasing the unit area loading of current graphite anode and NMC/NCA cathode materials, improving electrolyte/cathode (E/C) ratio, reducing the negative/positive electrode (N/P) ratio, developing lighter separator, current collectors, batteries packages. In Figure.1.1, Liu *et al* showed prospect of designing principal for how to boost the energy density to 500 Wh/kg by optimizing the batteries parameters. By using baseline Li metal||NMC622 cell (Cathode capacity of 196 mAh g⁻¹ charge to 4.6 V, 22.0 mg cm⁻² cathode loading, 35% porosity, 70 μm thickness, 2.6 N/P ratio, E/C ratio 3.0 g (Ah)⁻¹) energy density can reach to ~350 Wh/kg. They also outlooked the future high energy density

cell via reducing the E/C ratio to 2.1-2.4 g (Ah)⁻¹, by reducing cathode porosity to 25%, by increasing the cathode thickness to 83 μm and mass loading to 26.0 mg cm⁻², by surpassing the cathode capacity to 220 mAh g⁻¹, by reducing the mass 50% of inactive materials (current collector, packaging), by reducing the Li metal loading to N/P ratio of 1, by using hypothetical new cathode materials with a capacity much higher than 252 mAh g⁻¹.

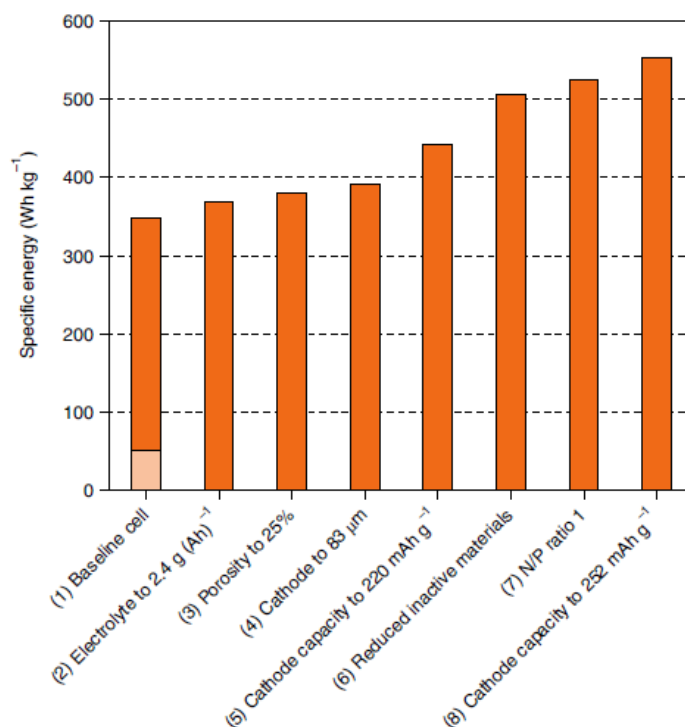


Figure 1. 1 Calculation of specific energy versus cell parameters in cell level. (Copyright 2019 Nature Publishing Group)³

From increasing the energy density of electrode materials perspective, the researchers are making a lot of efforts on developing advanced Li metal anode, high-nickel transition metal oxide cathode, Li-sulfur, Li-air batteries even anode free batteries. To achieve the baseline cell described in Figure 1.1, replacing graphite anode by Li metal anode in conventional batteries can drastically reduce the weight contents of anode in practical cell level.⁴ In Figure 1.2 weight distribution pie charts, Li metal anode only contribute 5.5% in total weight. And by reducing the

Li metal thickness, this value can be reduced lower even anode-free.^{5,6} However, researcher still need to resolve the cycling stability and safety issues, before Li metal can be used to practical batteries. As one of most promising anode materials for next generation lithium batteries, developing highly reversible long-lasting lithium metal is one of the most important steps to achieve 500 Wh/kg level batteries goals.

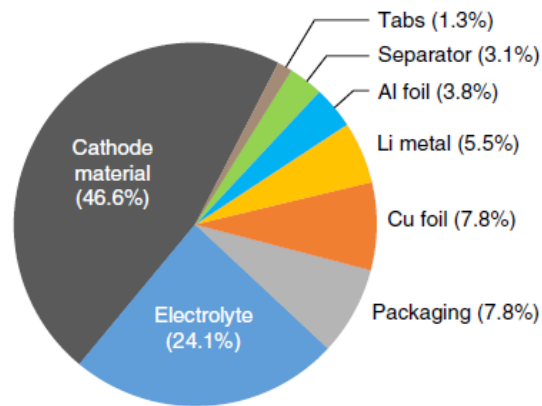


Figure 1. 2 Weight distributions of all cell components in the Li metal pouch cell. (Copyright 2019 Nature Publishing Group)⁴

1.2 History of Li metal anode

Dating back to the history of lithium batteries, lithium metal is selected as anode for first generation secondary lithium ion batteries research by Stanley Whittingham at Exxon in the 1970s.^{1,2,7} After the pioneers' exploration, the Li metal batteries are firstly commercialized by Moli Energy in late 1980s.^{1,8} The first generation commercialized lithium metal batteries is applied MoS₂ as cathode to pair with excess Li metal as anode.^{8,9} Although the hundreds cycles it can achieve and millions of Li metal contained cells were sold to market, the serious safety risk of Li dendrites caused cell shorts-circuit induced thermal controlling failure resulted in recall of all cells, and finally make Li metal batteries eventually become history. In subsequent years, NEC and some other companies continue to attempt the lithium metal safety performance improving. But lithium metal eventually ended in failure and all secondary Li metal batteries disappeared in market and few companies sell it as primary batteries only. Meanwhile, Sony successfully developed the durable carbon based materials as anode to replace metallic Li and graphite gradually developed into a widely used anode material until today.^{7,8}

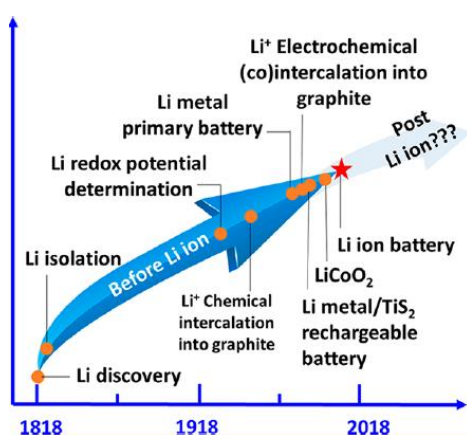


Figure 1. 3 Schematic of history before Li ion batteries.⁹

However, the further demand for higher energy density has led people to reconsider Li metal. If the graphite anode is successfully replaced by lithium metal, energy density will reach ~350 Wh/kg in Li-LiMO (Lithium transition metal oxide as cathode) system. Once the cathode is substituted by sulfur and air, the Li-S and Li-air system can deliver specific energy density of 650 Wh/kg and 950 Wh/kg, respectively.⁸ Although lithium metal has highest theoretical capacity (3860mAh/g) and lowest electrochemical potential (-3.040V vs. standard hydrogen electrode) among all metallic anodes, it still has difficulty for practical applications due to mossy/dendritic lithium formation caused safety concern, and unstable solid electrolyte interphase (SEI) induced low coulombic efficiency (CE).^{7,10} The continue exploration for existence issues on lithium interphase; researchers have more detailed understanding of challenge of lithium metal anode by using advanced technology.^{11,12} In the past decade, researchers have set off an upsurge to revive lithium metal anode. For lithium dendrites suppression and SEI stabilization, approximately six categories of lithium interphase optimization strategies came into our visions: (i) the electrolyte components optimization by adding electrolyte additive and increasing lithium salt concentration.¹³⁻¹⁷ (ii) high ionic conductivity and low interfacial impedance solid state electrolyte that mechanically inhibits dendrites growth.¹⁸⁻²⁰ (iii) electrochemical stable artificial SEI.^{21,22} (iv) stiffness enhanced membrane that ion transport and dendrite growth orientation controllable.²³ (v) pre-stored lithium in stable host for reducing plating/stripping energy barrier and minimizing volume change.²⁴⁻²⁷ (vi) uniform lithium plating/stripping 3D current collectors.^{28,29} Regardless these accomplishments, our exploration of Li metal is far from over, since difficulties in mechanism understanding and scalable practical applications.

1.3 Challenges in Li metal anode

Before the Li metal anode can re-enter the practical engineering application, a lot of arduous tasks need to be overcome including dendritic Li growth induced safety issues and infinite SEI consumption caused cycling performance limitation. The detailed dendritic Li growth and continuous SEI consumption challenges will be studied in this chapter.

One challenge for metallic Li is internal short-circuiting cell induced thermal control failure, which is caused by lithium dendrites growing and penetration through the cell membrane. Another is dendritic Li forming accompanied with uncontrollable SEI during plating and stripping. The large volume change brings continuous consumption of active Li and electrolyte components, so that relatively low coulombic efficiency induced low cycling performance.

Dendritic, mossy, whisker Li – short circuiting conditions

Lithium dendrite in previous paragraphs is abbreviation for all Li whiskers, mossy Li and dendritic Li.^{12,30-32} The essential dendritic Li is that Li growth occurred out of safety boundary^{31,33,34}, called Sand's capacity. The Sand's capacity is determined by two distinct Li growth conditions at Li metal-liquid electrolyte interface, the current densities applied for Li deposition is greater or less than intrinsic diffusion limited current densities. Once current densities exceed the diffusion limitation, we call it reached Sand's capacity and dendritic lithium with tips-growth phenomena occurred. The limited diffusion current density can be expressed based on dilute solution theory:

$$J_{lim} = \frac{2z_c c_0 F D_{app}}{t_a L} \quad (1)$$

The limited diffusion current densities related critical condition of dendritic Li growth also can be expressed in Sand's model. In Li metal-liquid electrolyte contained Li salt case, $z_c = 1$ is the charge number for lithium cation, c_0 is bulk electrolyte concentration, F is Faraday constant, D_{app} is averaged apparent diffusion coefficient of Li cations in liquid electrolyte ($2 \times 10^{-6} \text{ cm}^2 \text{ s}^{-1}$ in 1M Li cations in electrolyte), t_a is transference number of the anion in electrolyte (0.62 for PF_6^- anion), and L is the inter-electrode distance.

As long as the reduction reaction caused Li cation consumption in a Li electrodeposition process, anions from electrolyte was removed by electric field at Li metal-electrolyte interface. The effective diffusion equation can be applied for reveal the Li cation concentration evolution. Once the applied current densities exceeded to the diffusion limit current density at interface, the Li cation concentration decreased to zero at the Li-electrolyte interface during a specific time. The specific time is firstly derived by Sand in 1901 known as Sand's time. After it reached the Sand's time, the stable electroplating becomes unstable at interface, the shortage of cation supply induced dendritic growth by catching up the critical Li cation concentration line. The dendritic Li is commonly considered to be penetrative, but it usually will not occur at normal practical batteries charging/discharging except extremely operation condition. The averaged cell operation current density is about 3 mA cm^{-2} as 20 mA cm^{-2} for dendritic Li growth.

However, Li penetration still can occur under diffusion limit current density. In order to determine accurate critical safety boundary, researchers claimed a first critical current density, J_{cc} below the J_{lim} . The detailed differentiating condition is determined by different SEI status. As current density is below the first critical current density, J_{cc} , root growth Li whisker dominates the Li deposition. This phenomenon may be attributed to the complete coverage of the lithium surface by a robust SEI layer. Beyond the second critical current density, J_{lim} , the system specific

diffusion-limited current density, ion depletion at the electrode surface leads to the diffusion-limited, tip-growing, dendritic lithium that can easily penetrate the nanopores membrane and short the cell. Between these two critical current densities, the SEI formation could be interrupted by the competing lithium deposition, leaving parts of the metal surface without the continuous SEI coverage, such that near isotropic surface growths start to prevail. Based on these findings, we propose a set of safety boundaries along with strategies to optimize the design of rechargeable metal batteries. The detailed mechanism displayed in Fig.1.5.

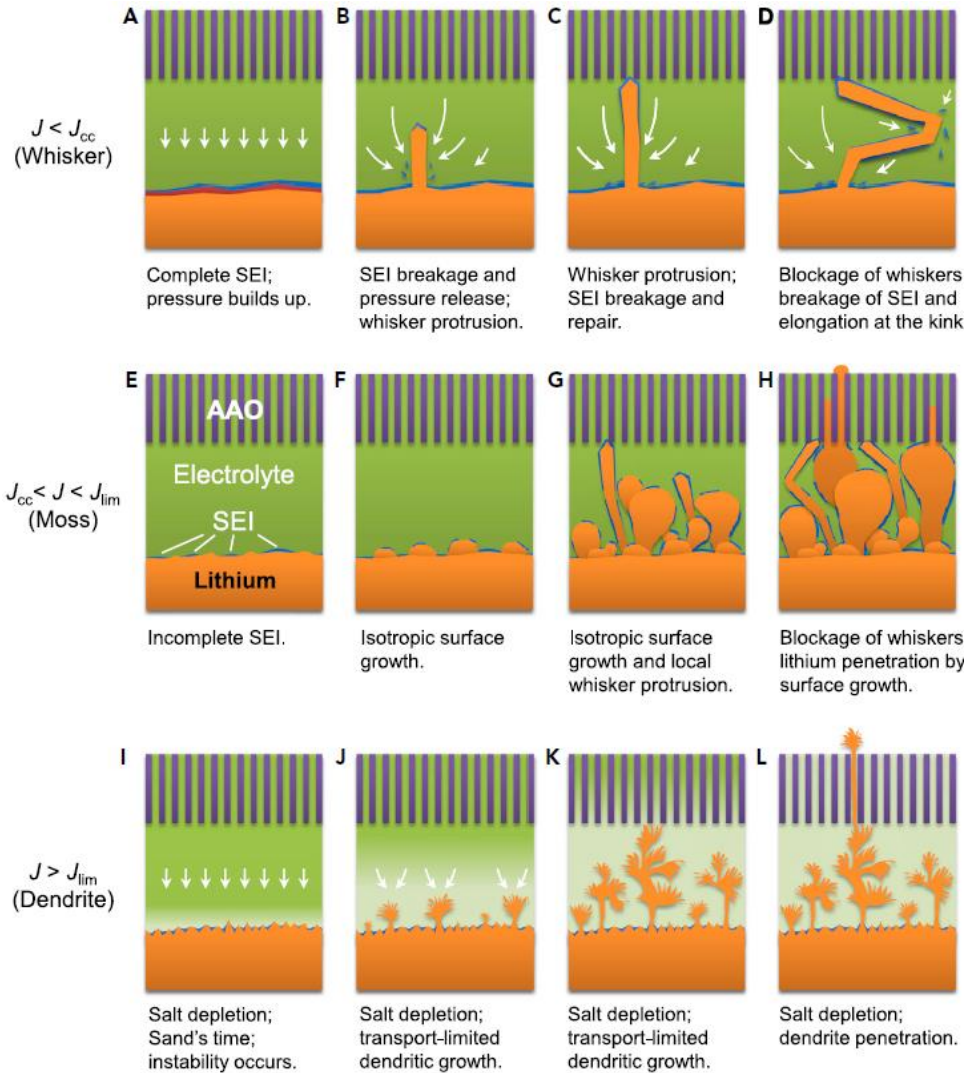


Figure 1. 4 Schematic of the lithium growth mechanisms and Li penetration interaction with the nanoporous ceramic separator. (Copyright 2019, Cell Press publishing group)³¹

Uncontrollable SEI – low coulombic efficiency

The SEI as a critical research component accompanied with Li batteries since the pioneering research work done by Emanuel Peled and Doron Aurbach.^{35–37} Owing the lowest electrochemical potential versus the standard hydrogen electrode, the reduction reaction happened in all Li+/Li surface including electrolyte components. Meanwhile, the passivated SEI

layers played a positive role for the cell cycling, such as stabilizing cell operation and extending of voltage window. However, Li metal anode is restricted by unstable and uncontrollable SEI layer which has detailed schematic in Figure 1.6. The insoluble and passivated SEI formed by lithium reacting with liquid electrolyte solvents at beginning cycles, but mossy lithium growth induced volume change penetrated the stable SEI layer and form the cracks. Then, the fresh lithium exposed to the electrolyte and higher galvanic reactivity between fresh lithium and lithium ion will cause uninform lithium plating/ stripping process and isolated dead lithium. Also, to heal the SEI cracks, the lithium will continually react with electrolyte solvent to form new SEI at cracks. Moreover, the dead lithium consumed lithium ion in electrolyte, so that increase the possibility for lithium ion concentration reach zero at solid-liquid interphase during cycling. Once plating/stripping easily reach 'sand time' during one cycle, the dendritic lithium start to growth, so the dendrites growth penetration induced internal short circuit safety issues occurred.^{12,30,38,39} This is also the reason for low coulombic efficiency (CE). The low CE is a huge sacrifice of the cycling performance of cell.

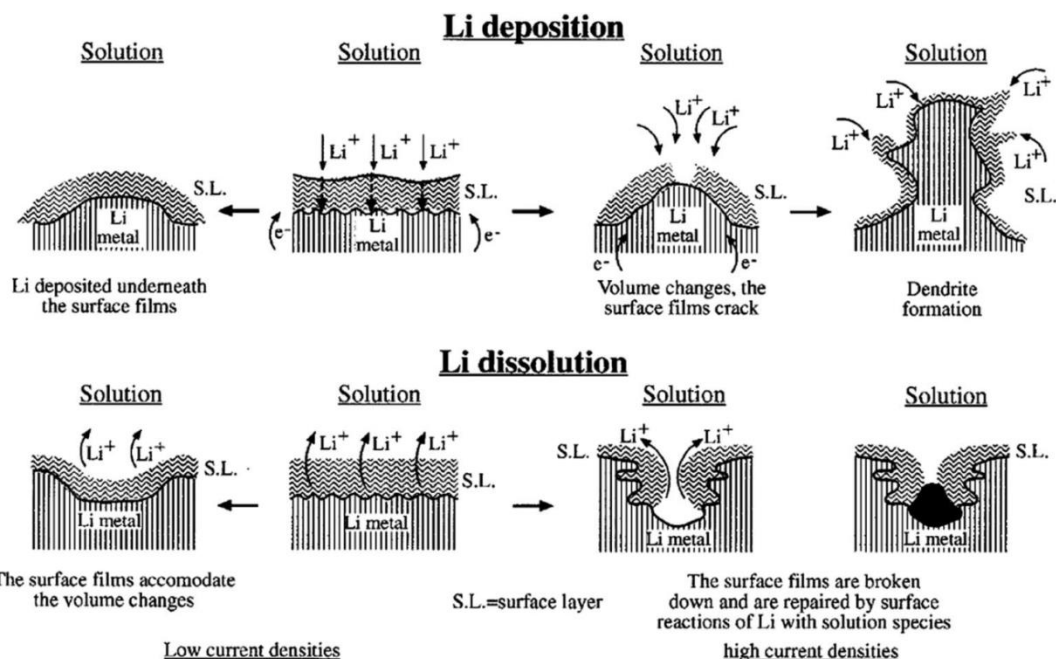


Figure 1. 5 Failure mechanism of Li metal during Li deposition/dissolution induced by SEI cracks and components consumption. (Copyright 2000, American Chemical Society)¹¹

Besides, Li metal has essentially infinite volume change due to its hostless properties. The bulk Li has no space to accommodate the infinite volume change. Once the whisker, mossy and dendritic Li growth formed SEI, the irregular geometry of SEI will be permanently formed. After the continuous cycling, irreversible SEI will continue to pile up and then form the thicker porous SEI, which will gradually increase the internal impedance in cell. Also, fully isolated Li⁴⁰ formed during cycling become the permanent dead Li inside the cell and peeled off from metallic Li anode. More Li and SEI loss will gradually sacrifice the energy density of cell with more cycles and increase the energy barrier for Li plating and stripping, which showed in Figure 1.7.

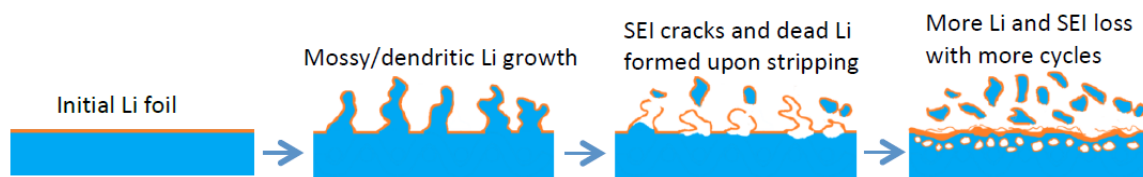


Figure 1. 6 Schematic of the Li metal nucleation and mossy/dendritic growth processes with issues of uncontrollable SEI cracks, dead Li isolation and porous structure.⁴¹

1.4 Characterizations of Li metal and SEI

To understand and to solve the challenges in Li metal, advanced materials characterization techniques was applied to investigate the root cause of Li dendrites growth, SEI components and their dynamic evolution. phase field, Density function theory (DFT) and DFT based multifunction simulations were applied to address the Li metal-electrolyte interface diffusion process and SEI formation mechanism.

1.4.1 Morphology of Li dendrites

There are extensive advanced materials characterization tools for observing Li dendrites, including optical microscopy, X-Ray microtomography, *in-situ* transmission electron microscopy (TEM), *in-situ* scanning electron microscopy (SEM), Cryo-TEM, atomic force microscopy (AFM) and magnetic resonance imaging (MRI). A lot of Li metal dendrites morphology characterization start from entry-level optical microscopy, such as Bai et al. developed capillary cell to observe the Li dendrites plating and stripping under stereo microscope which showed in Fig. 1.4 and Fig. 1.5.¹² The tip growth Li dendrites and root growth mossy Li was successfully distinguished by applying continuous bias until reaching sand time at Li metal-electrolyte interface. Also, the theory of zero concentration line at electrode/electrolyte interface or ‘Sand capacity’ and ‘Sand time’ were explained clearly in Li mossy/dendrites growth model. The results also expressed a fundamental design limitation conditions for Li metal batteries. As showed in Fig. 1.8, Wood et al. used close window operando optical microscope to reveal the dynamic mossy/dendritic Li growth/dissolution process corresponding to voltage profile.^{30,42} Especially, the stripping response has kinetically fast stripping stage, “dead” Li forming/high

polarization stage and Li bulk pitting stage. The results exhibited Li metal mass transport corresponding to voltage profiles during Li plating and stripping.

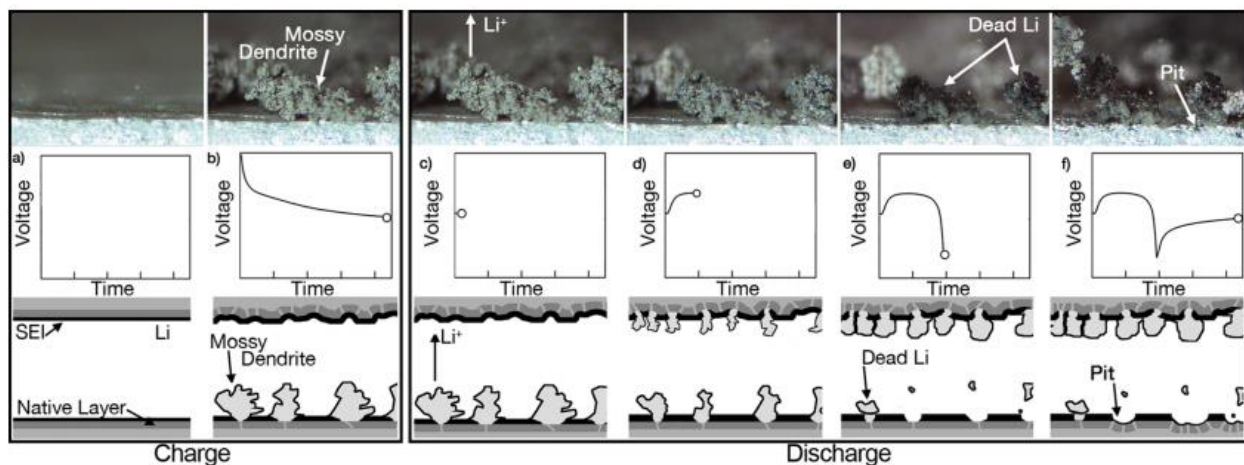


Figure 1. 7 Schematic showing the correlation between morphology and electrochemical response of a Li-Li symmetric cell during Li plating and stripping.⁴²

TEM is one most powerful tool for materials characterization, it provides valuable root cause results of Li dendrites affiliated with in-situ setup. As showed in Fig.1.9, Kushima et al. applied in-situ liquid cell to reveal the early nucleation stage of Li metal deposition under TEM.³² The sealed window liquid cell experimental setup consist with LiCoO_2 as cathode, Au as Li anode deposition current collector and 1M LiTFSI containing electrolyte. The results identified 4 stages of initial Li nucleation and growth, including nucleation, root growth of Li whisker, growth rate decreasing and kink forming and growth. It firstly revealed the nanoscale Li metal growth from early nucleation stage.

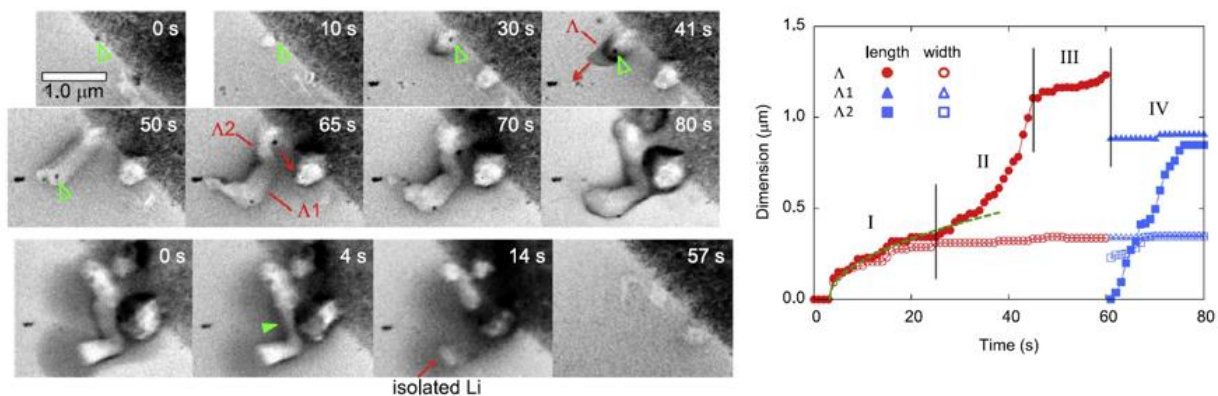


Figure 1. 8 Schematic of Li whisker nucleation, root growth and kink forming via real time in-situ liquid cell observation.³²

Beyond the in-situ TEM level, the researchers also revealed atomic level images of Li dendrites by cryo-TEM (Shown in Fig.1.10).⁴³ The standard TEM unable to image the Li dendrites at atomic resolution level since its electron beam sensitive nature. But cryogenic holder allows the observation of Li dendrites at its pristine morphology and crystalline structure. The results also revealed the Li metal-SEI interface at atomic level TEM characterization. The Li dendrites was observed as $\langle 110 \rangle$ and $\langle 211 \rangle$ faced single crystal, it prefers to grow along with $\langle 111 \rangle$ plane. Also, Li whisker kinks forming without crystallographic defects.

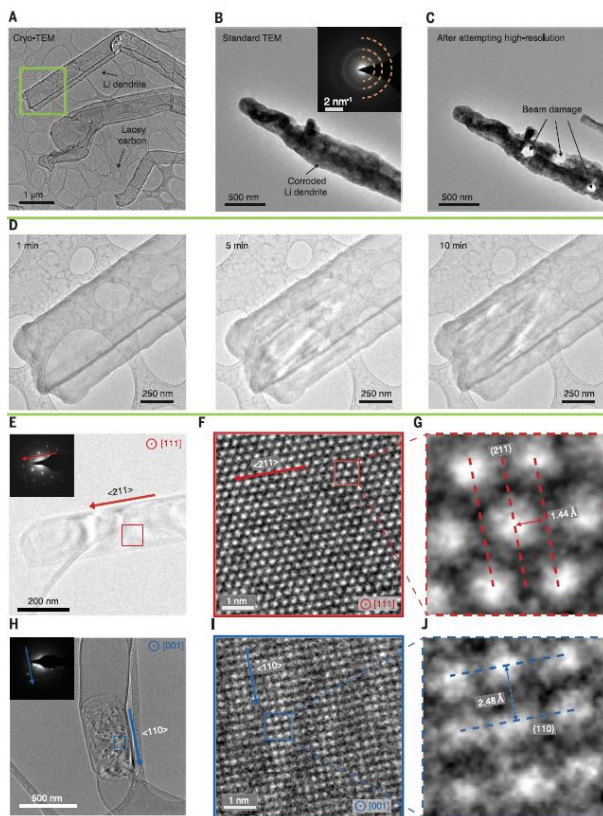


Figure 1. 9 Atomic-resolution TEM of Li metal dendrites by using cryo-TEM and standard TEM.⁴³

1.4.2 Characterization of Li metal SEI

As alkali metal, Li metal is highly reactive with organic solvents and inorganic lithium containing salt components in electrolyte. The formation of SEI serve as a buffer layer to avoid Li metal direct contact with electrolyte, SEI also serve as the electron insulator and Li ion conductor to support Li plating/stripping process. SEI plays an important role to effect all anode including Li metal cycling performance and Li morphology in batteries operation.⁴⁴ Peled *et al.* believe SEI has the heterogeneous mixed organic and inorganic, which is called mosaic structure.⁴⁵ The mosaic structure has organic polyolefins, semicarbonates structure at surface and inorganic structure Li_2O , LiF , Li_2CO_3 under the organic components. In Fig. 1.11, The mosaic

structure of SEI also was directly observed by Li *et al.* via cryo-TEM in the conventional ethylene carbonate-diethyl carbonate-based electrolyte. In carbonate electrolyte system with fluoroethylene carbonate (FEC) as additive, the multi-layer structure SEI with Li_2O at surface was observed as well. The investigation of Li dendrites surface SEI has different model along with variety electrolyte.

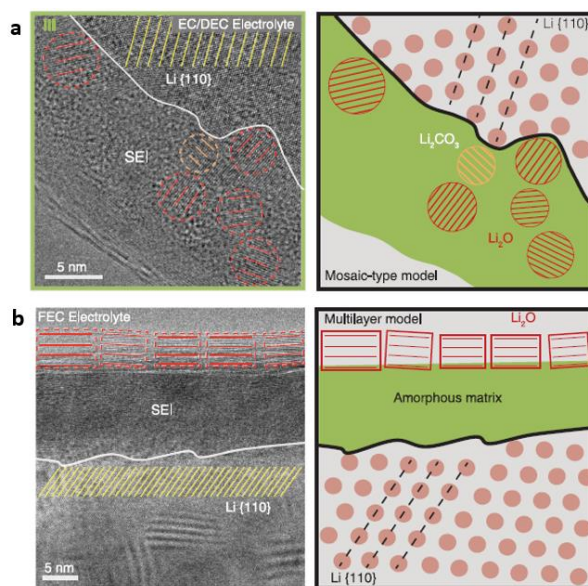


Figure 1.10 Cryo-TEM images and schematic of mosaic-type SEI in conventional carbonate electrolyte (a) and multilayer structure SEI in electrolyte with FEC as additives (b).⁴³

To investigate the Li dendrites/SEI volume change/fragmentation induced and Li loss, Fang et al. quantitatively analyzed the reversible Li, inactive Li and SEI Li^+ in different electrolyte Li metal batteries system.⁴⁶ The reversible Li was measured by coulombic efficiency (CE) within one cycle of Li metal cycling. An analytical method titration gas chromatography (TGC) was applied to identify the amount of unreacted Li and Li^+ in formed SEI. In Fig. 1.12, the capacity usage contribution was identified among different electrolyte system. Huge unreacted Li and SEI Li amount contribution discrepancy implies that different types electrolyte

system have a significant impact on Li metal charging/discharging kinetic rate. In those electrolyte systems with lower CE and inactive Li system, Li tips cannot catch up the pace of fast Li plating and stripping resulting in shedding from Li bulk substrate. The data reported in this literature shed light on electrolyte/SEI designing principles for more efficient Li metal anode charging/discharging.

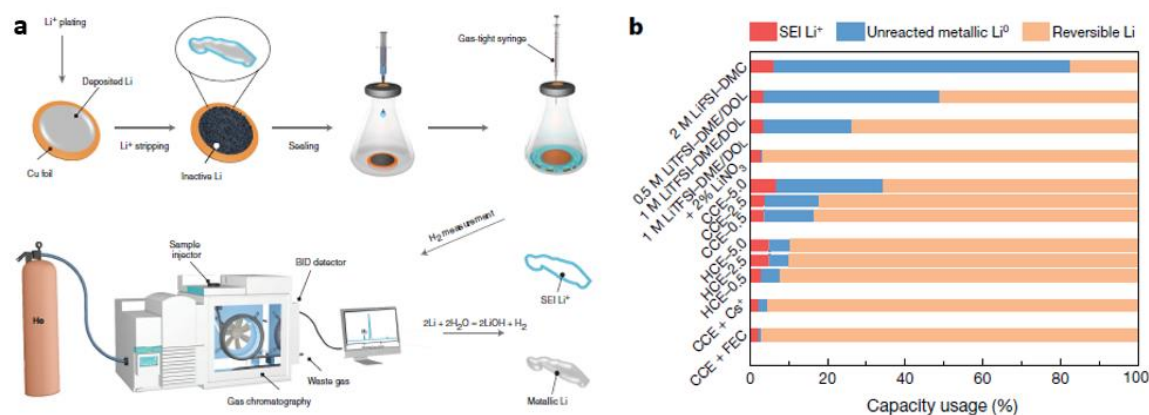


Figure 1.11 (a) Schematic of TGC method for inactive Li capacity contribution detection, (b) Analysis of capacity usage in different type electrolyte system.⁴⁶

Zhu *et al.* used *in-situ* liquid secondary ion mass spectrometry (SIMS) to identify the dynamic formation of SEI at early stage.⁴⁷ According to the inference of the data in the Fig. 1.13, an electric double layer formed at electrode/electrolyte interface owing to current collector surface potential and Li⁺. After negatively charge was applied to current collector, negatively charged current collector repel the salt anions stay at inner layer of SEI. Therefore, dense inorganic rich SEI layer formed at inner SEI and organic-rich components formed at outer SEI. It is because of this SEI structure that provides ionic conductivity, electron insulator during Li metal cycling.

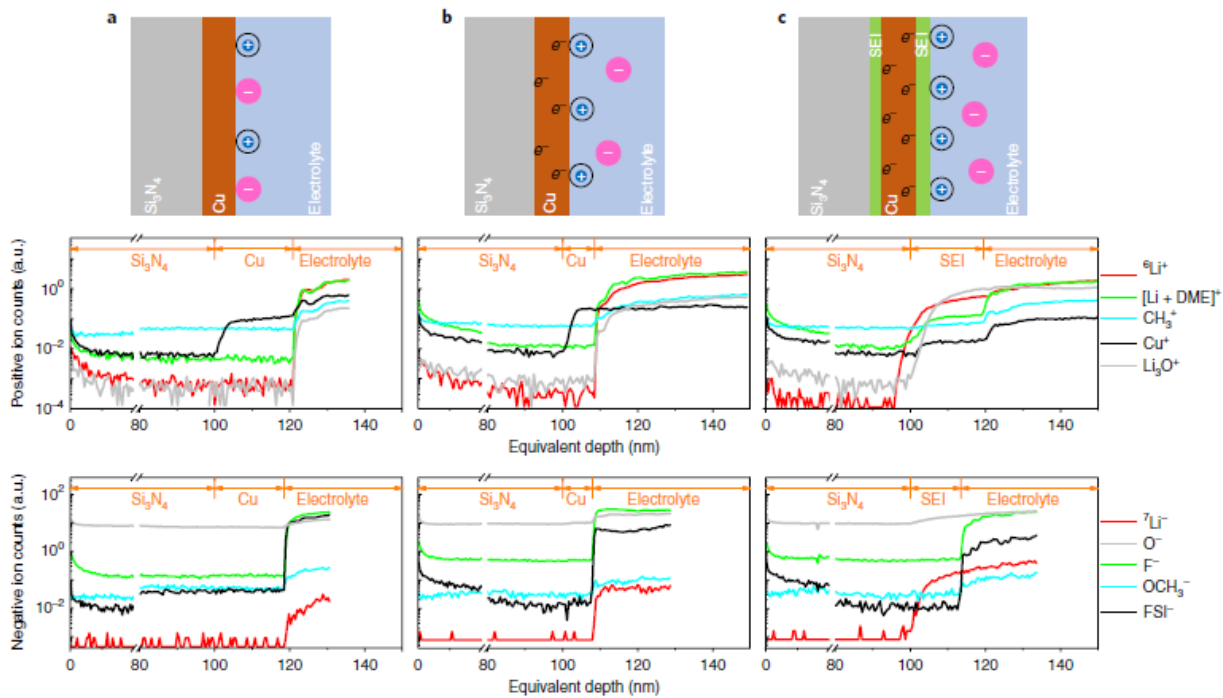


Figure 1.12 Schematic of SEI formation corresponding to in-situ SIMS depth profiles with positive and negative ion counts.⁴⁷

1.5 Current state of art in Li metal anode efforts

The electrolyte and interfacial engineering have been investigated for improving Li metal anode performance over decades. Here, the proposed Li modification methods during most recent ten years will be reviewed and discussed. Besides, the pre-stored Li in stable host and uniform electrodeposition in 3D configuration will also be reviewed and studied.

1.5.1 Electrolyte engineering

Liquid electrolyte modification have been widely investigated especially Li salt in electrolyte, electrolyte solvent components and additive. Especially additives, they can be physically or chemically adsorbed on the Li surface. And then, they can also decompose or synthesize new lithium compounds to help with uniform lithium metal plating/stripping or stabilizing the SEI. Herein, electrolyte additive and high concentration electrolyte will be highlighted.

Electrolyte additive

At the early time, the electrolyte additives including gaseous molecules, organic aromatic compounds, vinylene carbonate, 2-methylfuran and surfactants were already considered to have positive effect on Li metal.^{7,10,16,48,49} After that, *fluorinated compounds* such as limited amounts of HF and H₂O inside of carbonate electrolyte can facilitate the growth of a LiF/Li₂O interlayer on Li surface with dense inorganic inner layer SEI and regulating Li electrodeposition.^{17,50} In 2013, the researchers revealed a novel electrolyte engineering that can eventually change Li dendrites formation. Selected alkali cations (such as Cs⁺ and Rb⁺) with limited concentration has lower reduction potential than lithium ions. When lithium deposition occurred, selected alkali cations additives can take shape of an electrostatic shield with positively charged at early stage

of Li tip nucleation/growth (showed in Figure 1.14). These selected alkali cations additives have no further reduction to alkali metal. The strategy (called *self-healing electrostatic shield*) exhibits a significant lithium dendrite formation/growth prevention, it also can promote the uniform lithium deposition, favorable interface lithium ion reduction in lithium metal batteries.¹³ In ether-based electrolyte system, *synergetic effect of both lithium polysulfide and LiNO₃* results to a uniform and stable SEI at Li metal surface to suppress Li dendrites growth and electrolyte consumption.¹⁴ It is another case of electrolyte engineering to prevent lithium dendrites growth by adding electrolyte additives such as lithium polysulfide and LiNO₃.

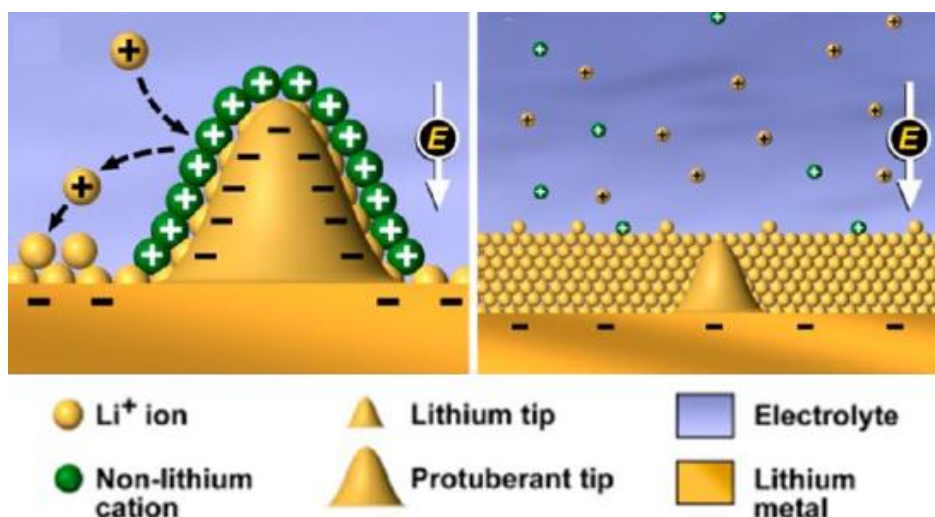


Figure 1. 13 Schematic of Li deposition process based on the self-healing electrostatic shield mechanism. (Copyright 2013, American Chemical Society)¹³

High concentration electrolyte

Based on dilute solution theory limited diffusion current density equation, high Li cation concentration can increase J_{lim} . Therefore, high concentration Li can suppress the Li dendrites growth since increased J_{lim} can enhance the threshold for Li dendrites growing. Researchers used

4M lithium bis(fluorosulfonyl)imide (LiFSI) in ether-based electrolyte lead to a nodule-like Li deposition, stable SEI and high CE even under high current density (Figure 1.15). By using 4M LiFSI ether-based electrolyte, Li metal symmetric cell cycling operation under high current density of 10mAcm^{-2} , cycling performance can reach 6000 cycles. To evaluate CE, a Cu current collector|Li metal cell cycling operation under high current density of 4mA cm^{-2} can maintain average CE as high as 98.4% after 1000 cycles.¹⁵ In a similar approach, using high concentration of 7M LiTFSI exhibited effectively suppressed Li dendrites and minimized dissolution of polysulfide in Li-S batteries. This concept also was called as solvent in salt.⁵¹ In 2018, researchers reported Li dendrites suppression work by altering the electrolyte to a network structure of quasi-solid state. Quasi-solid state means the lithium salt concentration in electrolyte is saturated. This strategy of using highest concentration electrolyte can resolve Li dendrites growth at Li metal anode side.⁵² In summary, increase the Li cation concentration is a good solution for Li metal challenges, but the cost of Li salt need to be reduced.

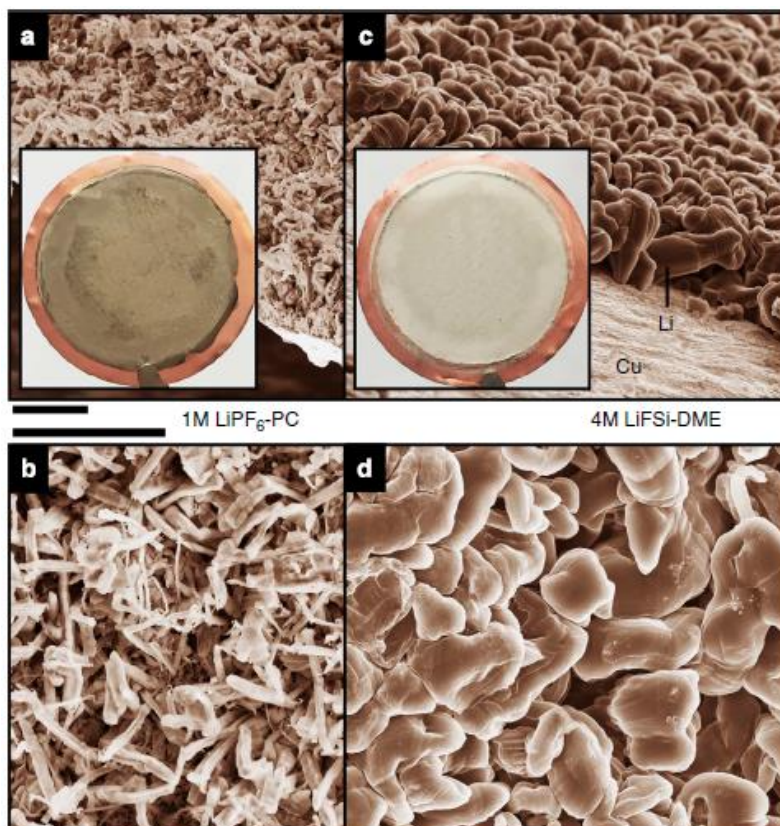


Figure 1. 14 SEM images of the morphologies of Li metal after plating on Cu substrates in different electrolytes. (a,b) 1M LiPF₆-PC. (c,d) 4M LiFSI-DME. (Copyright 2015 Nature Publishing Group)¹⁵

Solid state electrolyte

The rapidly growing trends of using all-solid-state Li ion batteries (LiBs) promoted solid state electrolyte (SSE) to become one of the most popular energy storage technologies in past decade.⁵³ A lot of effort have been made by developing organic and inorganic SSE materials in past decades (Figure 1.16), such as organic SSE materials polyethylene oxide (PEO),⁵⁴ inorganic thin film SSE-lithium phosphorus oxynitride (LiPON)⁵⁵ and inorganic ceramic SSE (perovskite-type,⁵⁶ sodium superionic conductor (NASICON)-type,⁵⁷ lithium superionic conductor (LiSICON)-type,⁵⁸ garnet-type⁵⁹ and sulfide-type⁶⁰). Due to its excellent safety and adequate

electrochemical stability, SSE has some irreplaceable superiorities compared with liquid electrolyte.³⁴ Also, lower possibilities of lithium dendrites penetration issues and relatively wide Li/Li⁺ electrochemical stable windows enable the utilizing of lithium metal as anode paired with SSE. Although recent literature has disputed whether solid electrolytes can inhibit dendrite, the inflammable nature of solid-state electrolyte is still a safer choice than liquid electrolyte. Herein, a list about popular solid-state electrolyte research approaches is displayed.

Type	Materials	Conductivity (S _{cm} ⁻¹)	Advantages	Disadvantages
Oxide	Perovskite Li _{3.3} La _{0.56} TiO ₃ , NASICON LiTi ₂ (PO ₄) ₃ , LISICON Li ₁₄ Zn(GeO ₄) ₄ and garnet Li ₇ La ₃ Zr ₂ O ₁₂	10 ⁻⁵ –10 ⁻³	<ul style="list-style-type: none"> • High chemical and electrochemical stability • High mechanical strength • High electrochemical oxidation voltage 	<ul style="list-style-type: none"> • Non-flexible • Expensive large-scale production
Sulfide	Li ₂ S–P ₂ S ₅ , Li ₂ S–P ₂ S ₅ –MS _x	10 ⁻⁷ –10 ⁻³	<ul style="list-style-type: none"> • High conductivity • Good mechanical strength and mechanical flexibility • Low grain-boundary resistance 	<ul style="list-style-type: none"> • Low oxidation stability • Sensitive to moisture • Poor compatibility with cathode materials
Hydride	LiBH ₄ , LiBH ₄ –LiX (X=Cl, Br or I), LiBH ₄ –LiNH ₂ , LiNH ₂ , Li ₃ AlH ₆ and Li ₂ NH	10 ⁻⁷ –10 ⁻⁴	<ul style="list-style-type: none"> • Low grain-boundary resistance • Stable with lithium metal • Good mechanical strength and mechanical flexibility 	<ul style="list-style-type: none"> • Sensitive to moisture • Poor compatibility with cathode materials
Halide	LiI, spinel Li ₂ ZnI ₄ and anti-perovskite Li ₃ OCl	10 ⁻⁸ –10 ⁻⁵	<ul style="list-style-type: none"> • Stable with lithium metal • Good mechanical strength and mechanical flexibility 	<ul style="list-style-type: none"> • Sensitive to moisture • Low oxidation voltage • Low conductivity
Borate or phosphate	Li ₂ B ₄ O ₇ , Li ₃ PO ₄ and Li ₂ O–B ₂ O ₃ –P ₂ O ₅	10 ⁻⁷ –10 ⁻⁶	<ul style="list-style-type: none"> • Facile manufacturing process • Good manufacturing reproducibility • Good durability 	<ul style="list-style-type: none"> • Relatively low conductivity
Thin film	LiPON	10 ⁻⁶	<ul style="list-style-type: none"> • Stable with lithium metal • Stable with cathode materials 	<ul style="list-style-type: none"> • Expensive large-scale production
Polymer	PEO	10 ⁻⁴ (65–78 °C)	<ul style="list-style-type: none"> • Stable with lithium metal • Flexible • Easy to produce a large-area membrane • Low shear modulus 	<ul style="list-style-type: none"> • Limited thermal stability • Low oxidation voltage (<4V)

LiPON, lithium phosphorus oxynitride; LISICON, lithium superionic conductor; NASICON, sodium superionic conductor; PEO, poly(ethylene oxide).

Figure 1. 15 A popular solid state electrolyte comparison tables with ionic conductivity and their advantages and disadvantages. (Copyright 2017 Nature Publishing Group)⁶¹

1.5.2 Interfacial engineering

The intrinsic formed SEI films during cycling are complicated, and researchers has limited understandings about what are the specific components of intrinsic formed SEI and how they influence SEI layer properties and batteries performance. In order to avoid the uncontrollable SEI induced Li depletion and electrolyte components consumption. Considerable efforts based on interfacial engineering also called artificial SEI were introduced in Li metal anode modification. Based on interfacial treatment methods, they are listed here as following categories: physical, chemical and electrochemical pretreatments.

Physical treatment

Physical treatment targeted on coating a passivated protective layer on Li metal for mechanically suppressing dendrites and regulating Li ions flux. Most of methods (including spin coating, rolling, flash evaporation, doctor-blade coating, etc.) are facile and cost friendly, which is available in practical Li metal batteries. Also, some fancy methods such as atomic layer deposition and magnetron sputtering were applied for coating.

As far as current knowledge, the artificial SEI concept was firstly introduced by researcher in Stanford University in 2014. Interconnected hollow carbon nanospheres monolayer thin film coating applied on Li metal anode (Figure 1.17). The electrochemical and morphology characterization results exhibited that coated carbon nanospheres SEI helps to isolate the lithium metal depositions and facilitates the formation of a stable solid electrolyte interphase. No obviously Li dendrites formation was observed by scanning electron microscope (SEM) under current densities of $1\text{mAh}/\text{cm}^{-2}$. The CE maintain at $\sim 99\%$ for over 150 cycles. It indicated that

nanoscale interfacial engineering is a potential promising strategy for Li metal anode improvement.²¹

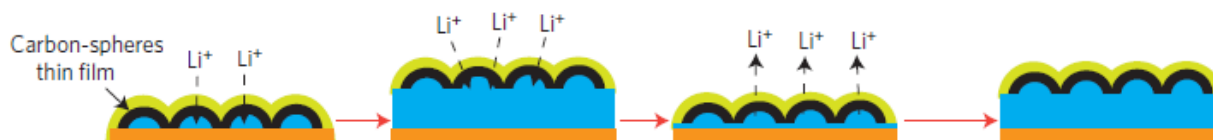


Figure 1. 16 Mechanism study of hollow carbon nanosphere layer coating for stabilizing the SEI layer and regulating the Li ion flux. (Copyright 2014 Nature Publishing Group)²¹

Sharing similar mechanism, a Langmuir–Blodgett artificial SEIs (LBASEIs) was synthesized by using functionalized reduced graphene oxides (rGO) (Figure 1.8). It was physically coated on Li foil by most common used cold treatment materials-rolling process. It is found to be effectively stabilizing the Li metal and regulating Li growth to a horizontal direction. This design has strong full cell electrochemical data to support LBASEIs coated Li has excellent performance paired with commercialized intercalation cathode Li nickel cobalt manganese (NMC).⁶²

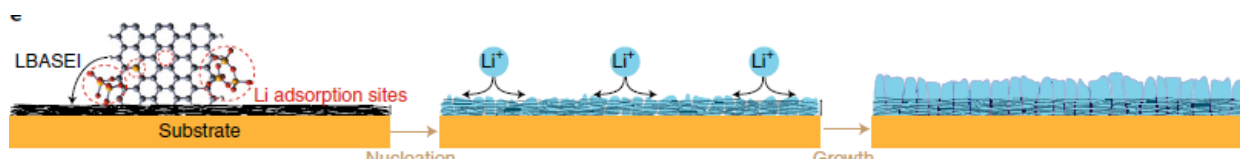


Figure 1. 17 Schematic of the LBASEI design with the Li nucleation and growth processes with LBASEI. (Copyright 2018 Nature Publishing Group)⁶²

Another artificial soft-rigid protective layer made by poly (vinylidene-co-hexafluoropropylene) (PVDF-HFP)⁶³ and LiF⁶⁴ was indicated to have favorable attributes such as excellent mechanical performance, good compatibility with Li and high ionic conductivity.

The ALD method can achieve an ultrathin 14 nm thick ALD Al_2O_3 layer on Li metal to effectively prevent Li metal from corrosion of electrolyte.⁶⁴ It can also functionalize with other components to generate composite protective layers. Other inorganic protective layer such as Li_3PO_4 has been tried to be deposited as a thin film on Li metal foils by magnetron sputtering. The amorphous Li_3PO_4 thin films have thicknesses of 0-200 nm, and it has an almost insulated property with a low electronic conductivity. The conformal coating layer Li_3PO_4 can successfully suppress Li dendrite growth and extend its lifespan as well.⁶⁵

Chemical treatment

Similar to physical treatment, the chemical treated Li metal has passivated protective layer properties to avoid further reaction between Li and electrolyte components. Due to high activity of lithium metal, chemical treatment can easily introduce one or several more components to protective layer. The chemical treatment methods include gas processing, Li alloy processing and other wet chemical treated ionic conductive processing.

By using simple gaseous reaction process, N_2 pretreated Li metal exhibited an overwhelming benefiting role to protect Li metal by directly reacting the Li metal with N_2 gas at room temperature to form a Li_3N protection layer on the Li surface. Researchers also developed a conformal LiF coating technique on Li surface with commercial Freon R134a as the gaseous reaction reagent. Comparing with conventional solid/liquid reaction reagents, gaseous Freon has advantages of well reaction controllability, resulting to a permeable and uniform LiF coating on Li metal.⁶⁶ Thus, the Li plating/stripping process was successfully regulated by inorganic LiF-rich artificial SEI coating.

Researchers reported Li-rich composite alloy films (for example, $\text{Li}_{13}\text{In}_3$, LiZn , Li_3Bi , or Li_3As) coating to enhance the performance of Li metal batteries. It was synthesized via in-situ liquid reaction on lithium surface to form Li-rich alloys. It showed an effectively prevention of Li dendrite growth as well. This protected Li-rich alloy approach is stabilized to sustain plating/stripping over 700 cycles in Li metal symmetric cell at a current density of 2 mAcm^{-2} . And pairing with $\text{Li}_4\text{Ti}_5\text{O}_{12}$ as counter electrode, 1500 cycle can be achieved for cycling.²²

The conventional high ionic conductive sulfide-based SSE Li_3PS_4 was coated as protective artificial SEI. Li_3PS_4 was coated via wet chemical by reacting precursor with Li metal (showed on Figure 1.19), which is a simple directly reaction showed here: $10 \text{ Li} + \text{Li}_2\text{S}_6 + 2 \text{ P}_2\text{S}_5 \rightarrow 4 \text{ Li}_3\text{PS}_4$. The high ionic conductive Li_3PS_4 thin film successfully suppressed Li dendrites growth and limited infinite volume expansion. The proposed potential profile, ion concentration profile and electric field profile were further used to reveal the mechanism of improvement in Li_3PS_4 coated Li. In symmetric cell results, over 2500 hours stable cycling in Li_3PS_4 coated Li metal. And in full cell with $\text{Li}_4\text{Ti}_5\text{O}_{12}$ as counter electrode, 400 cycles stable operation under high current density of 8 mAcm^{-2} .⁶⁷ Another case by using protective Li_3PS_4 layer formed by $12 \text{ Li} + \text{P}_4\text{S}_{16} \rightarrow 4 \text{ Li}_3\text{PS}_4$ reaction in N-methyl-2-pyrrolidone (NMP) was reported. The Li_3PS_4 layer was indicated that it can prevent the formation of Li dendrites and reduce side reactions during cycling and SEI consumption. The electrochemical performance improved with a higher capacity retention in Li-S batteries by using Li_3PS_4 -Li metal as anode at high current density of 5 A g^{-1} for over 400 cycles.⁶⁸

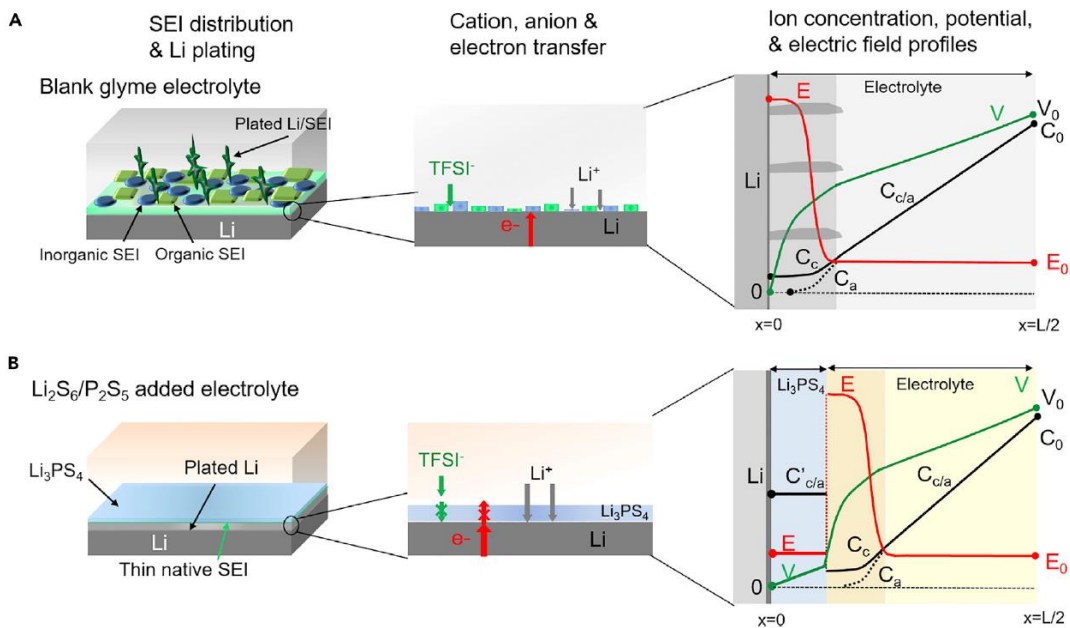


Figure 1. 18 Illustration of Li and SEI formation in bare Li and $\text{Li}_3\text{PS}_4\text{-Li}$ (Left), the electron/ion transfer process (Center), and the proposed profile (Right) of the Anion/cation concentration, electric field and potential (Copyright 2019, Cell Press publishing group)⁶⁷

1.5.3 Li hosts with 3D configuration

The ‘hostless’ nature is considered to be essential cause of infinite volume change in Li metal. The Li hosts should have high stability and high compatibility with Li metal or at least no further decomposition during cycling. Also, high surface area and 3 dimensional structures is another necessary feature. Recently, considerable efforts were performed for stabilizing Li hosts including conductive or nonconductive materials. The major benefits obtained from host are volume change minimization by introducing 3D configuration with high surface area induced Li separation into smaller domains, so that significantly reduce the effect current densities for Li deposition and dissolution. Then, 3D framework regulated the Li ion flux for homogenizing the

Li deposition and dissolution. Also, the host inherent structure can maintain at a constant volume during cell cycling, so that reduced strain in electrode materials by minimizing volume change.

Conductive host

High conductive host has nature advantage for collect current in Li deposition, host also can reduce the effect current densities at local domain. The conductive host materials selections are mainly divided into carbon based and metal based. Carbon materials have high stability and well-developed nanoscale options, such as graphene, carbon nanotube (CNT) and carbon fibers. Metal materials such as nickel and copper have high compatible properties with Li by intrinsic alloy diffusion phenomenon.

In a conductive host example, layered-stacked rGO thin film was fabricated via molten lithium infusion process (Figure 1.20). The layered-stacked rGO thin film has excellent wettability with molten Li, it also called lithiophilicity phenomenon. The molten Li can quickly self-infused into layered-stacked rGO thin film by only touching the edge of rGO thin film to molten Li. It is explained as strong capillary force induced infusion. The layered-stacked rGO film contribute only 7 wt% of anode. And less than 20% volume change was observed after molten Li infusion, which can lead to a much more stable cycling with lower polarization. The rGO-Li anode maintains up to $\sim 3,390 \text{ mAh g}^{-1}$ of capacity of first cycle, showed low overpotential of $\sim 80 \text{ mV}$ under current density of 3 mA cm^{-2} . A flat-smooth voltage profile was collected in battery cycling with a carbonate electrolyte. In full-cell battery paired with LiCoO_2 (LCO) exhibited good rate capability and flat-smooth voltage profiles.²⁵

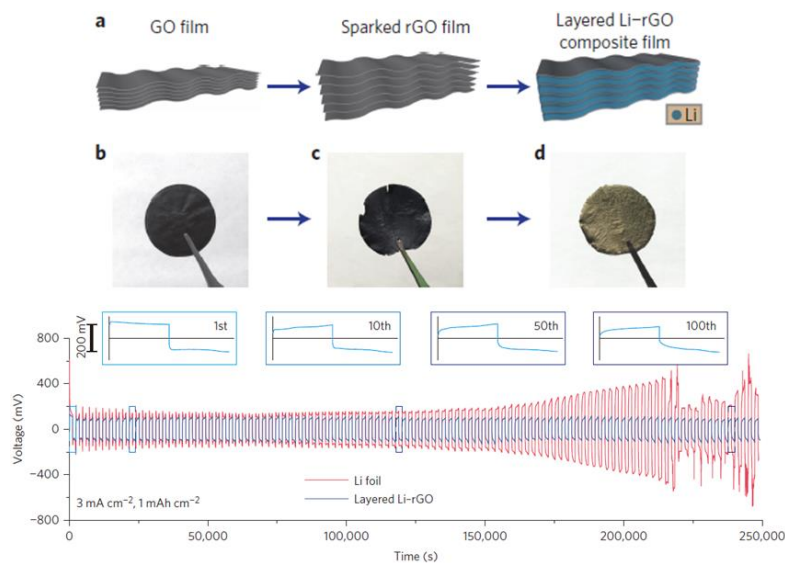


Figure 1. 19 Fabrication of a layered Li-rGO composite film and galvanostatic cycling of a symmetric Li-rGO electrode and Li anode. (Copyright 2016 Nature Publishing Group)²⁵

Another typical category of conductive host, metal-based host, was reported by using nickel metal foam Li composites.⁶⁹ The Li metal-nickel hybrid anode was achieved by molten Li infusion process. In comparison with the Li foil, the Li-Ni hybrid anode showed a stable overpotential of 200 mV at a current density of 5.0 mA cm⁻². The symmetric cell cycling with limited hysteresis over 100 cycles by using carbonate electrolyte. It also has good high-rate capability. The interfacial resistance was minimized, resulting in a small polarization in full-cell battery by pairing with Li₄Ti₅O₁₂ or LiFePO₄ as counter electrode. The merely ≈3.1% volume change was observed as a great host for suppressing Li dendrite formation. Also, the mechanism for uniform lithium stripping/plating behavior is explained based on a surface energy model. Besides, a 3D submicron copper fiber current collector was developed for performance improvement on Li metal anode. The mechanism of 3D copper submicron skeleton^{28,29} is displayed at following Figure 1.21. The high surface area current collector can significantly

reduce the effect current density and accommodate the volume change. In Li metal deposition and dissolution process, once Li nucleated at one site, the charges will accumulate at this sharp site or tips site. In comparison with Li metal, numerous protuberant tips perform as charge centers and nucleation sites, so that electric fields were regulated homogeneously. Also, the cell can stable cycle over 600 hours under a limited voltage hysteresis in this 3D copper current collector design.

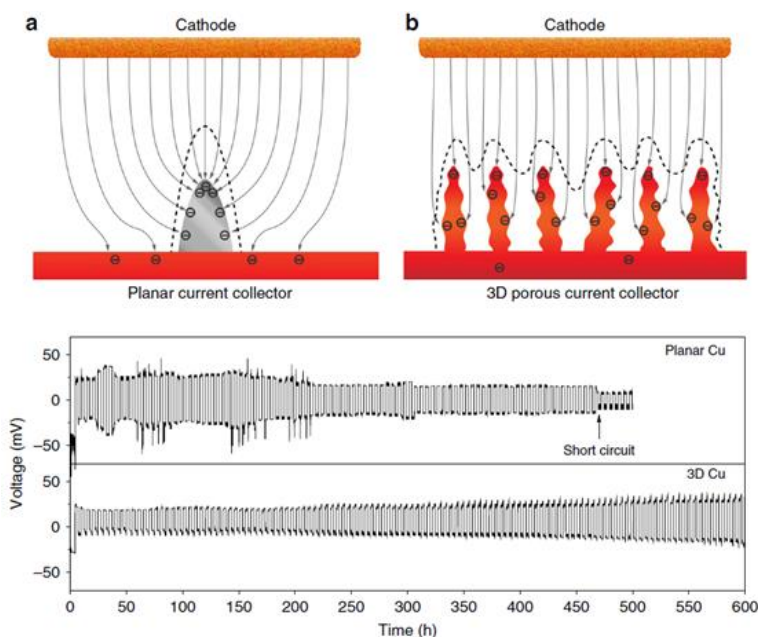


Figure 1. 20 Illustration of the proposed electrochemical deposition processes of Li metal on (a) planar current collector and (b) 3D current collector and electrochemical performance. (Copyright 2015 Nature Publishing Group)²⁸

In another case, a scaffold made by covalently connected graphite microntubes is reported,⁷⁰ which provides a firm and conductive frame-work with moderate specific surface area to accommodate Li metal for anodes of Li metal batteries. The anode presents an areal capacity of 10 mA h cm⁻² (prac-tical gravimetric capacity of 913 mA h g⁻¹) at a current density

of 10 mA cm^{-2} , with Li utilization of 91%, Coulombic efficiencies of about 97%, and long lifespan of up to 3000 h. The analysis of structure evolution during charge/discharge shows inhibited lithium dendrite growth and a reversible electrode volume change of about 9% only.

Nonconductive host

As a nonconductive example, a polymer fiber Li metal composite anode was designed by infusing molten lithium into a surface treated polyimide polymeric matrix. The molten Li stable polyimide host was fabricated by using electrospinning. To gain the lithiophilic properties, the surface atomic layer deposition was applied to coat a several nano meters thick ZnO onto polyimide. The non-conductive polymeric skeleton Li composite can maintain a uniform lithium stripping/plating, which successfully regulated lithium ion flux, thus it suppressed Li dendrites and improved CE. The porous electrode also can reduce the effective current density. Thus, a flat smooth voltage profiles and stable cycling can be achieved more than 100 cycles under high current density of 5 mA cm^{-2} in both carbonate and ether electrolyte.²⁶

A electric nonconductive and Li-ion conductive SiO framework was developed host for Li metal. The SiO framework fulfilled with Li deliver a Li-SiO reacted capacity contributed composite. Pre-formed $\text{Li}_x\text{Si-Li}_2\text{O}$ composite delivered protection on embedded Li by provide shells to avoid exposure Li in electrolyte. The SiO framework also provide a enough space to accommodate volume change during cycling. Thus, a uniform Li nucleation and deposition can be achieved owing to the distinguished active Li domains and framework. Li-SiO 3D framework display a low over potential, good cycling performance in carbonate electrolytes.⁷¹

As another nonconductive Li storage host, the anodic aluminum oxide (AAO) membrane was applied to confine the Li ion flux.⁷² Unlike planar Li foil electrode, the AAO covered

electrode reach a greatly improved CE and good cycling performance. Li^+ flux was successfully confined, which result in a homogeneous Li distribution above the AAO modified Li metal electrode.

1.6 Rationale of Li metal modification

To overcome the above challenges and still retain a relatively high energy density and good cycling performance. The main requirements of Li metal anode modification will be proposed.

- Pre-stored Li into an electrode is a prerequisite. Firstly, it can predefine the electrode as Li anode, which will have standard Li potential, no sacrifice for the cell voltage. Secondly, it also supplies the Li source—especially for those high energy density battery systems without Li, such as Li-air and Li-S. Moreover, the Li metal exist inside anode can minimize sacrifice the specific capacities.
- Dendritic/mossy Li suppression is one of the most important prerequisite. Dendritic Li is considered as most safety concern for application of Li metal. Even the limit current density for Li dendrites growth is far below the average cell operation current densities, to minimize the possibility for growing Li dendrites under extreme cell operation is still necessary. The dendritic/mossy Li suppression can also reduce the impact of infinite volume expansion to an acceptable level.
- Uniform Li electrodeposition is also a critical factor for high performance Li metal anode. It can reduce the effect of uneven Li distribution and volume expansion. The key factors for uniform electrodeposition are reduction of the energy barrier of electrodeposition and to lower down the effective current density.
- SEI Stabilizing is another most important principle for optimizing lithium metal anode. A rational design of Li metal anode has to consider the SEI stabilizing. A stabilized SEI can

reduce the consumption of Li ion and other components in electrolyte and essential effect for stable cycles.

- Reversible Li plating/stripping and high CE is ultimate goal for Li metal anode. It is most in need of possession property and the most challenging to achieve for Li metal anode. It is based on a comprehensive solution of infinite volume change and controllable SEI.

CHAPTER 2 Design Strategies and Preparation of Li Metal Anode with Dendrite Suppression, Stable Interface and Improved Cyclability

2.1 Introduction

To mitigate the Li dendrites growth in Li metal anode, several strategies were introduced in this chapters. For instance, it was introduced an electrically conductive buffer layers including carbon fiber fabrics and novel 2D materials MXene at surface of Li metal, which can reduce effective local current densities. As another strategy, especially for the SEI stabilization, an electro-chemo-mechanical performance enhanced artificial SEI is proposed to replace the weak conventional SEI. If the volume changes in Li cycling was effectively mitigated, the dendrites growth is effectively suppressed. Therefore, an enhanced CE in Li metal anode will be accompanied by good cycling performance. To achieve these designs, the thermal based physical treatment, traditional cold work materials processing-rolling and wet chemical treatment were applied for Li metal electrode preparation.

2.2 A lithiotropic mass controllable conductive Li-carbon fiber fabrics (LiCFF) composites design

2.2.1 Design principle of LiCFF

As mentioned in rationale of Li metal modification, a rational design for lithium metal anode should contain mass controllable pre-stored lithium. It is important for lithium metal anode has lithium source for lithium poor high-energy-density cathode materials (such as Li-S⁷³

and Li-O₂⁷⁴ systems). The controllable mass of lithium not only can save the anode space for higher volumetric capacity battery designing, but also can economize the production cost. More importantly, to address the infinite volume change can greatly reduce the low CE effect and stabilize SEI layer. A mass controllable pre-stored lithium stable host will be solving most problems in lithium metal anode. An exciting research direction, the lithiophilic host materials with excellent mechanical properties and highly stable under electrochemical reaction in electrolyte have been introduced recent years (Carbon fiber, graphene, polymer, metal foam and carbonized wood).^{25,75,76} But all these works are molten lithium completely infiltrated and the entire surface of the hosts are covered with lithium metal. It means lithium electrolyte interface are still same with 2D surface of bare lithium, even they can well addressed volume change issue, but it cannot solve the unstable SEI problems. Besides, 3D framework matrixes were reported to reduce the effective electrode current density, minifying the plating/stripping volume change and Strengthening SEI.^{72,77-79} But proprietorial 3D framework matrixes have no pre-stored lithium, so that cannot supply the lithium source for lithium poor Li-S and Li-Air systems.

In this sub-chapter, we developed method to control the Li mass loading. It also has single-side Li-infused carbon fiber fabric structure. The comprehensive results exhibited an excellent reversibility of Li plting/stripping, and it has a low overpotential of less than 30 mV over 3000 cycles at current densities of 1mA/cm². Carbon fiber has excellent electrical conductivity of 9.09×10⁴ S/m, and higher surface area in carbon fabric than Li plate result in a uniform current distribution, thus forming a homogeneous, stable Li deposition/disslution instead of dendrites.

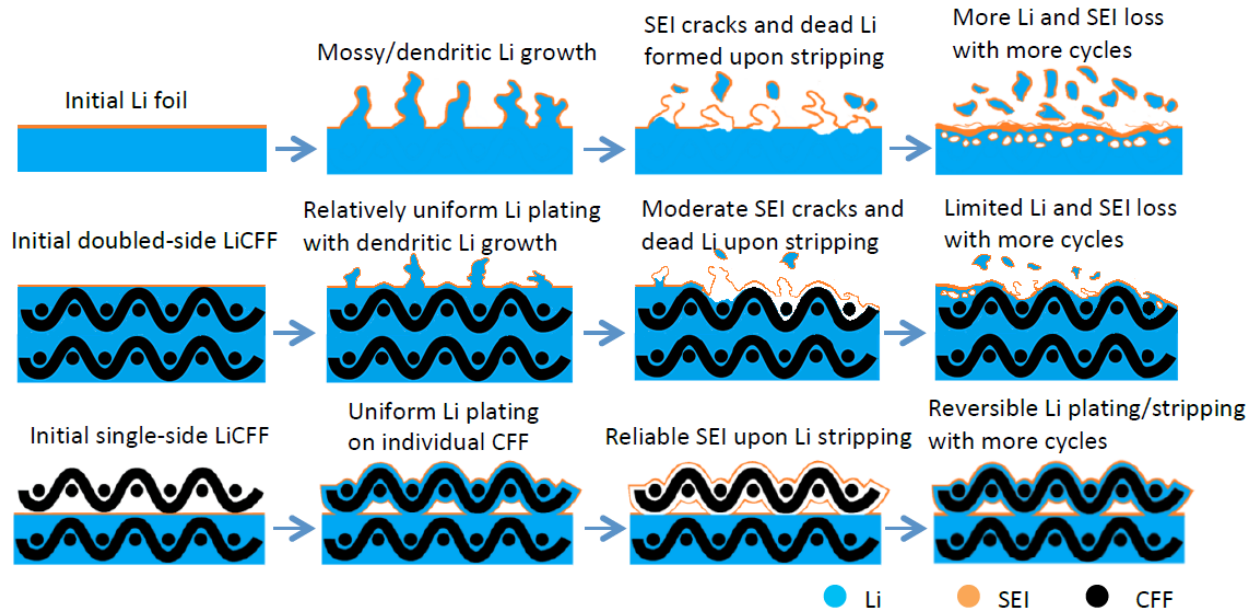


Figure 2. 1 Mechanism of Li plating/stripping on Li foil, single-side and double-side infused LiCFFs. Illustration of mossy/dendritic Li nucleation/growth on Li foil, single-side and double-side infused LiCFFs.⁴¹

Figure 2.1 illustrates the Li plating/stripping behavior on Li foil, double-side infused LiCFF and single-side infused LiCFF. At initial stage, Li foil leads to mossy/dendritic Li growth during plating/stripping. Li ions need large driving force (overpotential) to penetrate the preformed SEI during the plating and stripping, which owing to increasing of the local current density at specific locations and then growing out more mossy/dendritic Li (Figure 2.1). The uneven local current induce irregular Li forming at interface, then SEI damage/deformed at passively selected locations to form porous structure. When cycling numbers increasing and charging/discharging rates increasing, the Li foil interface suffers drastic volume change and morphological destruction (Figure 2.1). These expanded Li will disconnect with Li bulk substrate, thus ‘dead’ Li form at interface, which will sacrifice the active Li anode materials for batteries operation. Also the continuous exposed fresh Li will further consume electrolytes to create a new

SEI until the electrolyte depleted. For the double-side LiCFF, the irregular SEI and mossy/dendritic Li still can be formed at surface of electrode-electrolyte interface. The Li will evenly be deposited at CFF host surface. There is no room to adapt to the deformation which will eventually lead to a worse Li distribution at interface. However, the single-side LiCFF with both Li-rich and Li-poor sides will perform reliable Li plating/stripping along with a CFF host, and enough space in li poor-side will effectively accommodate the volume change (Figure 2.1).

2.2.2 LiCFF electrode preparation.

The LiCFF electrode preparation was conducted by infusing molten Li into one side of carbon fiber fabric (CFF), we also call it ironing process (showed in Fig.2.2). In an ironing case, a round 16 mm diameter CFF disc has weight of ~20 mg, density of 1.75-1.77 g/cm³, tensile strength of 192.5 kN/cm², electrical resistivity of 1.1x10⁻³ Ω cm, carbon content of 99.5%. The CFF is ordered from AvCarb 1071 HCB. Before LiCFF fabrication, CFF was pre-stored in an argon-filled glove box (H₂O: <0.5 ppm, O₂: <0.1 ppm, LABstar^{pro}, MBraun) over 24 hours. A bulk of Li metal with purity of 99.9% from MTI Corporation was placed on a stainless steel sheet, and then Li metal was heated up to 275 °C by a hot plate (Thermo Scientific Super Nouva⁺) until Li was completely melted. One polished side of stainless-steel disc was then dipped into molten Li until molten Li fully immersion the stainless-steel disc spacer. Then the stainless-steel spacer attached with molten Li was carefully transferred to CFF disc. Subsequently a carbon fiber ironing process was conducted via pushing the spacer with molten Li into the CFF. The spacer 'ironing' was pushed round trip until it gained default loading amount of Li or N/P ratio. For instance, it usually takes 15 to 60 seconds to load 1-10 mg Li into CFF (Showed in Fig. 2.3). After the ironing, the LiCFF was glove-box atmosphere cooled down to room temperature. The

prepared LiCFF was used to morphology characterizations and symmetric cell or full cell assembly.



Figure 2. 2 Ironing process lead to a limited/controllable molten Li infusion to single side CFF.⁴¹

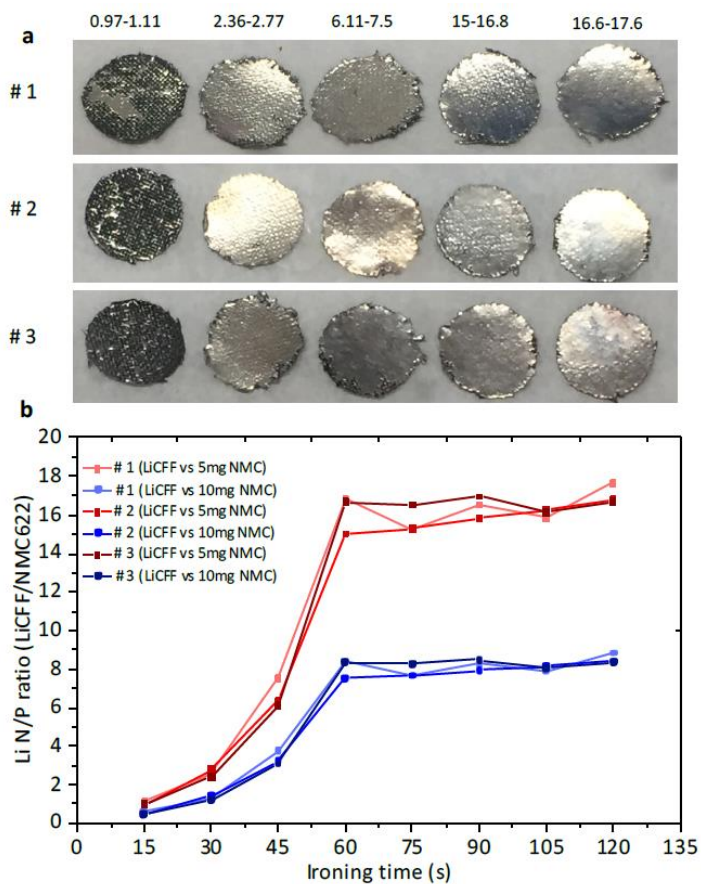


Figure 2. 3 Li loading control experiments of LiCFF.⁴¹

2.3 Rolling $\text{Ti}_3\text{C}_2\text{T}_x$ MXene into Ultrathin Li Metal: Inter-layer-calated Li (ILC-Li) Anode

2.3.1 Design principle of ILC-Li electrode

Considerable efforts on both conductive^{25,27,76} and nonconductive^{26,77} Li hosts engineering were applied on minimizing volume change by reducing effective current densities and regulating electric-electrochemical field for Li deposition and dissolution. One of the most popular host carbon materials with different forms such as graphene oxide²⁵, carbon nanofibers^{27,80,81} and carbon fabrics⁸² have been verified to be owned pretty good performance paired with Li metal, due to several advantages including stable in Li ion redox environment, has conductive scaffold structure and excellent mechanical properties. However, the relatively large interlayer/interfibrous spacing limited its effect current densities reduction. Besides, the amorphous carbon doesn't provide the graphite-like intercalation Li storage. Another popular host metal materials such as copper²⁹ and nickel^{69,78} has Kirkendall-type diffusion corrosion⁸³ caused permanent Li depletion. For nonconductive polymer host, only regulating Li ion flux can be achieved.

Ionic and mass transport in interfacial diffusivity and conductivity depends on geometry tortuosity. In order to minimize the rising resistance by introducing buffer layer, the tortuosity effects of structure is vital considerations from charge and mass transport perspective. So we propose to apply the several 2D materials such as graphene, MXene, MoS_2 flakes as the buffer layer between the electrolyte and Li metal.

MXene as potential flawless host materials for Li metal has several advantages⁸⁴, including high surface area interlayer spacing for Li storage, existence of cation intercalation Li

storage and stable paired with Li metal. $\text{Ti}_3\text{C}_2\text{T}_x$ MXene as one of most popular 2D materials has unique stacked layer by layer morphology, which can enable the fast Li ion flux for diffusion and insertion/intercalation channels⁸⁵. This excellent Li cation flux channel not only delivers significant reducing in effect current densities, but also regulating the Li flux for minimizing the volume change in Li metal anode. The MXene as high capacity electrode materials has been simulated with 447.8 mAh g^{-1} ⁸⁶. At beginning Li plating, as high as experimentally specific capacity of 225 mAh g^{-1} ⁸⁷ enabled considerable intercalation⁸⁸ Li storage. The Li intercalated MXene also can not only serve as Li storage host but also provide a Li deposition preference interface. The fast-interfacial Li ions transportation emerged stable Li nucleation play a critical role for uniform Li deposition. Then, up to hundreds nm gap interlayers in exfoliated MXene can provide sufficient space and surface area for Li deposition with ultimate low effect current densities by utilizing its 2D materials high surface area nature. The single-flake $\text{Ti}_3\text{C}_2\text{T}_x$ MXene nanosheets have already been reported⁸⁹ as parallelly aligned surface coating to lead horizontal Li growth in lithium metal anode. However, the pristine MXene without delaminating process is not been applied in Li metal anode. In this chapter, we report a non-delaminating $\text{Ti}_3\text{C}_2\text{T}_x$ MXene coated on an ultrathin Li metal, which serve as hybrid interlayer and intercalation Li storage with self-exfoliated phenomenon during cycling, also called inter-layer-calated Li (ILC-Li). The 30 micron thickness ultrathin pre-stored Li plus 15 micron MXene coating layer with capability of providing ~ 1.5 areal capacity ratio of negative to positive electrodes (N/P ratio) full cell displayed excellent cyclability at $\sim 5 \mu\text{l mAh}^{-1}$ lean electrolyte condition. The excellent conductivity of laminated MXene not only furnished uniform current distribution, but also regulated Li ion flux during cycling. The designed ILC-Li metal anode revealed excellent cyclic retention improvement in full cell paired with both NMC and NCA.

2.3.2 Fabrication of the ILC-Li electrode.

Ti_3C_2 MXene as a ceramic material, it doesn't have 'lithiophilic' property, and the thermal stability of MXene is still not well known. Thus, the thermal infusion process will not be used as ILC-Li composites synthesis. A facile cold rolling process is applied to deposit a micron level thickness MXene over Li metal. The process of rolling and the digital camera optical and transmission electron microscope (TEM) images of ILC-Li are showed in Figure 3.1.

The $\text{Ti}_3\text{C}_2\text{T}_x$ MXene was synthesized via HF etching method. 3g of Ti_3AlC_2 MAX (Forsman, China) was gradually added into 30ml HF solution (48-52%, Sigma-Aldrich) in a Teflon container with 30 minutes magnetic stirring. Then, Teflon container was transferred to 60 °C water baths for 1 hour stirring until temperature reached. Following by 24 hours stirring, the sediment was centrifuged and washed by DI water until pH decreased to 6. $\text{Ti}_3\text{C}_2\text{T}_x$ MXene was collected by using 0.22 μm pore size PVDF membrane vacuum filtration and vacuum drying at 80 °C for 24 hours. The 100 μm Li foil (Goodfellow) was rolled to 30 μm by stainless steel roller in a surface smoothed stainless-steel plate. The binder free non-delaminated MXene was mixed with N-methyl-2-pyrrolidinone solution (Sigma-Aldrich) and then coated on copper foil with 1.56 mg/cm^2 or 3.12 mg/cm^2 mass loading. The coated MXene coated copper foil was paired with 30 μm or 300 μm Li foil sealed with PET Mylar film inside Argon filled glovebox. The stacked configuration of Mylar film|MXene coated copper foil|Li foil| Mylar film was uniformly pressed by a rolling mill at 2rpm (Figure 3.1). Then, the Mylar film and copper foil were removed inside glove-box. Finally, ILC-Li electrode was collected.

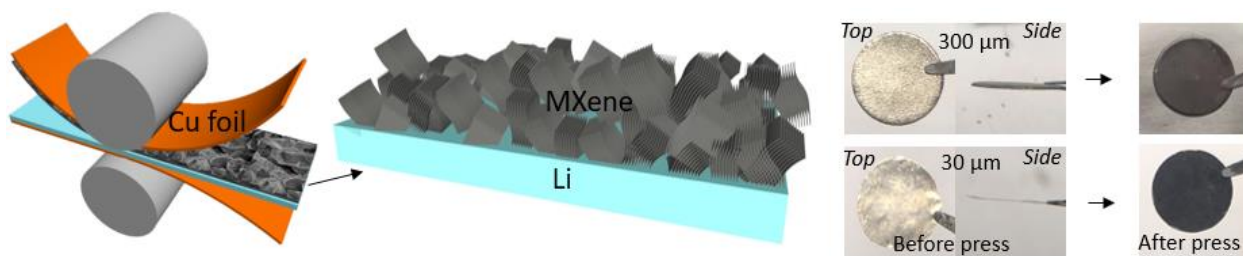


Figure 2. 4 Rolling process for ILC-Li fabrication and images of thin Li foil and digital images of Li foil, ILC-Li top/side view, respectively.⁹⁰

2.4 An electro-chemo-mechanical stable artificial pre SEI design for high performance Li metal

2.4.1 Design principle of reinforced artificial SEI coated Li metal

Recently, a facile designed reactive polymer poly(vinylsulfonyl fluoride-ran-2-vinyl-1,3-dioxolane)-graphene oxide composite derived SEI was reported as a protection layer to exhibit the Li dendrites growth even under lean electrolyte conditions.⁹¹ Also, a lot of literatures reported fluorinated⁹²⁻⁹⁴ and lithium nitride^{95,96} containing inorganic SEI as a widely approach to stabilize the Li metal anode since LiF or Li₃N are excellent electron insulator and ionic conductor. The existing of inorganic lithium compounds effectively prevents electron tunneling and provides fast Li ion diffusion in parallel rather than vertical manner. However, the researcher also found that the large dimension (100-400nm) LiF cannot contribute to the Li ion transport in SEI.⁹⁷ Thence, to redesign or refine inorganic part in SEI need to be considered in electro-chemo-mechanical stable SEI developing. Some recent reported literature indicates that the tuned organic-rich SEI also have great potential to prevent the Li dendrites formation. An artificial SEI based on poly(vinylsulfonyl fluoride-ran-2-vinyl-1,3-dioxolane) (P(SF-DOL))-graphene oxide

(GO) nanosheets covered Li metal⁹¹ exhibit the better batteries performance than conventional SEI Li metal batteries even under low temperature conditions.⁹⁸

In this chapter, we synthesized an artificial SEI with organic and inorganic components above the Li metal surface. The organic component of artificial SEI layer has sufficient ionic conductivity and high fracture toughness to tolerate the interfacial morphology change in Li metal. The inorganic component of artificial SEI layer contains excellent electron insulator and ionic conductor nano fillers such as LiF, Li₃N and Li containing salts to avoid electron tunneling effect (Figure 4.1). The synthesis process must be in-situ formed at Li metal surface without voids and defects. Then, the artificial SEI must retain higher ionic conductivity and better insulation than conventional SEI. Also, artificial SEI need to gain enough mechanical properties to survive Li metal infinite volume change.

In this artificial SEI development, it is fabricated by introducing the products from chemical reaction between Li metal and diluted nitrile solvents (typical acetonitrile), so that no voids and defects at in-situ formed polymer-Li interface due to on-site interface reaction. A poly-amino nitrile thin film will be seamless bonded to Li metal via in-situ reaction. In additions, the in-situ formed products including the Li₃N Li_xNO_y and LiCN can provide the excellent electron insulator and ionic conductor. Reaction between acetonitrile (ACN) and Li metal is very violent process. To minimize the reaction rate, LiTFSI will be dissolved into ACN for this coating process. To control the thickness of the artificial SEI, the diluted ACN contained solution will be applied as precursor to dip coating on Li metal. The one typical Li ion batteries electrolyte using hydrofluoroethers (HFE), 1,1,2,2-tetrafluoroethyl 2,2,2-trifluoroethyl ether will be used to dilute the LiTFSI contained ACN solution. The diluted nitrile-fluorinated solution Li metal reaction lead to forming this electro-chemo-mechanical stable reinforced artificial SEI. This reinforced

artificial SEI with high modulus organic components and a few nanometers level inorganic components will serve as ionic conductive buffer layer to inhibit the Li dendrites growth.

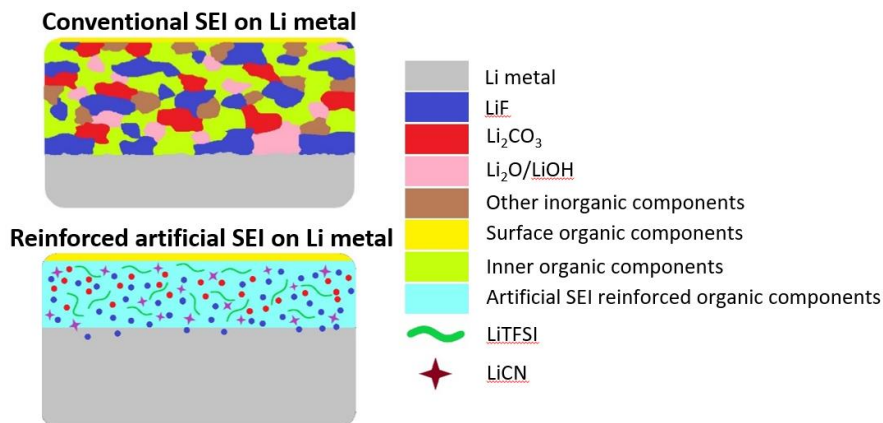


Figure 2. 5 Schematic comparison of conventional SEI and reinforced artificial SEI upon Li metal.

2.4.2 Fabrication of reinforced artificial pre SEI coated Li metal

The 100 μ m Li foil (Goodfellow) was carefully polished by brass brush to remove the surface impurities, then followed by rolling process for surface smoothing. 1.0 M lithium bis-trifluoromethane sulfonimide (LiTFSI, BASF Corp) was dissolve in ACN (HPLC grade, >99.9%, Sigma-Aldrich) to form 1M LiTFSI-ACN solution. The different volume portion (5%, 10%, 20%) of 1M LiTFSI-ACN solution was mixed with 1,1,2,2-tetrafluoroethyl 2,2,2-trifluoroethyl ether (HFE) to form nitrile-fluorinated precursor. In typical experiment, the 30 μ l 10% 1M LiTFSI-ACN in HFE dropped on 1.56 cm diameter Li metal disc to form the reinforced artificial SEI-Li (The precursor loading: $\sim 15.7 \mu\text{l} / \text{cm}^2$). The reacted Li foils were placed in open argon atmosphere over night. For pure ACN and Li metal reaction experiment, 60 μ l of ACN were dropped on polished and rolled Li foil surface and leave the reacted Li foil over night. All

experiments were conducted inside a Argon filled glove-box (H_2O : <0.5 ppm, O_2 : <0.1 ppm, LABstar^{pro}, MBraun).

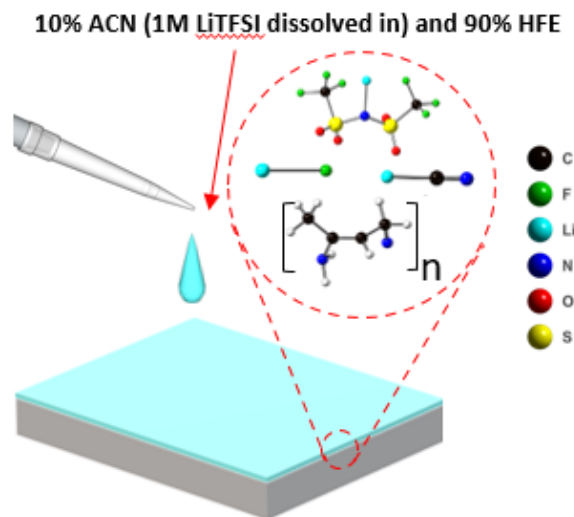


Figure 2. 6 Schematic of drop coating process for producing reinforced artificial SEI-Li electrode.

Chapter 2 is a reprint of the publication “Chen, X., Lv, Y., Shang, M. & Niu, J. Ironing Controllable Lithium into Lithiotropic Carbon Fiber Fabric: A Novel Li-Metal Anode with Improved Cyclability and Dendrite Suppression. *ACS Applied Materials & Interfaces* 11, 21584–21592 (2019)” and “Chen, X., Shang, M. & Niu, J. Inter-layer-calated Thin Li Metal Electrode with Improved Battery Capacity Retention and Dendrite Suppression. *Nano Lett.* **20**, 2639–2646 (2020)”, copyright of American Chemical Society. The dissertation author is the first author and co-writer of this publication. Chapter 2 is also a reprint of the manuscript under preparation “Chen, X., Shang, M. & Niu, J. An electro-chemo-mechanical stable artificial pre SEI design for Li metal anode with enhanced batteries performance.”, The dissertation author is the first author and co-writer of this manuscript.

CHAPTER 3: Multiscale Characterization of Modified Li Metal Anode with Dendrites Suppression and High Reversibility

3.1 Multiscale Characterization of LiCFF

3.1.1 Multiscale characterization of pristine LiCFF

Several reports using lithiophilic hosts including reduced graphene oxides (rGO),²¹ atomic deposited zinc oxide on polymer fibers²² and silver nanoparticles seeded carbon fiber²³ exhibited fast infusion rate by strong driving force. In these reports, the whole piece of Li host will be infused with molten Li, which lost the Li loading controlling ability. CFF have no chemical driving force at surface to enhance the capillary force, which result in a ‘lithiotropic’ properties. Lithiotropic means properties of less lithiphilic, but not lithiophobic. The properties of lithiotropic makes Li infusion process a slow process, therefore a mass loading controllable process. In Fig. 2.4a, it showed the ironing process for single-side CFF infusion and digital images of lithium-poor side and lithium-rich side in. Further confirming by scanning electron microscopy (SEM) images (Fig. 2.4b), lithium infused in lithium-rich side only and lithium-poor side remained the original appearance of the carbon clothing. The surface texture conforming to the orientation of single CFF provides capillary force to closely attach the molten lithium (Fig. 2.4a). The top view SEM images (Fig. 2.4c-e) of carbon clothing-Li also is a strong evidence for dense structure in lithium-rich side, which indicated seamless contact in carbon-Li interface and maximum space utilization. Besides, flawless weaving structure with 10 μm diameter carbon fibers keeps the original framework in both lithium-poor and lithium-rich sides. According to the

cross-section SEM images (Fig. 2.4b), the entire thickness of carbon clothing-Li electrode is about 300 μm and lithium-rich side is about 120 μm . And lithium-rich and lithium-poor sides have a clear interface with acceptable depth fluctuation. Furthermore, variety of thicknesses can be effectively control the amount of lithium infusion process. (in Fig. 2.5) Therefore, amount of excess lithium is controllable based on lithium capacity of the counter electrode.

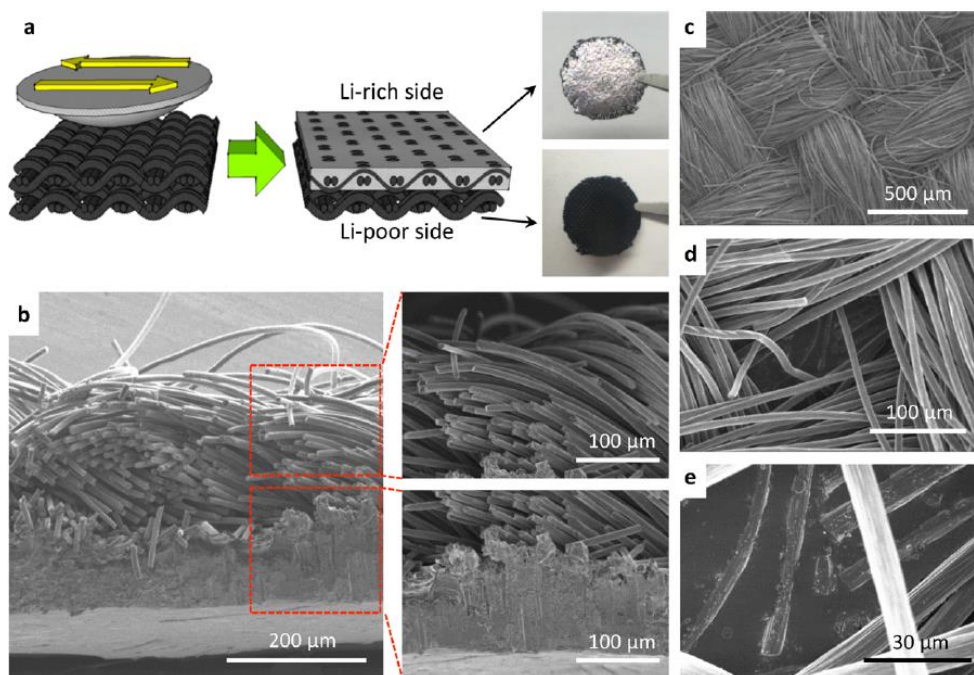


Figure 3. 1 Fabrication and morphology of the LiCFF electrode. Schematic of ironing molten lithium into CFF to form the LiCFF electrode. The insets show the Li-rich (top) and Li-poor (bottom) sides of the sample after ironing and SEM cross-section images.

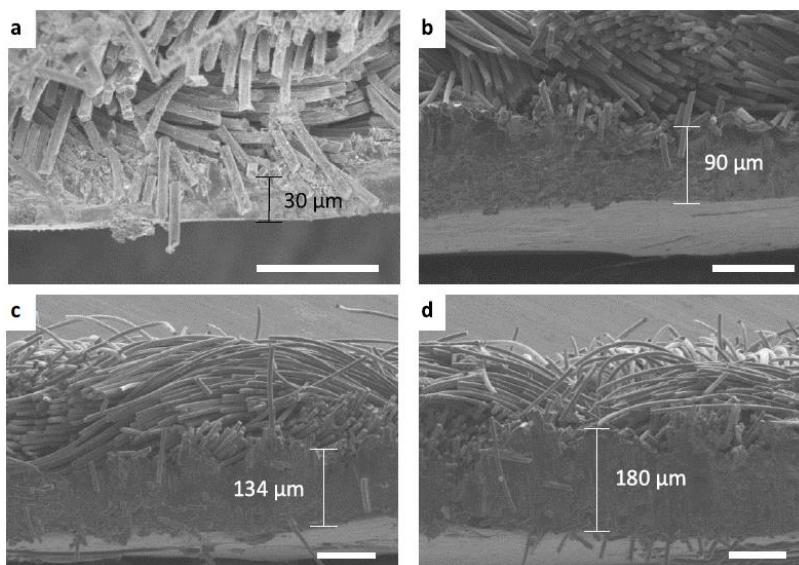


Figure 3. 2 LiCFF with variety of Li loading and thickness.

The thermogravimetric analysis (Fig. 2.6e) indicates that CFF is high purity carbon materials without any impurity doping and thermal stable up to 600 °C. Such high thermal stable temperature provide guarantee, that CFF can well undergo the molten lithium infusion process. The Raman spectroscopy characterization (Fig. 2.6c) resolved that CFF has no degree of graphitization. The ratio of D band and G band higher than 1 demonstrated that CFF has amorphous structure, which further revealed by X-ray diffraction (XRD) spectra of CFF in Fig. 2.6b. The Raman shift and XRD spectra results well defined that CFF can only contribute as a conductive lithium host. The XRD spectra of lithium infused CFF manifested high purity lithium remained after molten lithium infusion process. In Fig. 2.7, the X-ray photon spectroscopy (XPS) C 1s peak and Li 1s peaks indicate existence of the surface diffusion in Li-CFF interface. The Kirkendall-type diffusion induced Li_xC formation, which produced Li^+ deposition preference at Li-CFF interface. Rather than surface chemical treated lithium host, the physical lithium infusion process in CFF did not introduce any extra elements except C and Li, which means no lithium

compounds involved in like Li_2O , $\text{Li}_{13}\text{In}_3$, LiZn , and Li-Si alloy. This ultra-high purity lithium avoided the side effects during electrochemical reaction. The LiCFF anode revealed an excellent mechanical performance owing to a high storage modulus of 15-16 MPa in CFF (Fig. 2.6d) as well.

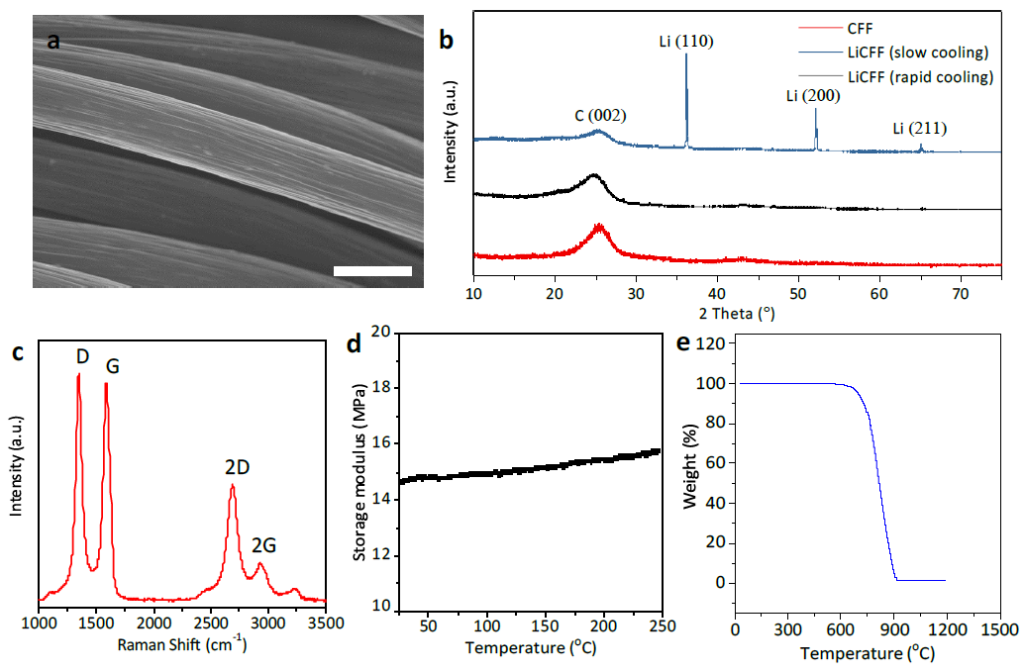


Figure 3. 3 Characterizations of the pristine CFF and LiCFF electrode.

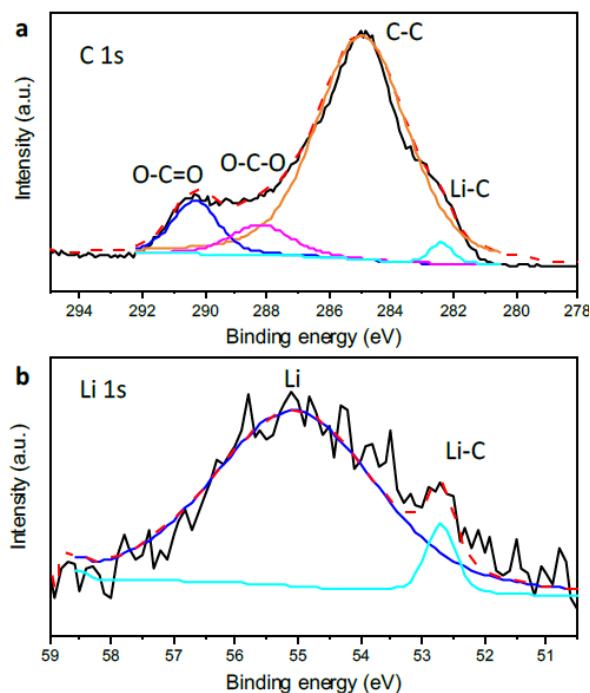


Figure 3. 4 XPS spectra of Li-CFF interface.

3.1.2 Morphology evolution of LiCFF after Li plating/stripping

The *ex-situ* morphology evolution in SEM of LiCFF was studied after 10th and 100th cycles of galvanostatic plating and stripping with carbonate-based electrolyte (1M lithium hexafluorophosphate (LiPF₆) in 1:1 volume ratio ethylene carbonate (EC): diethyl carbonate (DEC), BASF). Carbonate-based solvents with high voltage stability window and high conductivity, low internal resistance anode friendly lithium salt LiPF₆ were selected as electrolyte to conduct experiment for morphology characterization. SEM cross-section and top surface images of after plating/stripping process were captured from cycled symmetric cells under various current densities. Besides, the in-situ capillary cell observation experiments were used to record the movies for comparing the plating process of Li foil and LiCFF.

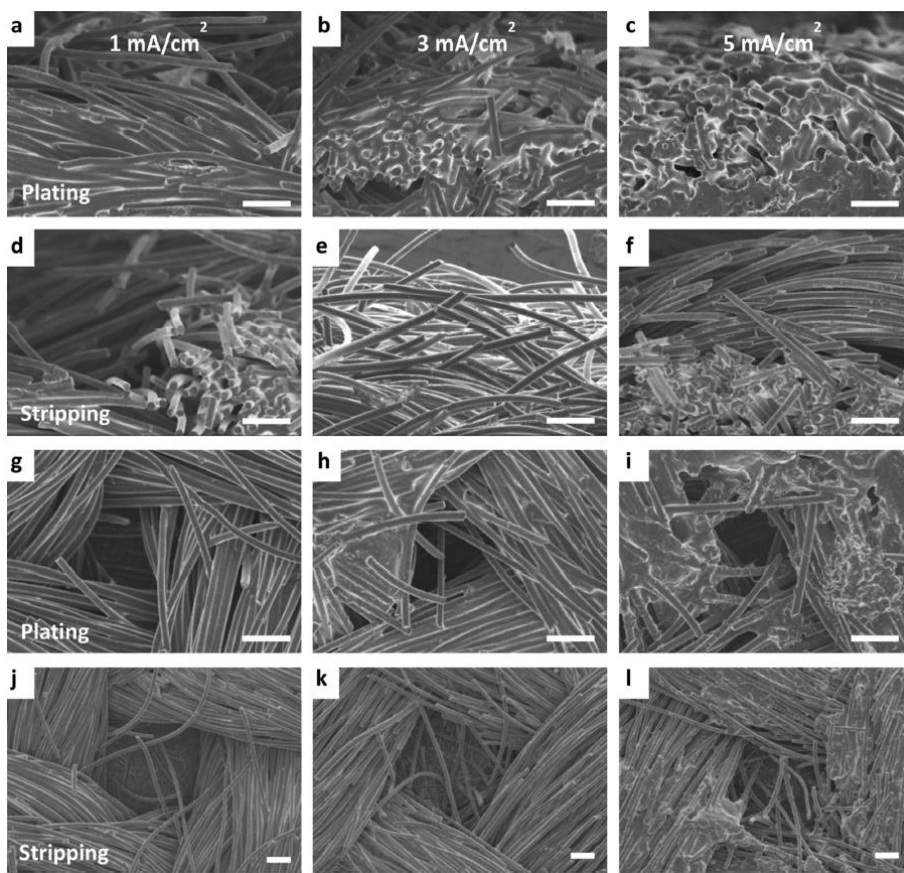


Figure 3. 5 Ex-situ morphology evolution of LiCFF after 10th cycle Li plating/stripping.

SEM cross-section images (Fig. 2.8a-f) (Fig. 2.9a-f) and top surface images (Fig. 2.8g-l) (Fig. 2.9g-l) showed morphology after 10th and 100th cycled plating/stripping under current densities 1mA/cm², 3mA/cm² and 5mA/cm². Compared with pristine CFF, there are clearly visible white edges along the CFF surface, corresponding to non-conductive solid electrolyte interfaces (SEI). According to morphology and size of these white fringe SEI layers, we can probably observe the evolution and amount of lithium metal remaining on the surface. Interestingly, we found no mossy/dendritic lithium growth at surface of CFF lithium 10th and 100th cycled under 1mA/cm², 3mA/cm². The lithium plating/stripping process strictly followed CFF morphology; lithium refilled the gaps among individual fibers after plating and the original

CFF fibers structure appeared again after lithium stripping. Even in SEM images at 5 mA/cm^2 , 100^{th} cycled samples; there are only mossy lithium growth founded at electrode surface and no dendritic lithium found. After careful comparison with plated samples, we also discovered stripped samples has low amount of lithium residues and more appeared as original CFF. It also explains the high reversibility of lithium plating/stripping process and dendrites free behaviors in carbon clothing-Li anode.

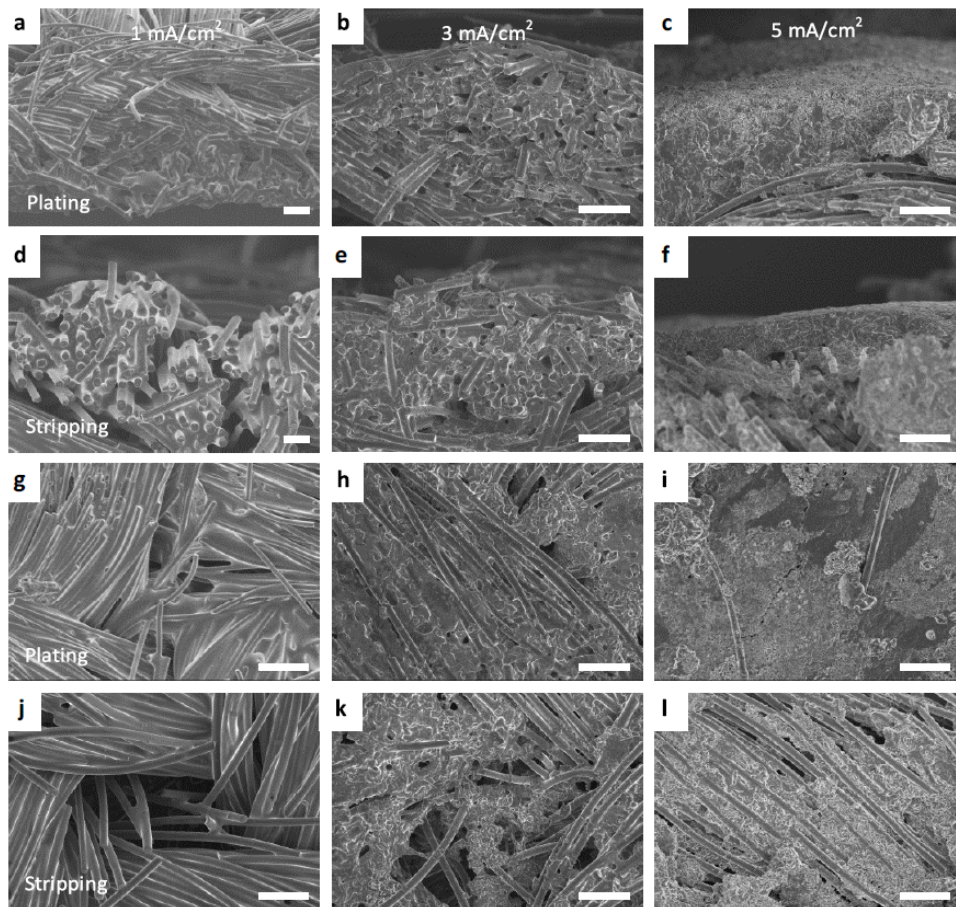


Figure 3. 6 Ex-situ morphology evolution of LiCFF after 100th cycle Li plating/stripping.

For more visual and intuitive observation, in-situ capillary cell was introduced to dynamic evolution observation for comparing the lithium plating performance between bare

lithium and LiCFF. The in-situ capillary cell experimental setup is illustrated in Fig. 2.10a. The estimated constant current density $3.53\text{mA}/\text{cm}^2$ was applied to capillary symmetric cells to electrochemical plating the lithium in bare lithium and LiCFF in parallels. The movies (Movie 2, 3) of bare lithium plating and LiCFF plating were recorded for comparing lithium deposition behaviors. From Fig. 2.10b, the bare lithium performed traditional mossy lithium growth within 14 minutes, which has relatively high-volume expansion and low reversibility. From Fig. 2.10c, we surprisingly found that lithium plating start from lithium source that beneath the CFF. Lithium uniformly deposited on CFF surface and gradually penetrates the CFF until mossy lithium growth appeared in surface. Compared with bare lithium, it takes more than 20 minutes to see the mossy lithium growth in LiCFF, also the rate of mossy lithium growth is much slower. This phenomenon could be strong evidence about that high conductive CFF surface delivered a much more uniform lithium plating process by lower local current density. When lithium penetrated from some specific sites, CFF still remained some internal sites can provide this low energy barrier plating among CFF gaps. So it greatly reduced rate of mossy lithium growth as well.

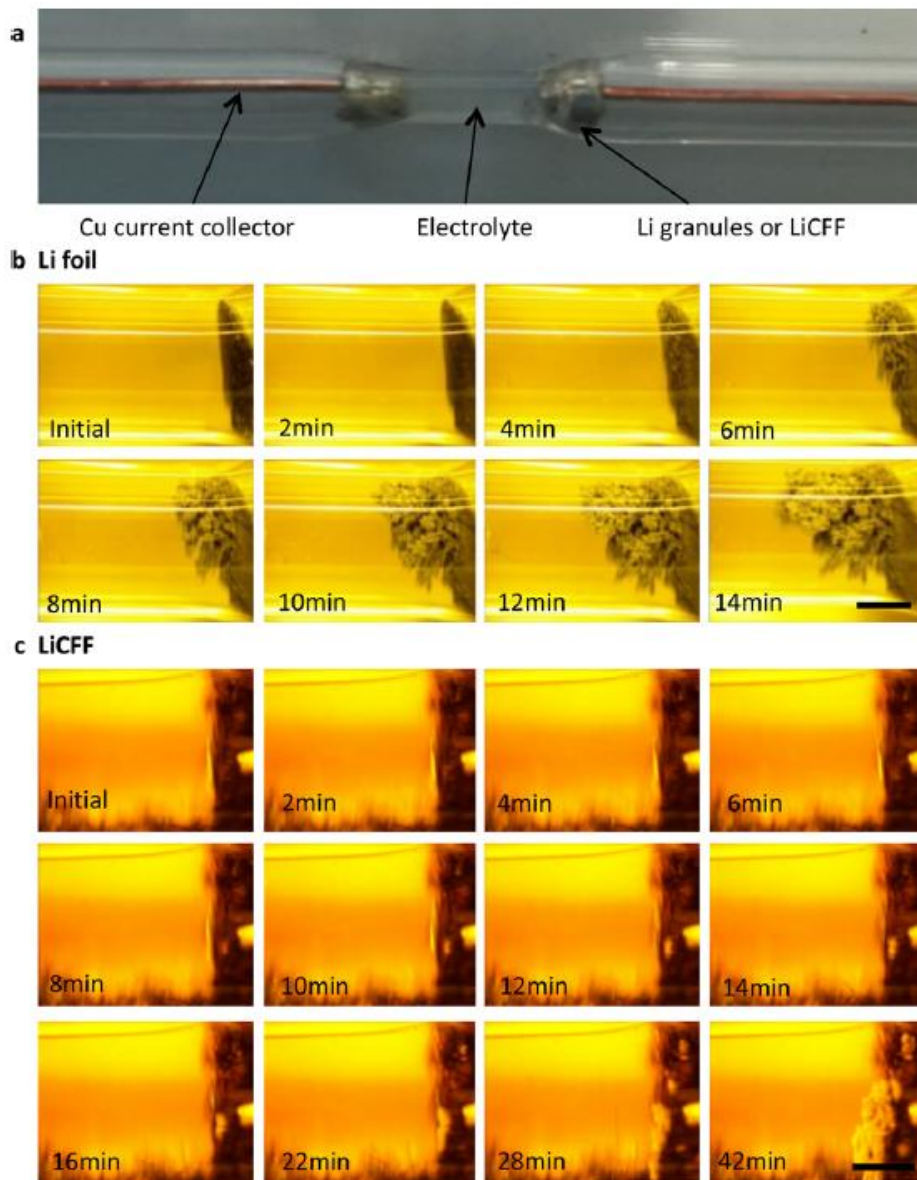


Figure 3. 7 In-situ capillary cell observation setup and Li plating morphology evolution comparison of Li foil and LiCFF.

According to ex-situ SEM and in-situ capillary cell characterization, the conductive and flexible CFF as an artificial interface greatly enhanced the lithium plating/stripping performance. Relatively high surface area helped LiCFF to maintained lower nucleation energy barrier for uniform lithium deposition by reducing the local current density. It enhanced lithium

reversibility by forming a stable SEI during non-mossy lithium growth induced relatively small volume change. The dendritic lithium growth is largely suppressed since decreased current density in local sites of CFF.

3.2 Multiscale characterization of ILC-Li

3.2.1 Morphology of MXene and pristine ILC-Li

Among all conductive hosts for dendrites-free Li deposition, non-delaminating $\text{Ti}_3\text{C}_2\text{T}_x$ MXene is attractive due to high electronic conductivity as $2.4 \times 10^3 \text{ S cm}^{-2}$ and promoted Li ion diffusion brought by lamination structure. The flexible lamination structure provides sufficient space to store and accommodate lithium as well. Firstly, the non-delaminating $\text{Ti}_3\text{C}_2\text{T}_x$ MXene was firstly synthesized by traditional hydrofluoric acid etching method and followed by sonication process. $\text{Ti}_3\text{C}_2\text{T}_x$ MXene has lamination structure with O, F, OH functional groups at surface (Fig 3.2a). The $\text{Ti}_3\text{C}_2\text{T}_x$ lamination structure was characterized by scanning electron microscope (SEM) (Fig 3.2b) transmission electron microscope (TEM) (Fig 3.2.c-d) and Energy Dispersive X-ray (EDX) (Fig 3.3a-d). Then, the binder free MXene was coated on copper foil for controlling thickness, which can be controlled at 15 to 30 μm based on loading from 0.78 mg cm^{-2} to 1.56 mg cm^{-2} . On the other hand, the distinguished advantage of Li foil is its highest specific capacity. However, exceed Li amount paired with counter electrode become the reason for limiting the overall energy density of the batteries.

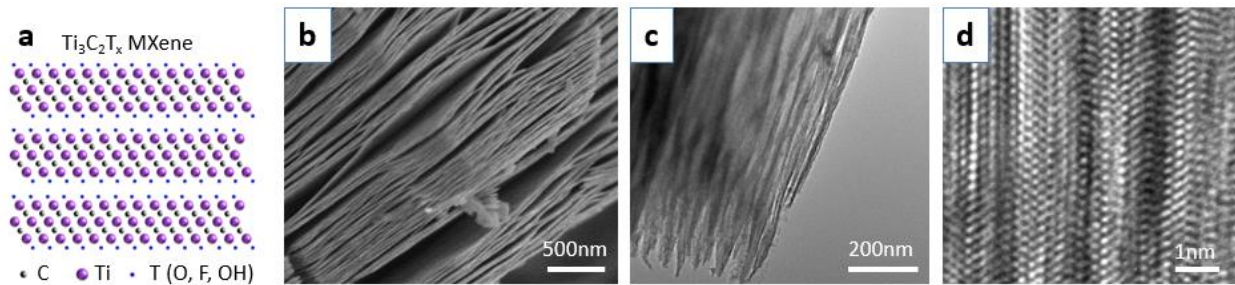


Figure 3. 8 Schematic of $Ti_3C_2T_x$ MXene and SEM images, TEM images and HR TEM images.

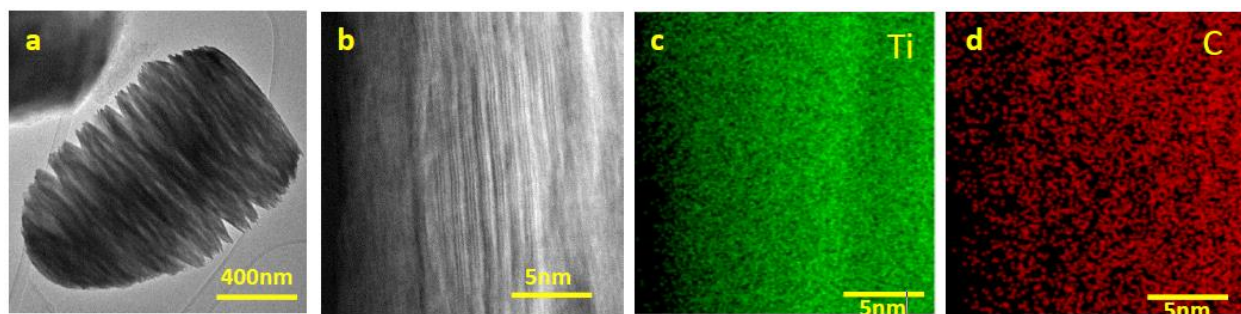


Figure 3. 9 TEM and STEM images of non-delaminating $Ti_3C_2T_x$ MXene and EDX mapping.

To meet a reasonable N/P ratio, the Li foil was vigorously rolled to its thinnest limit 30 microns. Then, the MXene coated copper foil was stacked to pre-rolled Li foil for rolling press. The rolling pressed ILC-Li cross-section morphology was showed by scanning electron microscope (SEM) including $\sim 330 \mu m$ thick ILC-Li electrode with $300 \mu m$ Li foil and $30 \mu m$ MXene loaded (Fig. 3.4a) and $\sim 45 \mu m$ thick ILC-Li electrode with thinnest Li foil of $30 \mu m$ Li and $15 \mu m$ MXene film (Fig. 3.4b). The stacked MXene film with block structure was tightly calendered into Li foil, which serves a high conductive interface for Li^+/e^- exchange. The MXene film not only can deliver a high surface buffering layer to decrease the Li deposition over potential, but also could contribute sufficient space to accommodate the volume change of Li plating/stripping at inter-block space. The zoom-in SEM image of exfoliated non-delaminated

MXene nanosheets (Figure 3.4c) microscopically demonstrates the benefits that high surface area lamination structure can reduce the effect current density. The interlayer spacing between nanosheets also exhibited the space to accommodation of volume change in Li deposition and dissolution.

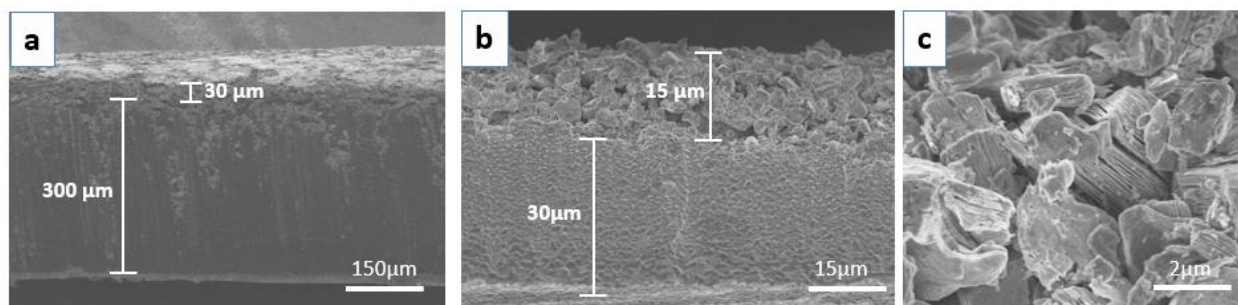


Figure 3. 10 SEM cross-section images of ILC-Li with 300 μm Li foil and 30 μm MXene loaded and 30 μm Li and 15 μm MXene film.

3.2.2 Mechanism of inter-layer-calation

In addition, an interesting phenomenon of Li intercalation resulted in increases of *c*-lattice parameter of non-delaminating $Ti_3C_2T_x$ MXene, which is measured by X-ray diffraction (XRD). The Figure 3.5a showed that pristine MXene coated Li sample has initial peak at 8.6° , which is corresponding to interlayer spacing of 1.02nm. After intercalation with Li or 1st Li plating cycles, the peaks were shifted to lower 2θ angles located at 6.5° , which is corresponding to interlayer spacing of 1.36nm. The high resolution TEM images (Fig 3.5b and Fig 3.5c) also confirmed Li intercalation induced interlayer spacing expand from 1.002nm to 1.344nm. The Li intercalation phenomenon indicated that interlayer space is a Li prefer location for Li plating and stripping as well.

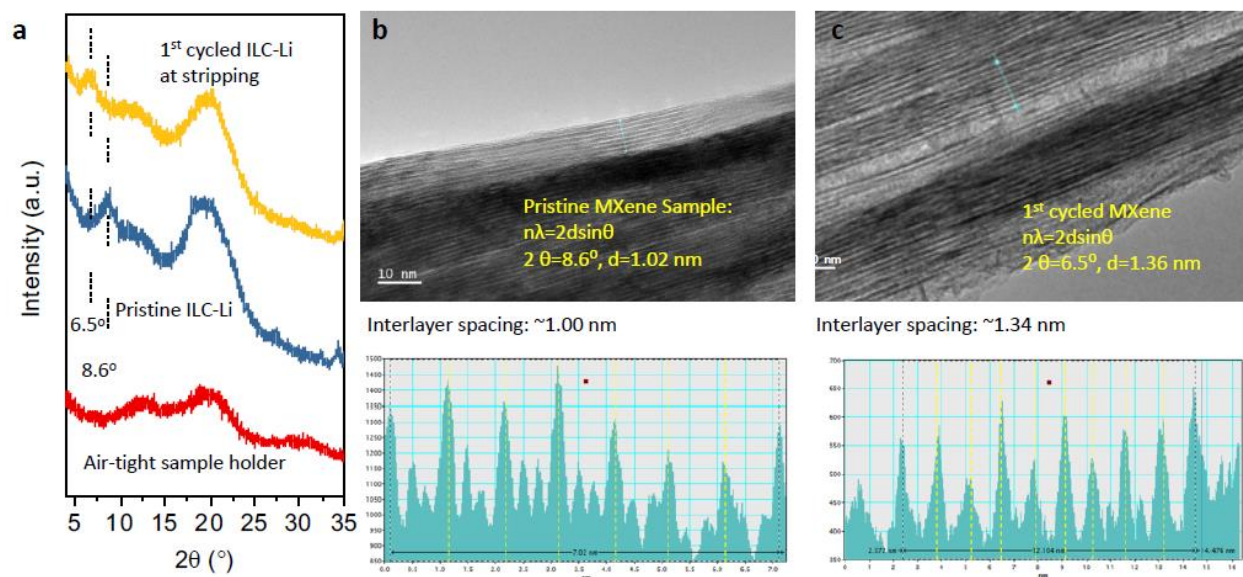


Figure 3. 11 Inter-layer distance expansion of MXene after cycling.

Inter-layer expansion phenomenon confirms the existence of inter-layer-calation Li metal storage in MXene stacks. There is periodic interlayer distance changing, which showed the deformation and damaged under high current density up to 5 mA/cm² (Figure 3.6a) or more cycles (Figure 3.6b) was applied. It should be noted that the irregular array of the (002) plane will not affect the Li insertion/extraction. It will instead increase the overall Li accommodation capability as well as the electrochemical property due to the further expanded volume.

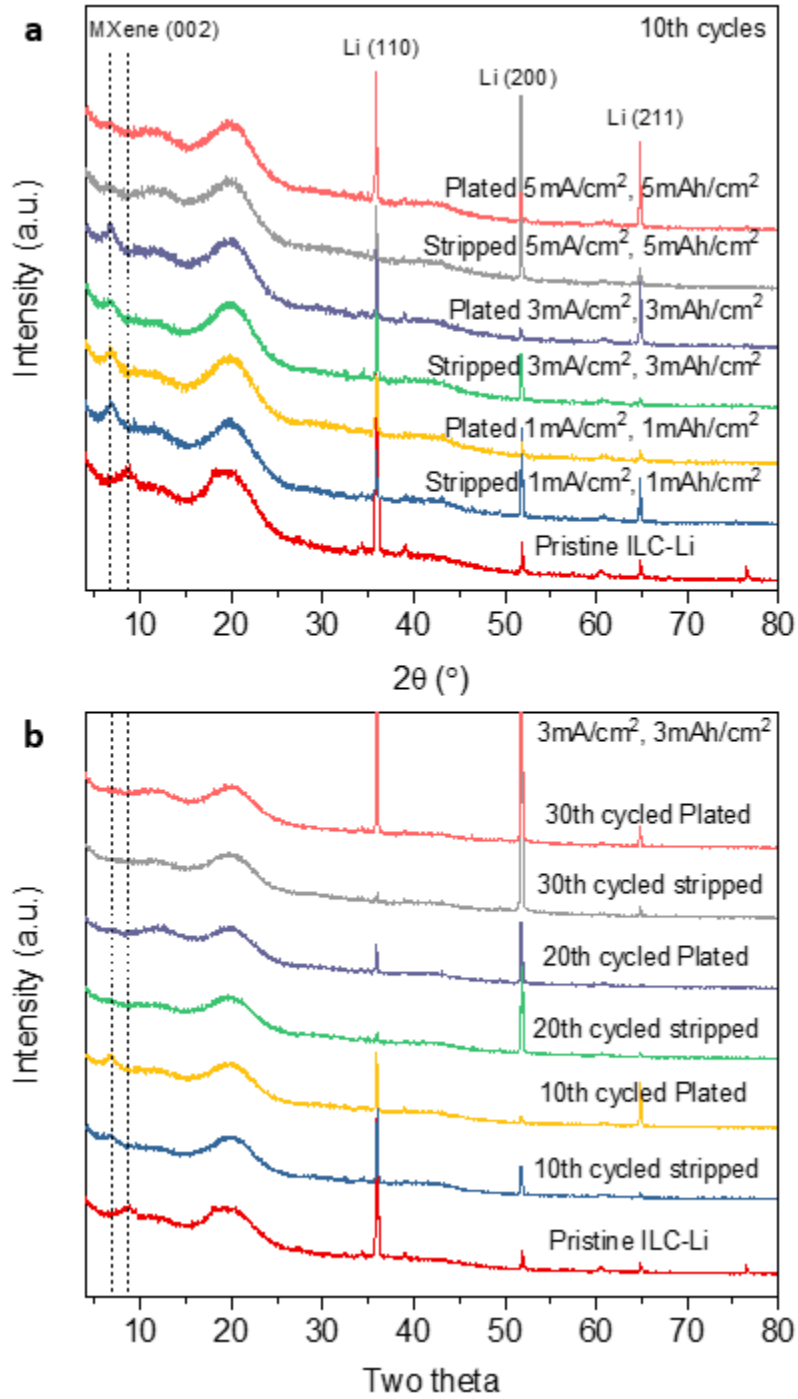


Figure 3.12 XRD patterns for showing the inter-layer expansion under different current density/cycling capacity and different cycle numbers.

3.2.3 Morphology evolution of ILC-Li electrode

Morphology evolution of non-delaminating $\text{Ti}_3\text{C}_2\text{T}_x$ ILC-Li electrode was investigated by SEM imaging, 3D confocal imaging and in-situ cycling observation at various current densities and different cycles in symmetric cells. The mossy/dendritic structure was found at Li foil sample after 10th cycles under current densities of 1mA cm^{-2} and 1mAh cm^{-2} (Figure 3.7a and e). It is very obvious appearance that Li was intercalated and plated at surface of lamination MXene nanosheets and efficiently used both interlayer and inter-block space, compared with mossy/dendritic growth in bare Li foil (Figure 3.7b-d and f-h). Li intercalated and deposited at surface of lamination nanosheets, further nucleated at surface of lamination Li-MXene at low current densities of 1mA cm^{-2} and low Li plating/stripping capacity of 1mAh cm^{-2} . As current density rise to $2\text{-}3\text{ mA cm}^{-2}$ and capacity increased to $2\text{-}3\text{ mAh cm}^{-2}$, Li deposition still occurred along lamination nanosheets surface until it fills up the inter-blocks space. The cross-section images (Figure 3.8) of MXene-Li interface after 10th cycles shows no gaps and fragmentation which corresponding to a uniform Li distribution. Meanwhile, the 3D confocal microscope imaging was applied for surface roughness measurement. According to $600\text{ }\mu\text{m}$ wide square area 3D surface images, pristine Li foil (Figure 3.7i) showed area roughness of 0.535 Sq (Root mean square height) (μm) while pristine ILC-Li (Figure 3.7k) display 0.922 Sq (μm). After 10th cycles, area roughness of Li foil (Figure 3.7j) electrode rise to 4.14 Sq (μm) while ILC-Li electrode (Figure 3.7l) exhibit an excellent area roughness of 0.692 Sq (μm). It showed that ILC-Li regulated Li ion flux during cycling, resulting in uniform Li deposition/dissolution. It also demonstrated that Li metal has extremely irregular mossy/dendritic Li deposition compared to ILC-Li. Also, the large surface area of $5.61\text{ m}^2/\text{g}$ (Figure 3.9) among the MXene stacks film provide sufficient space for Li metal storage.

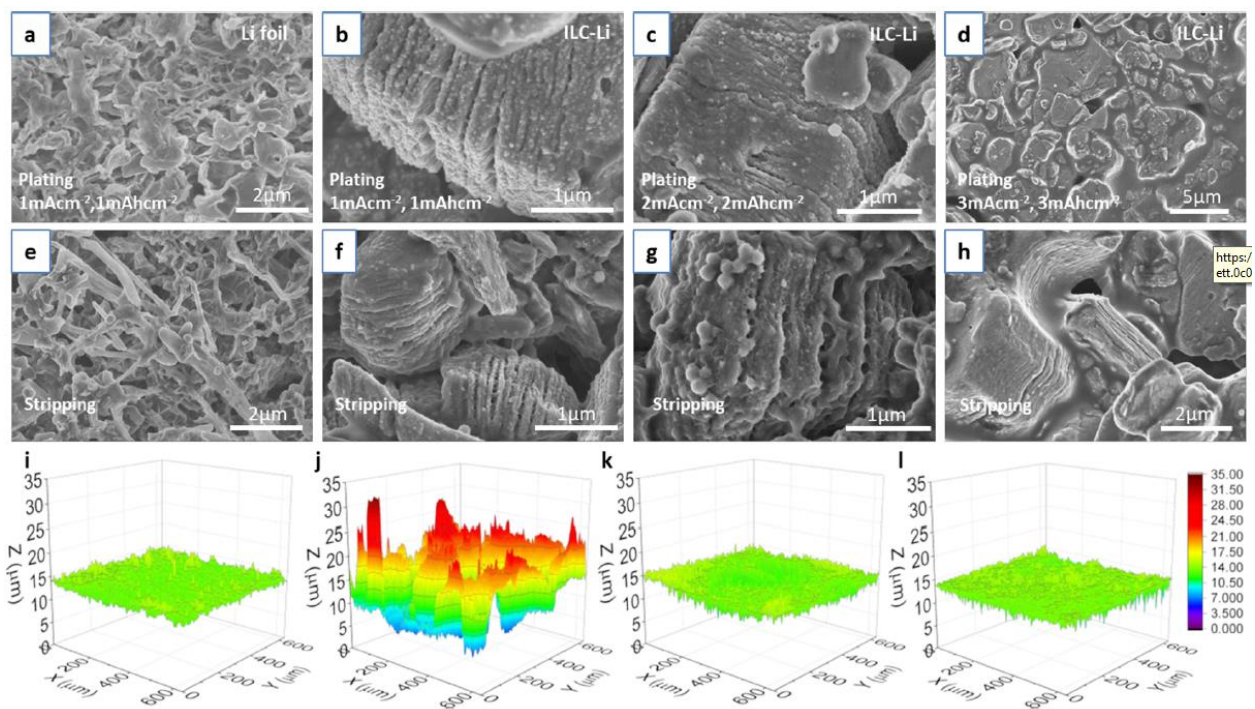


Figure 3. 13 Morphology evolution of ILC-Li and Li foil upon Li plating/stripping and its surface roughness measurements.

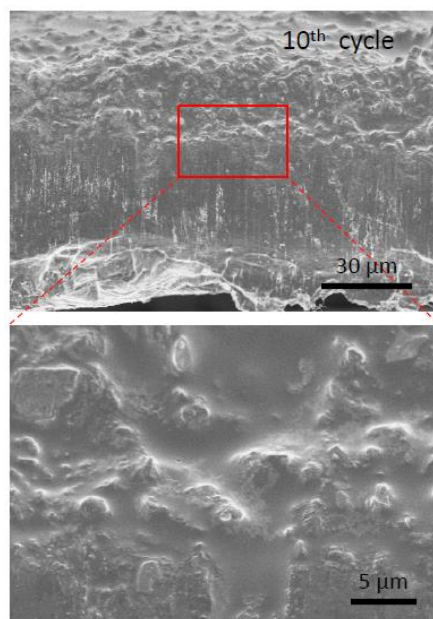


Figure 3. 14 Cross-section image at MXene-Li interface.

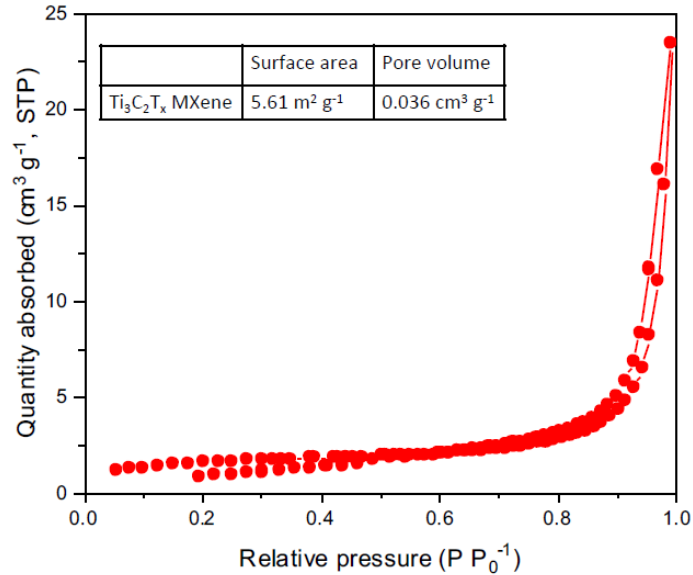


Figure 3. 15 Nitrogen sorption–desorption isotherm of pristine MXene.

A capillary cell (Figure 3.10b) was designed to in-situ observe the mossy/dendritic Li growth for further studying of dendrites suppression mechanism. The clear mossy Li growth appeared 2nd minutes plating in granule Li under current density of 4.77 mA cm⁻², while ILC-Li emerged Li metal color on 20th minutes. The differences in dynamic real time Li growth between granule Li and ILC-Li illustrated excellent conductivity MXene with lamination structure delivered fast Li⁺/e⁻ flux, resulting intercalation and inter-block type Li deposition. Current uniformly distributed in larger surface area of lamination structure, resulting a decreased local current density. Then, fast Li⁺/e⁻ flux resulted consistent Li ion concentration at ILC-Li electrolyte interface, which greatly lessened uneven local Li deposition. Therefore, MXene as a “Li host”, played a great role for space utilization in Li deposition. At 40 minutes to 80 minutes dynamic Li stripping in capillary cell, ILC-Li exhibited an excellent reversibility of cell cycling. The thin layer of Li metal color gradually faded in ILC-Li (Figure 3.10a), while grown mossy Li scarcely reduced in granule Li cell (Figure 3.10c) in stripping cycles. Uneven deposited Li was

isolated because of hostless natural and wrapped SEI, and further induced irreversible mossy type Li stripping.

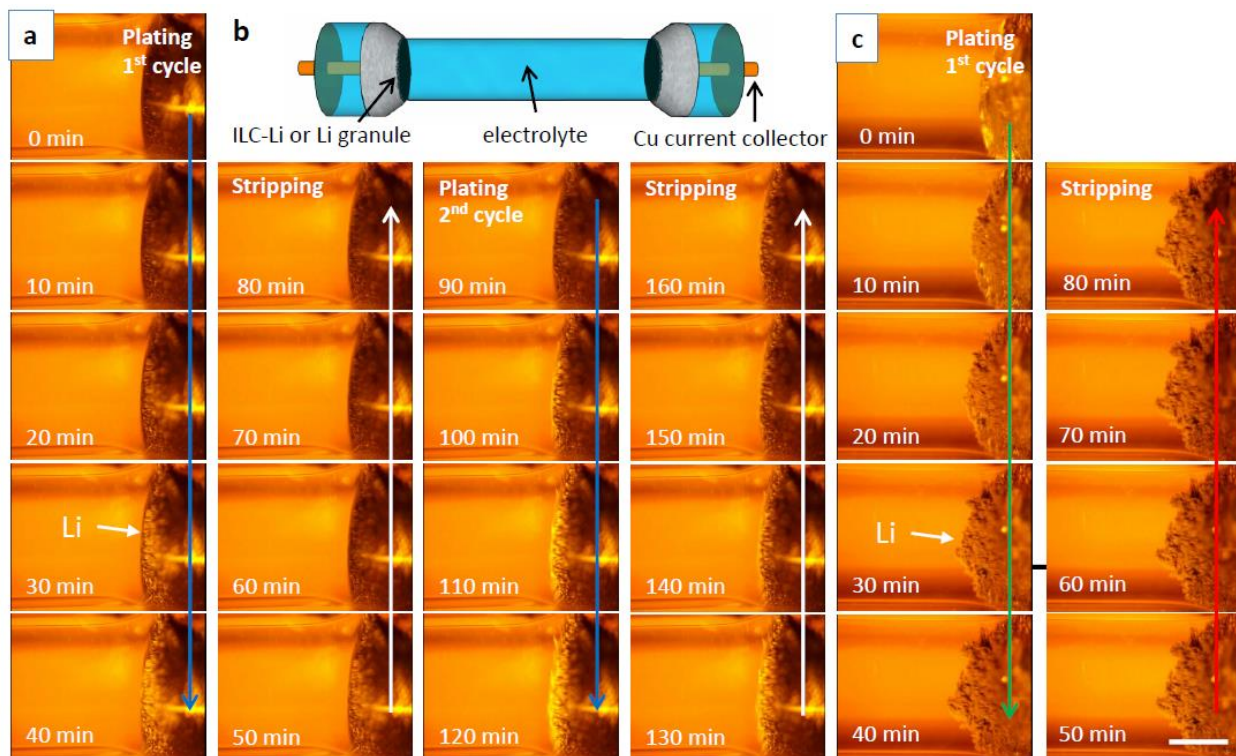


Figure 3. 16 In-situ capillary cell observation of Li dendrites growth/depletion upon Li plating/stripping.

3.2.4 X-ray photoelectron spectroscopy characterization of SEI in ILC-Li and Li foil

To further study the mossy/dendritic Li suppression mechanism in SEI level, a series of X-ray photoelectron spectroscopy (XPS) with depth profiles characterization was applied to reveal the composition of SEI at different depths. The C 1s, F 1s, Ti 2p, Li 1s and O 1s spectra were examined in 3rd cycled ILC-Li (Figure 3.11), while C 1s, F 1s, Li 1s and O 1s spectra were tested in cycled Li foil (Figure 3.12). The peak 286.7 eV and 287.8 eV in C 1s respectively

corresponding to C-O and C=O only displayed at both surface and 20s etching time (depth \approx 8.8nm). 290.6 eV in C 1s and 688.5 eV in F 1s corresponding to $-\text{CF}_3$, while 530.4 eV in O 1s corresponding to C-O/C=O, which showed on surface only. The components of C-O, C=O and $-\text{CF}_3$ can be simply categorized as organic-rich components in SEI. The both cycled ILC-Li and Li foil has organic-rich SEI only exist at top 8.8 nm of surface. On the other hand, the presence of inorganic-rich components such as LiF, $\text{Li}_2\text{CO}_3/\text{LiOH}$ and Li_2O as deep as hundreds nm from surface and coexists simultaneously with lithium metal.

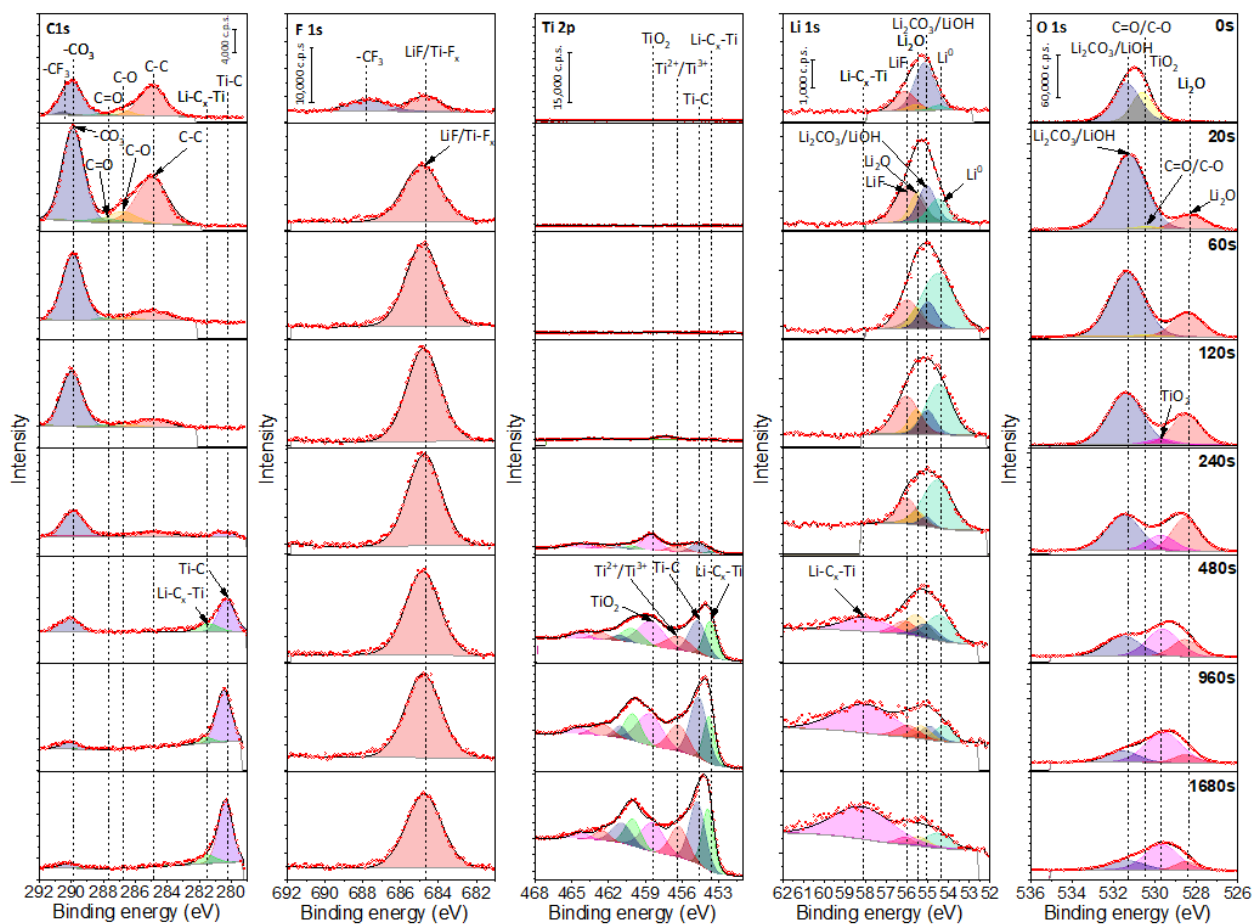


Figure 3. 17 XPS depth profile of ILC-Li electrode from surface to 1680s etching time (which corresponding to depth of 739nm).

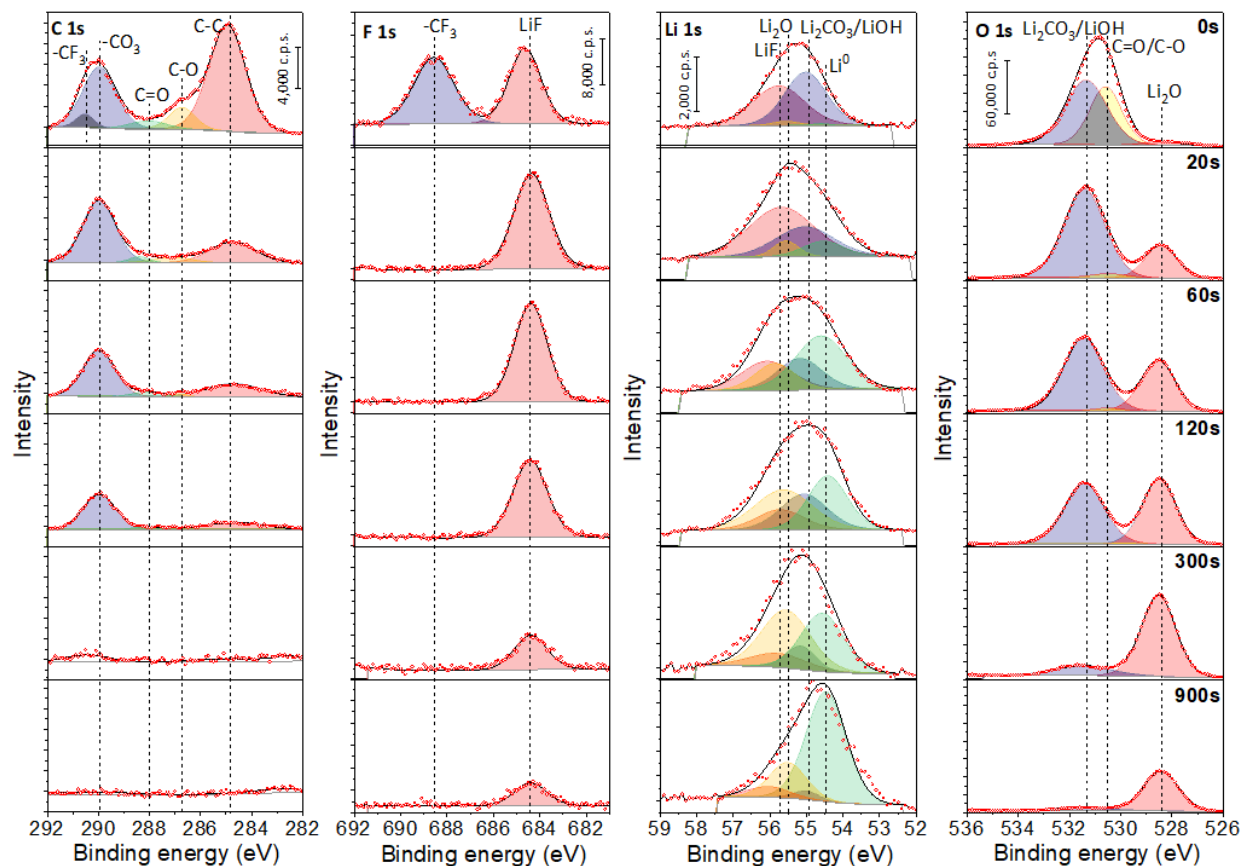


Figure 3. 18 XPS depth profile of Li foil from surface to 900s etching time (which corresponding to depth of 396nm).

Hereby, we defined a method to determine the thickness of inorganic-rich SEI. According to Li spectra evolution in XPS depth profiles, we defined that 50% Li metal mole content as boundary for inorganic-rich SEI and Li metal. Surprisingly, Li metal mole contents exceeded to 50% at 60s etching time which corresponding to ~ 26.4 nm in cycled ILC-Li while Li metal mole contents exceeded to 50% at 300s etching time which corresponding to ~ 132 nm in cycled Li foil (Table 3.1). Except the overlapped F 1s peaks for LiF and $\text{Ti}_3\text{C}_2\text{-F}_x$ at 684.7eV, all peaks intensity evolution in depth corresponding to Li_2CO_3 , LiOH and Li_2O qualitative anastomosis with several peaks in Li 1s, thereby avoiding errors due to peak splitting. The thinner inorganic-

rich SEI than cycled Li foil, it can be used as an evidence for reducing effect current density at local site inside of cycled ILC-Li electrode. As another interesting XPS profiles, Ti 2p peak at 453.6eV and Li 1s peak at 58.2eV was conducted to further probe the chemistry of LiC_x-Ti Li-prefer/lithiophilic layer in cycled ILC-Li electrode. Also, we found the thickness of inorganic-rich SEI is much thicker in Li foil than ILC-Li (Figure 3.13). It is further revealed the previous hypothesis of Li intercalation into the Ti₃C₂T_x nanosheets, which formed a compounds surface layer. This lithiophilic LiC_x-Ti interfacial layer regulated nucleation, resulting uniform Li deposition.

Table 3. 1 Li metal atomic ratio and mole ratio in Li foil and ILC-Li at different depth.

Etching time and depth	Li foil electrode		ILC-Li electrode	
	Li metal atomic ratio (%)	Li metal mole ratio (%)	Li metal atomic ratio (%)	Li metal mole ratio (%)
0s	1.73	2.35	7.91	11.80
20s (8.8nm)	13.38	16.59	17.86	22.99
60s (26.4nm)	39.63	48.92	44.50	50.52
120s (52.8nm)	30.19	41.96	54.74	62.40
240s (105.6nm)	N/A	N/A	62.18	67.38
300s (132nm)	36.38	50.18	N/A	N/A
900s (396nm)	69.13	78.53	N/A	N/A

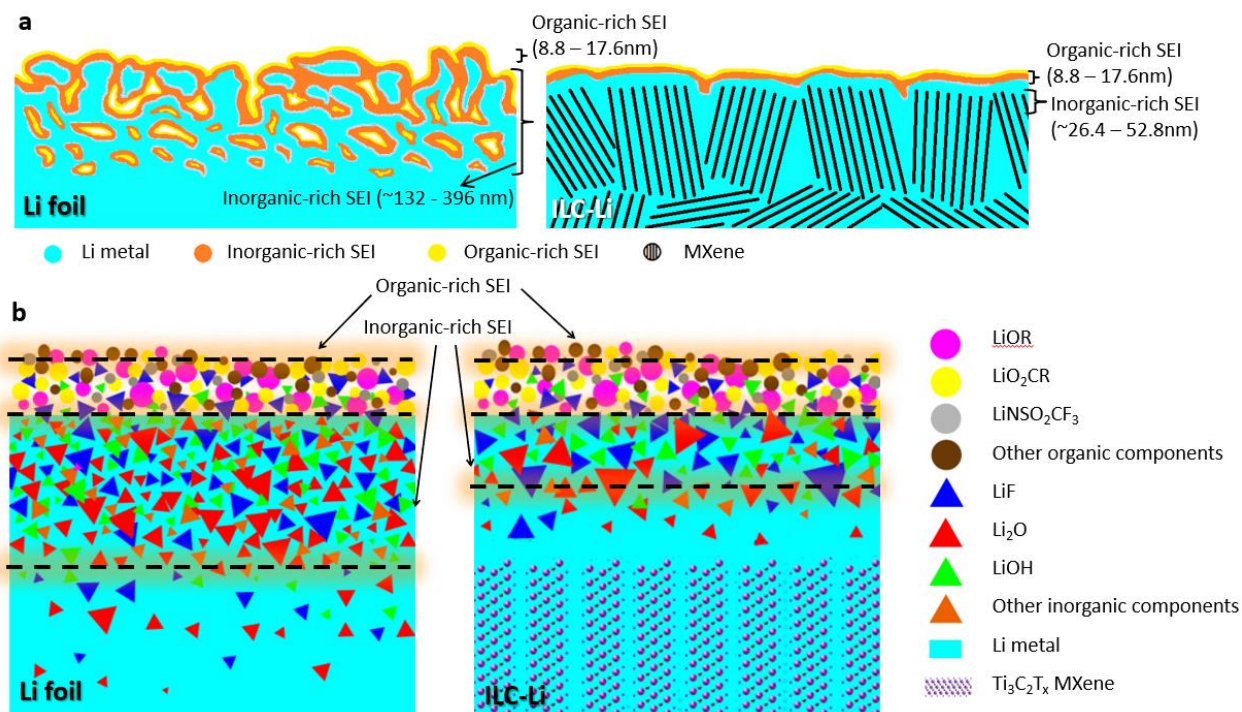


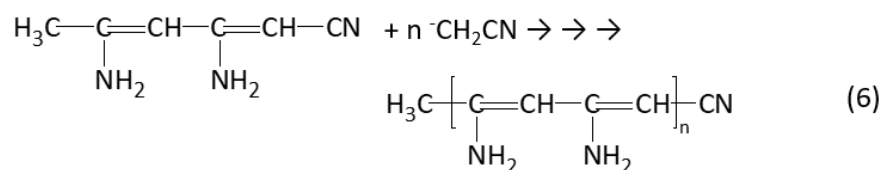
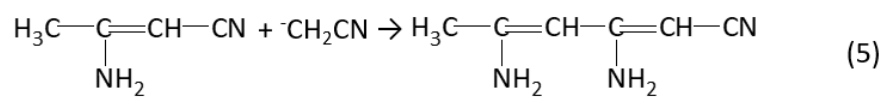
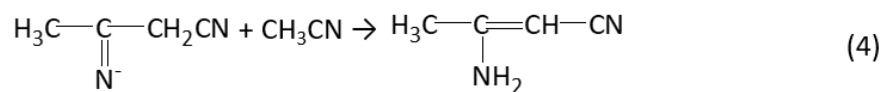
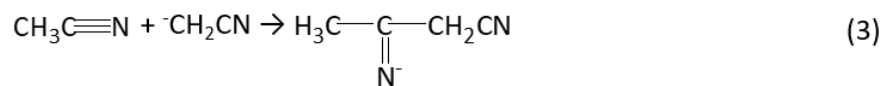
Figure 3. 19 Schematic of organic-rich SEI inorganic-rich SEI distribution in Li foil and ILC-Li.

3.3 Characterization of reinforced artificial pre SEI-Li

3.3.1 Reaction of ACN and Li metal

The reaction between ACN and Li metal was firstly reported by Rupich et al.⁹⁹ The reaction products including methane, lithium cyanide (LiCN) and a series of organic products. Firstly, Li metal will react with ACN to form CH_3^- and CN^- . Then CN^- and Li^+ can pair to form lithium cyanide while CH_3^- react with ACN to form CH_2CN^- . There are possible polymerization resulting in by reacting CH_2CN^- anion and ACN. All possible reaction chemical formulas were listed in Eq. (1) – (6). The Li metal and ACN reaction experiment were conducted via dropping 60 μl into well-polished Li foil. The reaction processes are accompanied with generation of a large number of bubbles, which corresponding to the reaction products of methane. The

experimental results of fourier-transform infrared spectroscopy (FTIR) revealed the existence of C-N (1143-1281 cm^{-1}) stretches and N-H ($\sim 1600 \text{ cm}^{-1}$) stretches $\text{C}\equiv\text{N}$ ($\sim 2174 \text{ cm}^{-1}$) in ACN reacted Li foil (Figure 4.3). It indicates a lot of organic reaction products containing amine and nitrile, which fit the chemical formulas listed.



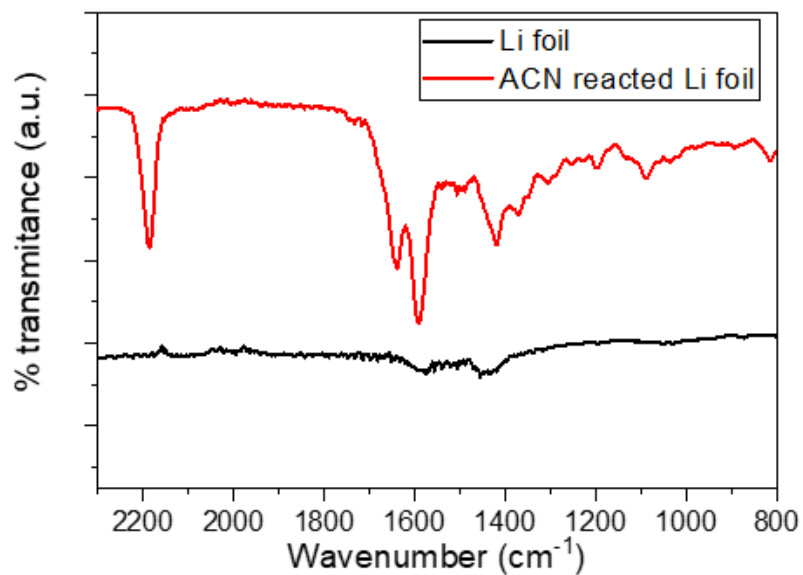


Figure 3. 20 Fourier-transform infrared spectroscopy of ACN reacted Li metal and Li foil.

The morphology characterization of ACN reacted Li (Figure 4.4) by SEM showed porous structure, which corresponding to methane generated bubbles during violent reaction process. The ductile framework of organic components constructed the ACN passivated Li metal.

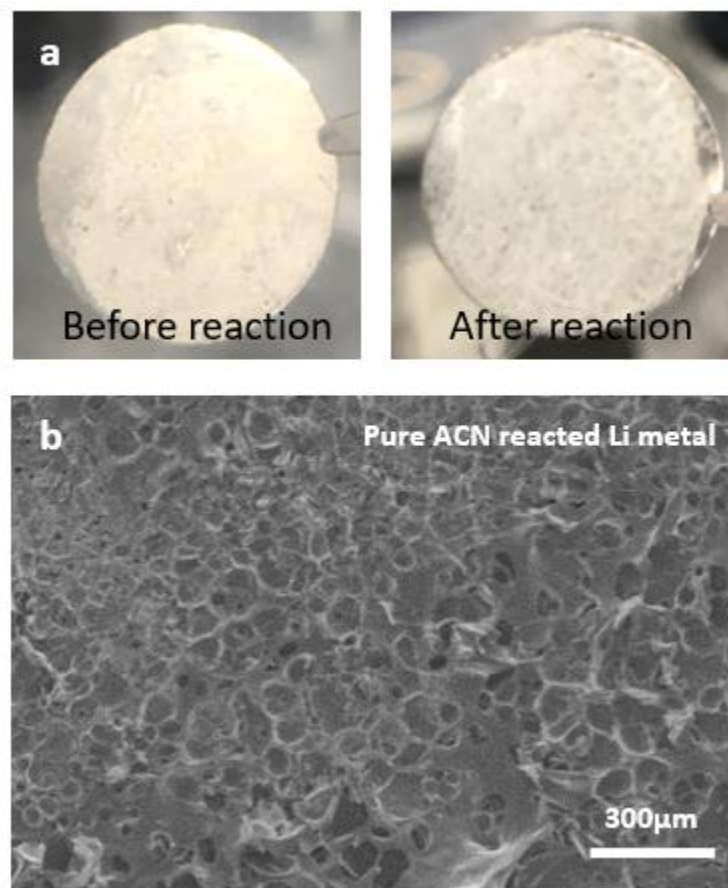


Figure 3. 21 (a) Digital image comparison of before and after ACN Li-metal reaction. (b) SEM image of pristine ACN reacted Li metal.

3.3.2 Composition characterization of reinforced artificial pre SEI

The reinforced artificial SEI-Li also was characterized scanning electron microscope (SEM) (Fig 4.5), transmission electron microscope (TEM) (Fig 4.6) affiliated with Energy Dispersive X-ray (EDX) and electron energy loss spectroscopy (Fig 4.6d-g). The top view of 5% 1M LiTFSI in ACN and 95% HFE reacted Li, 10% 1M LiTFSI in ACN and 90% HFE reacted Li and 20% 1M LiTFSI in ACN and 80% HFE were taken via SEM, respectively (Figure 4.5). The smooth surface in 5% 1M LiTFSI in ACN and 95% HFE reacted Li, 10% 1M LiTFSI in ACN

and 90% HFE reacted Li indicates that diluted nitrile-fluorinated solution great reduced the ACN-Li reaction rate. A smooth surface and uniform distributed artificial SEI were successfully covered on Li metal surface.

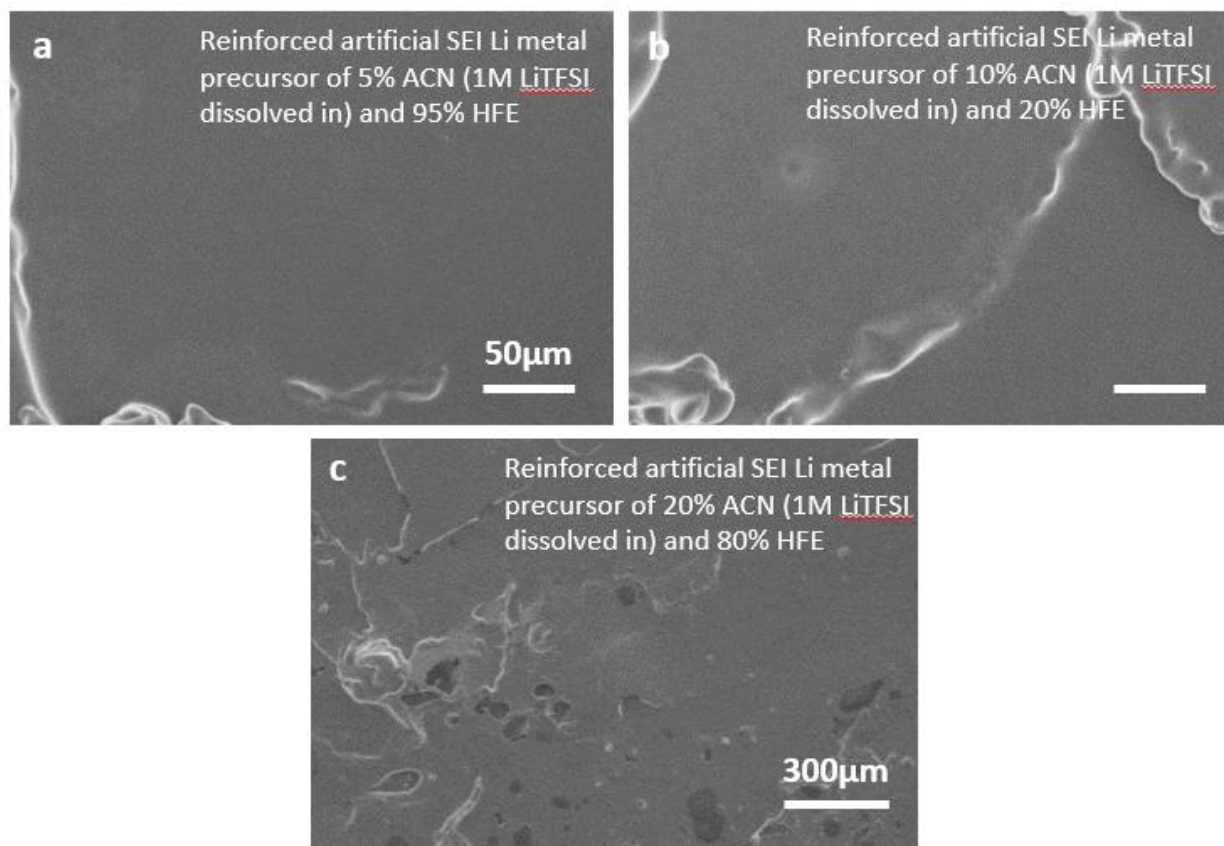


Figure 3.22 SEM image of pristine reinforced artificial SEI Li metal by using precursor of 5% ACN (1M LiTFSI dissolved in) and 95% HFE (a), precursor of 10% ACN (1M LiTFSI dissolved in) and 90% HFE (b) and precursor of 20% ACN (1M LiTFSI dissolved in) and 80% HFE (c).

To further reveal the components and morphology of reinforced artificial SEI, S/TEM was applied to investigate the surface of reinforced artificial SEI-Li. The STEM images (Figure 4.6a) showed the dimension of reinforced artificial SEI is over 100nm thick which indicates much thicker organic components than conventional SEI. Therefore it delivered the higher

mechanical properties than conventional SEI to suppress the dendritic Li growth. Apparent contrast variation among reinforced artificial SEI was observed in STEM image, which corresponding to embedded inorganic nanoparticles. To further confirm that, characterization was carried out via high-resolution (HR)-TEM. In Figure 4.6c, HR-TEM images revealed that possible LiF (lattice fringes of 2.36 Å and 2.04 Å corresponding to LiF 111 plane and 200 plane) and LiCN (lattice fringes of 2.85 Å corresponding to LiCN 210 plane) was uniformly embedded into organic components in reinforced artificial SEI respectively. The EDS mapping exhibited the existence of N, F, S elements. The top 20nm integrated EELS spectra for both reinforced artificial SEI and conventional SEI revealed the difference components. In Li K-edge spectra (Figure 4.6d), The reinforced artificial SEI indicated stronger peak in 62 eV energy loss, which corresponding to containing more inorganic lithium compounds signal such as LiF. In C K-edge spectra (Figure 4.6e), the wider range peaks above the 300eV possibly represents the existence of additional C bonding such as C≡N in reinforced artificial SEI. In N K-edge spectra (Figure 4.6f), the N peaks in reinforced artificial SEI revealed that the existence of amine and nitrile in reinforced artificial SEI organic components. In F K-edge spectra (Figure 4.6g), wider peak range in reinforced artificial SEI possibly owing to the fluorinated organic species which may originated from reaction in HFE fluorinated solvent bound to the Li⁺ or Li metal.

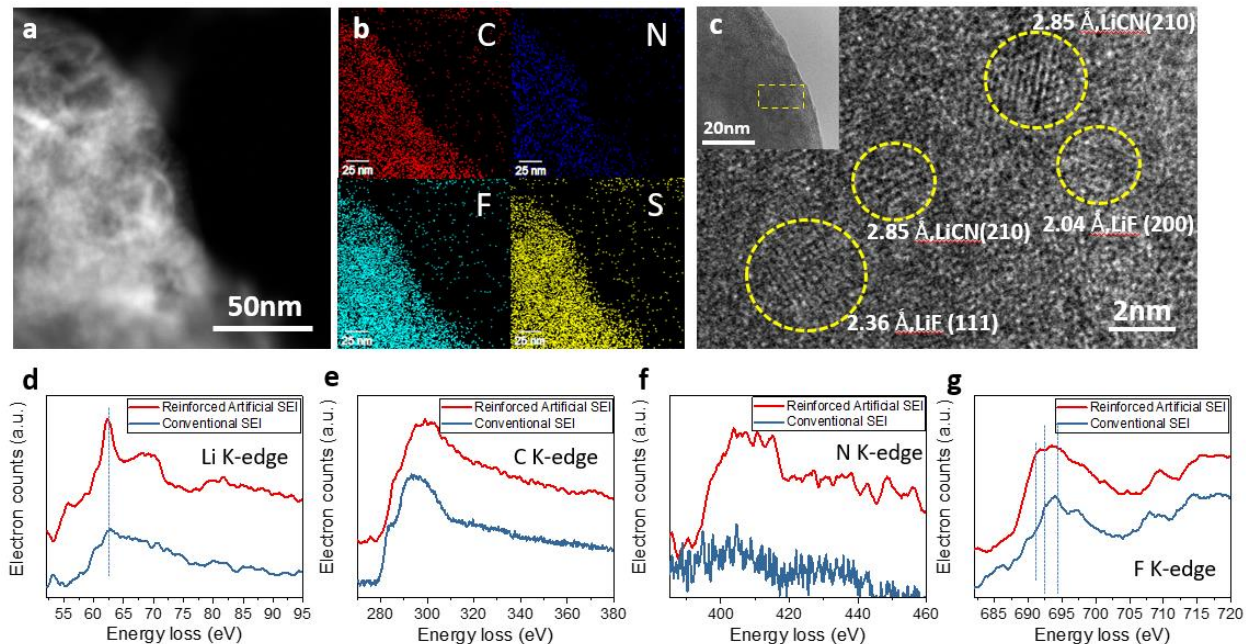


Figure 3. 23 Morphology characterization of reinforced artificial SEI. (a) STEM ADF image of reinforced artificial SEI (b) EDS elemental mapping of reinforced artificial SEI. (c) HR-TEM images of reinforced artificial SEI including low-mag TEM images and high-mag TEM images with lattices of LiF and LiCN. (d-f) Li, C and N K-edge EELS spectra of reinforced artificial SEI.

3.3.3 Morphology evolution of reinforced artificial pre SEI

The one of most important motivation for designing artificial SEI is mossy/dendritic Li suppression (schematic showed in Figure 4.7a and d). Li foil and Morphology evolution of reinforced artificial SEI-Li electrode was carried out by SEM imaging, 3D confocal imaging at various current densities/cycling capacity in symmetric cells. The mossy type structure was found at Li foil sample after 10th cycles under current densities of 1mA cm⁻² and capacity of 1mAh cm⁻² (Figure 4.7b and c). It is very obvious appearance that smooth Li distribution after plating and stripping even under high current density of 5mA cm⁻² and capacity of 5mAh cm⁻², compared with mossy/dendritic growth in bare Li foil (Figure 4.7e-j). The Li metal was well distributed beneath of the SEI film, and no obvious piercing under current density of 1mA cm⁻²

and capacity of 1mAh cm^{-2} . As current density rise to $3\text{-}5\text{ mA cm}^{-2}$ and capacity increased to $3\text{-}5\text{ mAh cm}^{-2}$, Li deposition still showed a majority uniform distribution along the reinforced artificial SEI. Besides, the 3D confocal microscope imaging was applied for surface roughness measurement. According to $600\text{ }\mu\text{m}$ wide square area 3D surface images, pristine Li foil (Figure 4.7k) showed area roughness of 0.50 Sq (Root mean square height) (μm) while pristine reinforced artificial SEI-Li (Figure 4.7m) display 0.56 Sq (μm). After 10^{th} cycles, area roughness of Li foil (Figure 4.7l) electrode rise to 3.43 Sq (μm) while reinforced artificial SEI-Li electrode (Figure 4.7n) exhibit an good area roughness of 1.83 Sq (μm). It showed that reinforced artificial SEI-Li regulated Li ion flux during cycling, resulting in uniform Li deposition/dissolution. It also demonstrated that Li metal has extremely irregular mossy/dendritic Li deposition compared to reinforced artificial SEI-Li.

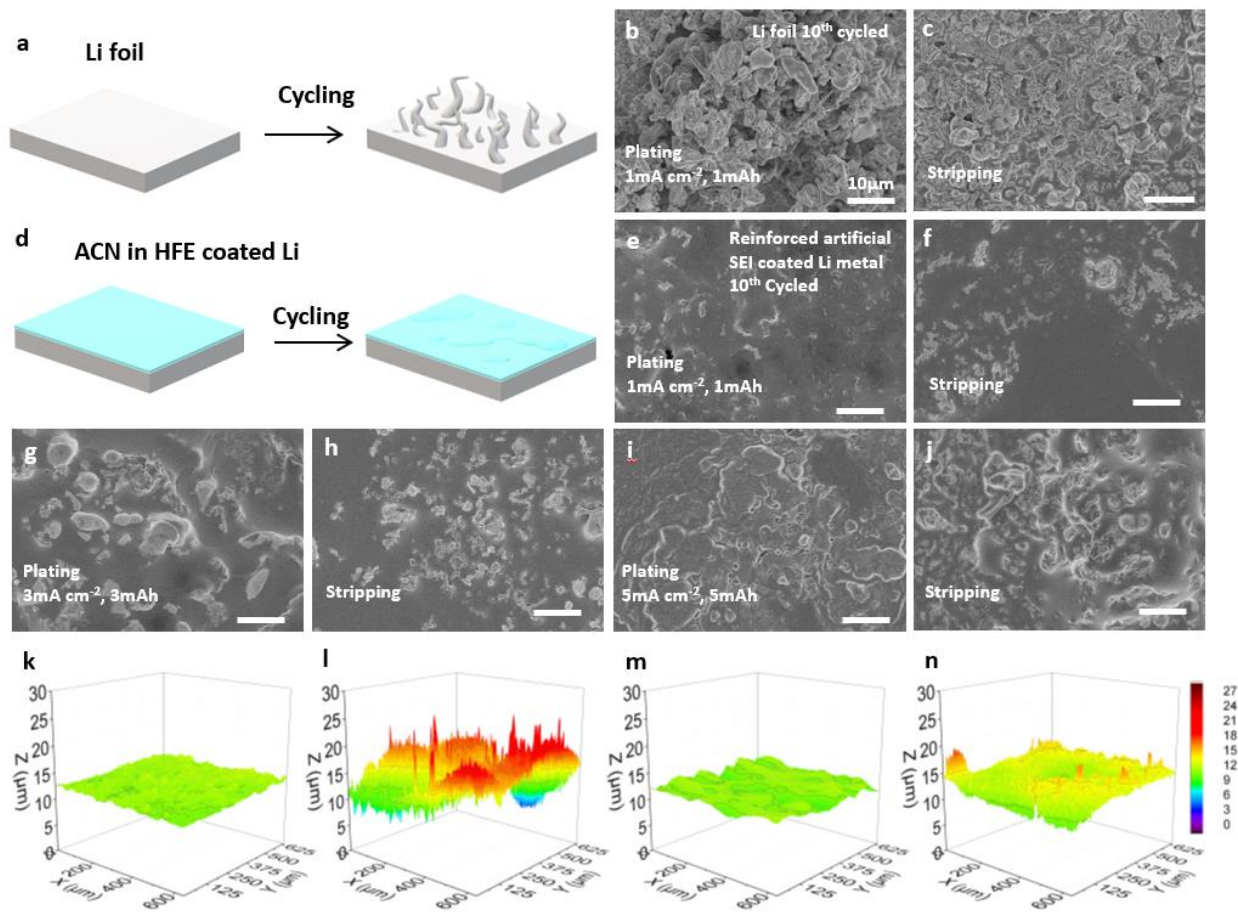


Figure 3. 24 Morphology evolution of the Li foil and reinforced artificial SEI coated Li metal electrodes upon Li plating/stripping at different current densities after 10 cycles.

3.4 Experimental details

3.4.1 Experimental details of LiCFF characterization.

Thermogravimetric analysis (TGA) was performed at air environment from 25 °C to 700 °C with a ramp speed of 5 °C per min by using TA Instruments SDT2960 (RGA mass spectrometer). X-ray diffraction (XRD) measurements were carried out at Bruker D8 Discover X-ray Diffractometer using Ni filtered Cu K α radiation. The applied current and voltage were 40 mA and 40 kV, respectively. The sample was scanned from 15 to 70° with a speed of 5°/min. Scanning electron microscope (SEM) images were captured on a Hitachi S4800 ultra-high resolution field emission scanning electron microscope (FESEM) equipped with energy-dispersive X-ray spectroscopy (EDS). For the *ex-situ* morphology evolution, the LiCFF sample was prepared from an opened coin cell after cycling under various current densities. The sample was completely rinsed with diethyl carbonate (DEC) to remove the electrolyte residuals before the observation. The Raman spectroscopy was carried out using 514 nm laser excitation via HORIBA Raman Microscope XploRA Plus. The mechanical property of dynamic memory analysis (DMA) test was completed on TA Instruments Q800 with a frequency of 1Hz and a temperature ramp speed of 5 °C/min.

The *in-situ* capillary cell observation was operated via a transparent glass capillary cell that contains a symmetric cell inside. The glass capillary cell was formed by welding two glass tubes (Internal diameter x length: 4 × 25 mm and 3 × 7 mm) at a high temperature. Then the symmetric cell was assembled inside in the glove box. In a typical experiment, the electrolyte (LP47, BASF Corp.) was first filled in by capillary force. Two small pieces of LiCFFs or two Li granules (99%, American Elements) as both electrode and sealing agent were carefully placed on

the both ends of the cell with a distance of 5-7 mm. A copper wire with 1 mm in diameter was poked into the LiCFF or Li granule as current collector. Finally the cell setup was connected to the battery tester to perform the Li plating/stripping tests. The dynamic morphology evolution of mossy/dendritic Li was recorded and using a digital trinocular stereo zoom microscope (SM-3TZ-54S-5M, AmScope).

3.4.2 Experimental details of ILC-Li characterizations.

X-ray diffraction (XRD) analysis was operated at Bruker D8 Discover X-ray Diffractometer without filtered Cu K α radiation. The applied current and voltage were 40 mA and 40 kV, respectively. The sample was scanned from 4 to 80° with a speed of 1°/min inside an Argon filled airtight holder. Scanning electron microscope (SEM) imaging was performed at Hitachi S4800 ultra-high resolution field emission scanning electron microscope (FESEM) equipped with energy-dispersive X-ray spectroscopy (EDS). High resolution scanning/transmission electron microscope S/TEM images and EDS element mappings were operated on a JEOL JEM-ARM200CF 200 kV STEM/TEM, which was equipped with a probe aberration corrector. TEM images were performed under 200kV accelerating voltage. High-angle annular dark-field scanning transmission electron microscopy (HAADF-STEM) mode imaging and EDS element mapping was imaged under 200 kV accelerating voltage with an image resolution of less than 0.08 nm and energy resolution of 0.35 eV. Morphology evolution of cycled ILC -Li and Li foil samples were conducted from cycled opened coin cells under various current densities. The samples were carefully rinsed with dimethyl ether (DME) to remove the electrolyte residuals before the characterization. XPS measurements were carried out at Thermo Scientific ESCALAB 250Xi XPS, which is affiliated with a scanning ion gun and an electron flood gun. A non-monochromatic X-ray source of Al K α line (a photon energy of 1486.6 eV)

irradiated to sample. The spectra were collected using an ultrahigh vacuum (UHV) instrument with pressure below 1×10^{-10} Pa. The emitted electrons were detected using a hemispherical analyzer under an angle of 45° to the surface normal. All XPS spectra were fitted with Gaussian–Lorentzian functions and a Shirley-type background and plotted as a function of the binding energy with respect to the Fermi level. All the data were calibrated using the C 1s peak at 284.8 eV. 3D surface imaging was performed by Olympus LEXT OLS4100 3D Laser Confocal Microscopy equipped with a 405nm semiconductor laser photomultiplier detector.

The dynamic morphology evolution of mossy/dendritic Li deposition/dissolution was recorded via a digital trinocular stereo zoom microscope (SM-3TZ-54S-5M, AmScope). A sealed transparent hourglass type tube with symmetric cell inside was used for In-situ capillary cell observation. The cell has internal diameter of thinner observation section of 3mm and thicker section on both sides of 4mm. Firstly, the electrolyte (1.0 M LiPF_6 dissolved in 3:7 weight ratio of ethylene carbonate (EC) and ethyl methyl carbonate (EMC) with 2wt% vinylene carbonate (VC) as electrolyte additive) was first filled in cell by capillary force. Then, ILC -Li and granule Li were used to seal the capillary cell in sides. 1 mm diameter copper wire was poked into the ILC -Li or granule Li as current collector. The assembled capillary cells were connected to battery tester system (LANDT 2001CT, Landt Instruments, Inc.) to perform the Li plating/stripping test.

4.4.3 Experimental details of reinforced artificial pre SEI characterization

Scanning electron microscope (SEM) characterization was conducted at Hitachi S4800 ultra-high resolution field emission scanning electron microscope (FESEM) equipped with energy-dispersive X-ray spectroscopy (EDS). Morphology evolution of cycled reinforced artificial SEI-Li and Li foil samples were performed from 10th cycled symmetric coin cells under

various current densities. The samples were carefully rinsed with dimethyl ether (DME) to remove the electrolyte residuals before the characterization. High resolution scanning/transmission electron microscope S/TEM images and EDS element mappings were operated on a JEOL JEM-ARM200CF 200 kV STEM/TEM, which was equipped with a probe aberration corrector. TEM images were performed under 200kV accelerating voltage. Annular dark-field scanning transmission electron microscopy (HAADF-STEM) mode imaging and EDS element mapping was imaged under 200 kV accelerating voltage with an image resolution of less than 0.08 nm and energy resolution of 0.35 eV. The electron energy loss spectroscopy (EELS) C K-edge and N K-edge spectra acquisition were performed under 0.25eV/Ch and 5mm aperture in high-loss EELS spectrum from 250eV to 750eV, 0.125eV/Ch and 2.5mm aperture in high-loss from 50eV to 300eV for Li K-edge and 550eV to 800eV for F K-edge. The reinforced artificial SEI-Li and conventional SEI-Li samples were sealed in argon filled container before transferring them into TEM holder. The samples have usually less than 1 minute exposure to air during holder transferring to TEM. XPS measurements were carried out at Thermo Scientific ESCALAB 250Xi XPS, which is affiliated with a scanning ion gun and an electron flood gun. A non-monochromatic X-ray source of Al K α line (a photon energy of 1486.6 eV) irradiated to sample. The spectra were collected using an ultrahigh vacuum (UHV) instrument with pressure below 1×10^{-10} Pa. The emitted electrons were detected using a hemispherical analyzer under an angle of 45° to the surface normal. All XPS spectra were fitted with Gaussian–Lorentzian functions and a Shirley-type background and plotted as a function of the binding energy with respect to the Fermi level. All the data were calibrated using the C 1s peak at 284.8 eV. 3D surface roughness imaging was performed by Olympus LEXT OLS4100 3D Laser Confocal Microscopy equipped with a 405nm semiconductor laser photomultiplier detector. All SEM,

TEM, XPS, 3D Laser Confocal Microscopy measurements were conducted by using 10% 1M LiTFSI in ACN and 90% HFE mixture reinforced artificial SEI-Li. Conventional SEI-Li foil characterization was performed by using over 24 hours assembled symmetric CR2032 coin cell with 60 μ l electrolyte of 1.0 M LiPF₆ dissolved in ethylene carbonate (EC) and DEC (1:1 volume ratio, LP47, BASF Corp.).

3.5 Discussion

To summarize from perspectives of morphology characterization, two modified novel Li metal anode was designed by coating the electrically conductive materials on Li metal surface, which have Li-rich and Li poor sides. And an artificial reinforced SEI was designed via wet chemical sample preparation. By comparing the pros and cons of two electrically conductive buffer layers CFF and MXene, the LiCFF has advantages of using commercially available carbon fiber fabrics, whereas MXene need to have a chemical etching process and limited scalability. However, the MXene has advantages of controllable dimensions, whereas CFF has restricted dimension. Both CFF and MXene provide the space to accommodate the volume expansion during Li plating and stripping. MXene can more effectively utilize the space among MXene stacks and interlayer space. The Li metal deposited at surface of CFF and MXene with 3D architecture, CFF and MXene also provide the excellent conductivity and Li ion transport. Therefore, both strategies provide the homogenous Li plating and stripping. The artificial SEI is a strategy to suppress lithium metal deposition from nucleation stage, and it provide comprehensive enhanced electro-chemo-mechanical stable SEI. From results of morphology evolution, all strategies effectively suppressed the Li dendrites growth and enhanced reversibility of Li plating/stripping.

Chapter 3 is a reprint of the publication “Chen, X., Lv, Y., Shang, M. & Niu, J. Ironing Controllable Lithium into Lithiotropic Carbon Fiber Fabric: A Novel Li-Metal Anode with Improved Cyclability and Dendrite Suppression. *ACS Applied Materials & Interfaces* 11, 21584–21592 (2019)” and “Chen, X., Shang, M. & Niu, J. Inter-layer-calated Thin Li Metal Electrode with Improved Battery Capacity Retention and Dendrite Suppression. *Nano Lett.* **20**, 2639–2646 (2020)”, copyright of American Chemical Society. The dissertation author is the first author and co-writer of this publication. Chapter 3 is also a reprint of the manuscript under preparation “Chen, X., Shang, M. & Niu, J. An electro-chemo-mechanical stable artificial pre SEI design for Li metal anode with enhanced batteries performance.”, The dissertation author is the first author and co-writer of this manuscript.

CHAPTER 4: Electrochemical Performance of Modified Li Metal Anode with Dendrites Suppression and High Reversibility

4.1 Electrochemical performance of LiCFF electrode

4.1.1 Electrochemical stability of LiCFF in symmetric cell.

In order to verify the mechanism mentioned before, electrochemical testing was conducted in both symmetric cells (Fig. 2.11) and Li vs NMC half cells. Fig.2.12a distinguished voltage profiles of symmetric LiCFF cells and bare Li cells over 6000 hours under current density of $1\text{mA}/\text{cm}^2$.

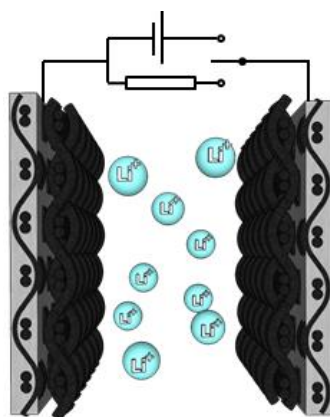


Figure 4. 1 Schematic of symmetric cell.

LiCFF exhibits ultimate low overpotential with $\pm 20\text{mV}$ during electrochemical cycling at first 10 cycles, whereas the bare lithium exhibits over 100mV overpotential. Interestingly, LiCFF exhibits ultimate low overpotential with $\pm 20\text{mV}$ during electrochemical cycling at first

10 cycles performed an extremely stable cycling performance with only 50% increasing in voltage offsets after 500 cycles. In parallel, voltage offsets of bare lithium gradually increased up to 1V after 80 cycles. As increasing the current density to $3\text{mA}/\text{cm}^2$ (Fig. 2.12b) and $5\text{mA}/\text{cm}^2$ (Fig. 2.12c), overpotential cycling performance of LiCFF still maintain a stable level (25mV to 50mV from 1-10th cycle to 490-500th cycle at $3\text{mA}/\text{cm}^2$, 40mV to 120mV from 1-10th cycle to 490-500th cycle at $5\text{mA}/\text{cm}^2$). Overpotential of bare lithium drastically increased to over 3V, due to irreversible lithium plating/stripping process. There is also a sudden drop in bare lithium during cycling, which could be interpreted as dead lithium peeled off from hostless lithium. Besides, enlarged single cycle profile displayed flat voltage plateau in LiCFF and fluctuation voltage plateau in bare lithium. It is mutual proofed with ex-situ SEM characterization, LiCFF exhibits low nucleation energy barriers, low polarization and highly reversible lithium plating/stripping by applied CFF as lithium host under various current density.

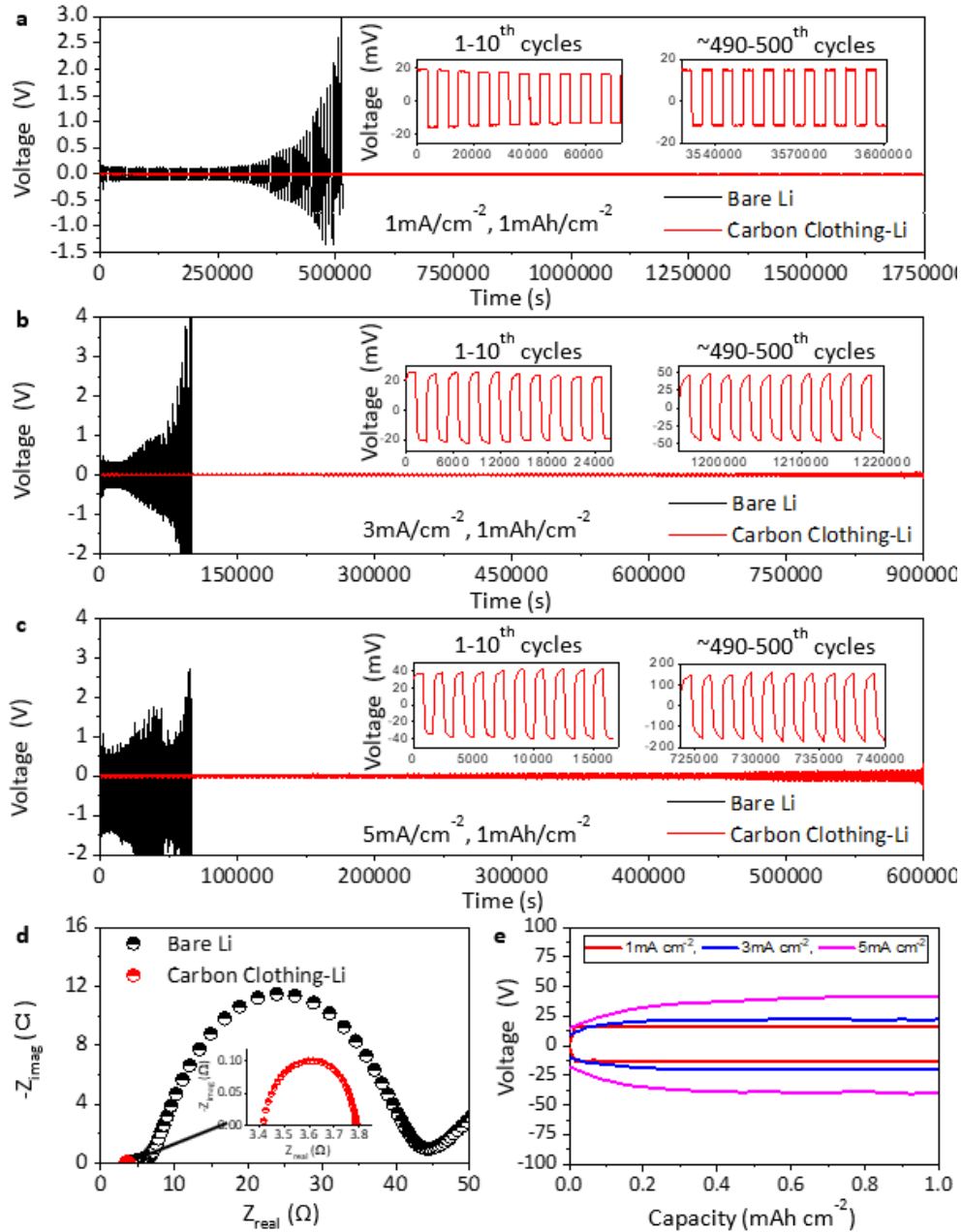


Figure 4. 2 Electrochemical stability of LiCFF electrode.

Moreover, the fully Li infused LiCFF covered by bare Li at top surface and CFF as Li storing host was illustrated as comparison. The relatively uniform Li plating along with CFF host still has unavoidable heterogeneous formation of SEI and mossy/dendritic Li growth. Although

there is a significant improvement over Li foil, the increased overpotentials after hundreds cycles (Fig. 2.13, blue) verified that there are still SEI cracks and dead Li upon further cycling. However, the LiCFF with both Li poor and Li rich sides showed reliable Li plating along with a smooth surface (Fig 2.13). The homogeneous, ultra-thin SEI layer and the enhanced Li^+/e^- conductivity specially from both improved contact area with electrolyte (due to the large inter-spaces) and the intimate contact between SEI and LiCFF remarkably decrease the Li nucleation/growth barrier and polarization, displaying a constant voltage plateau even under a current density of 5 mA/cm^2 during plating/stripping (Fig. 2.14). At high current density $3\text{-}10 \text{ mA/cm}^2$, and high Li plating/stripping capacity $3\text{-}10 \text{ mAh/cm}^2$, the low overpotential of less than 70 mV and less than 175 mV was maintained for over 250 cycles.

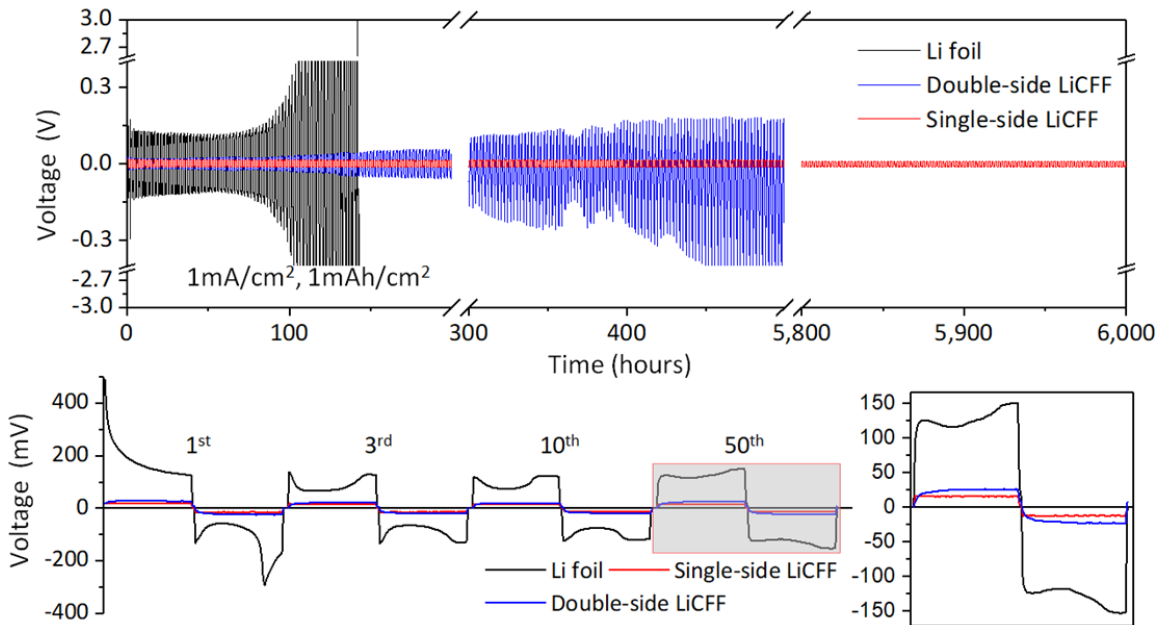


Figure 4. 3 Galvanostatic cycling of single-side (red), double-side (blue) infused LiCFFs and Li foil (black) at 1 mAcm^{-2} in symmetric cells.

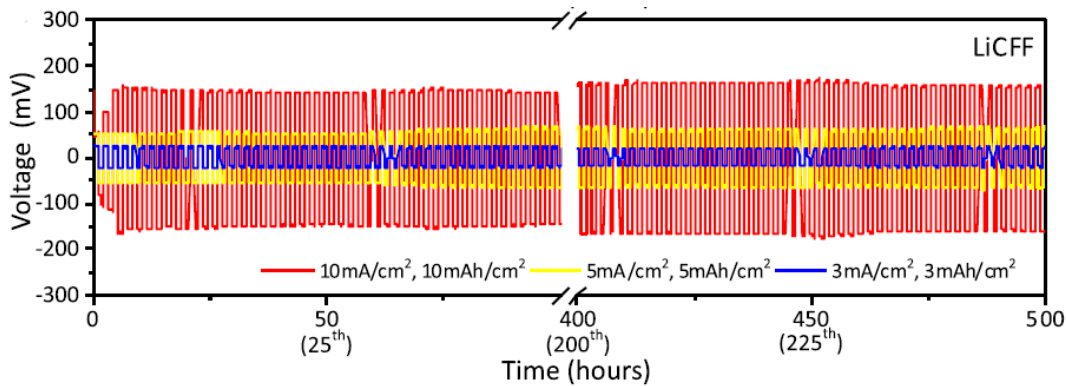


Figure 4. 4 Galvanostatic cycling LiCFFs at up to 10 mAcm^{-2} , 10 mAhcm^{-2} in symmetric cells.

This low energy barrier and low polarization lithium plating/stripping process also reduced the probability of irreversible SEI formation. It is further supported by electrochemical impedance spectroscopy (EIS) test (Fig. 2.12d and Fig. 2.15). The EIS Nyquist plots of bare lithium and LiCFF symmetric cells before cycling and after 10th cycles showed huge difference. The lithium electrode-electrolyte interfacial resistance during lithium plating/stripping can be qualitative analyzed by semicircle in high frequency range. The semicircle of EIS Nyquist plots in bare lithium before cycling is up to 390Ω , this could be explained by a low-conductivity passivation layer induced lithium-electrolyte interfacial resistance. It is further reduced to 40Ω by applying a 10th cycle cell, which removed passivation layer and has a stable SEI involved interface. In parallel, semicircle of LiCFF before cycling only has about 1.3Ω . This is convinced evidence about low interfacial resistance in LiCFF. It has high surface area, high conductivity and lithium friendly interface. After 10th cycles, LiCFF has a tiny semicircle about 0.4Ω . This indicates the more lithium favorable interface formed and ignorable irreversible SEI formation induced interfacial resistance. In summary, LiCFF have significantly reduced interfacial resistance and drastically improved cycling performance.

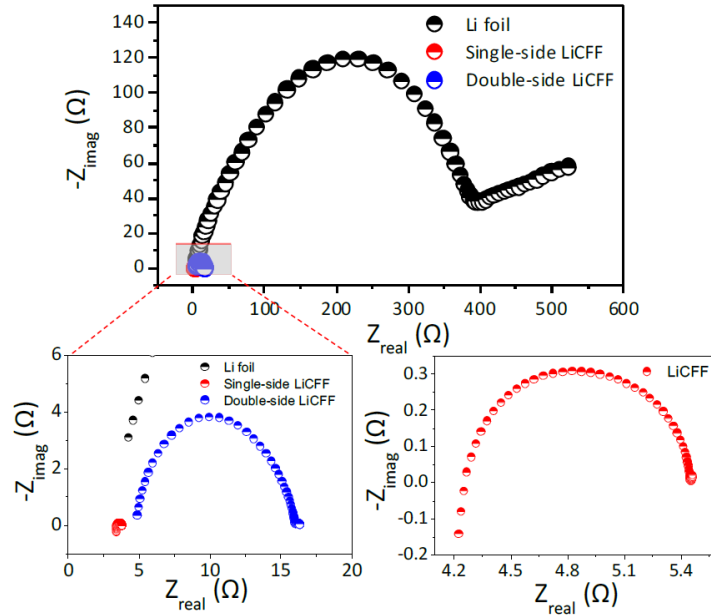


Figure 4. 5 EIS Nyquist plots of LiCFF and Li foil in symmetric cell before cycling.

4.1.2 Full cell performance of LiCFF/NMC 622 and LiCFF-Sulfur batteries

Attractively, one of the most commercialized cathode materials $\text{LiNi}_{0.6}\text{Mn}_{0.2}\text{Co}_{0.2}\text{O}_2$ (NMC 622) were applied to fabric half-cells with LiCFF/Li foil as anode. From Fig. 2.16b-e, LiCFF exhibited the better NMC 622 capacity delivery, rate performance and CE. LiCFF half-cell delivered discharge capacity based on NMC 622 with 175mAh/g at 0.2C, 160mAh/g at 0.5C, 152mAh/g at 1C, 60mAh/g at 10C; whereas Li foil half-cell can only deliver 170mAh/g at 0.2C, 150mAh/g at 0.5C, 142mAh/g at 1C, 20mAh/g at 10C at early cycles. The voltage profiles further confirmed lower plating/stripping energy barrier of LiCFF, which has smooth and flat charge/discharge plateaus. The bare Li exhibit a convex curve at beginning charging process, that corresponding to higher energy barrier need to be overcome. Its high absolute value of slope during discharging process proved unstable discharging plateaus. Besides, higher CE in LiCFF cell supported higher reversibility in half-cell as well. LiCFF only showed slightly higher CE at

0.2C (99.3%-99.9% of carbon clothing-Li, and 99.2%-99.9% of bare Li), which indicates both LiCFF and Li foil have a good reversibility at low current density. Once operating cells under higher current density such as 1C, the CE of LiCFF cell is 1%-1.5% high than Li foil cell. This also demonstrates its good rate performance.

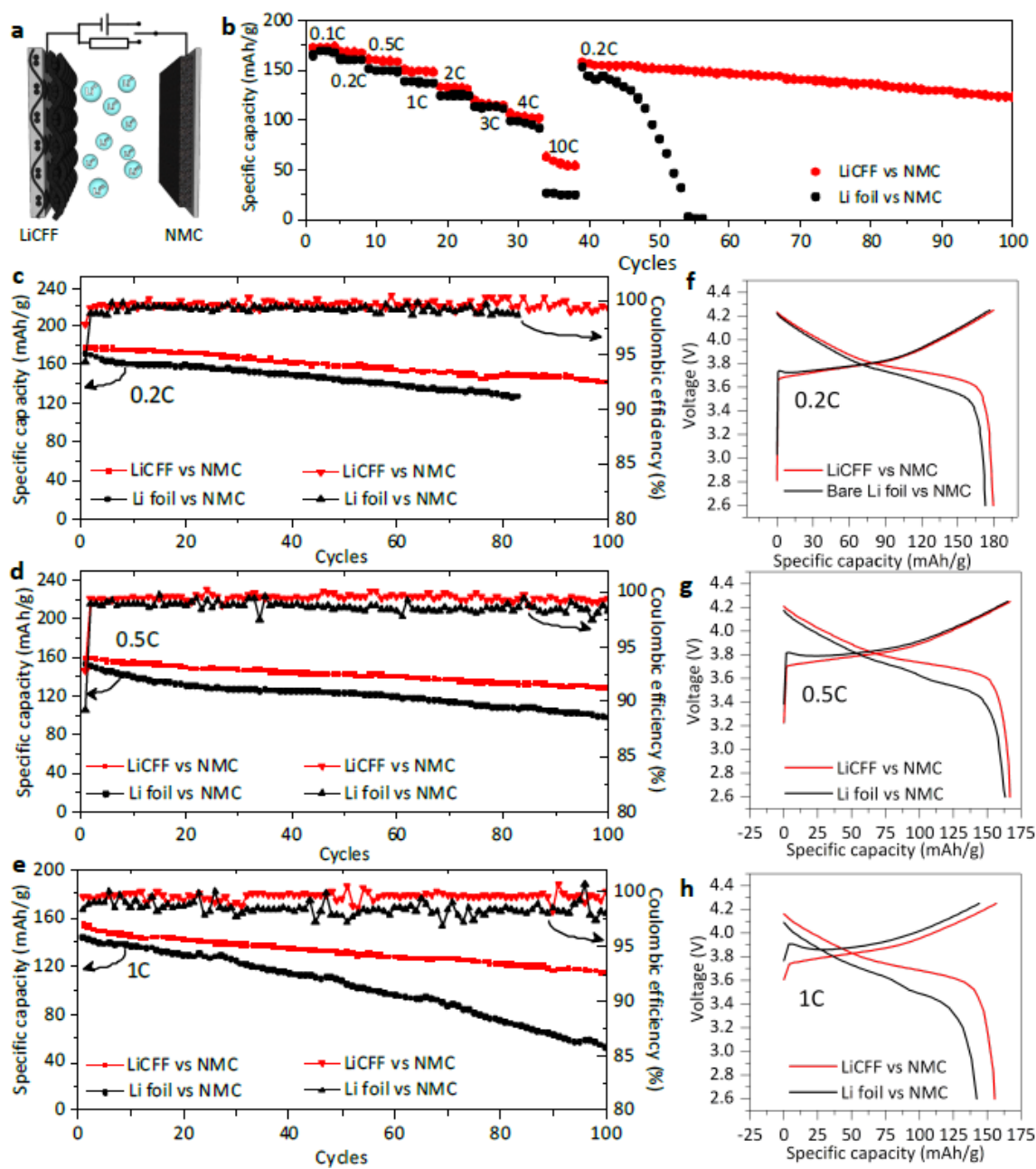


Figure 4. 6 Battery performance of LiCFF/NMC and Li foil/NMC full cells.

The LiCFF/NMC and Li foil/NMC cell interfacial resistance was measured by EIS as well. The LiCFF/NMC cell displays a relatively small contact resistance of 4.6 Ω and a transfer resistance of 11.8 Ω before cycling (Fig 2.17a). The resistances slightly decreased to 4.5 and 8.5 Ω after cycling (Fig 2.17b). Li foil/NMC cell showed high contact resistance of 6.0 Ω and a transfer resistance of 93.2 Ω before cycling (Fig 2.17a). And relatively high values of 4.6 Ω and 17.5 Ω were still remained after 10 cycles (Fig 2.17b). This is further evidence showed LiCFF has great contribution on increasing the Li^+ diffusion efficiency. The positive effects for improving performance are not only limited on symmetric cell, but also apply to Li/NMC cell system.

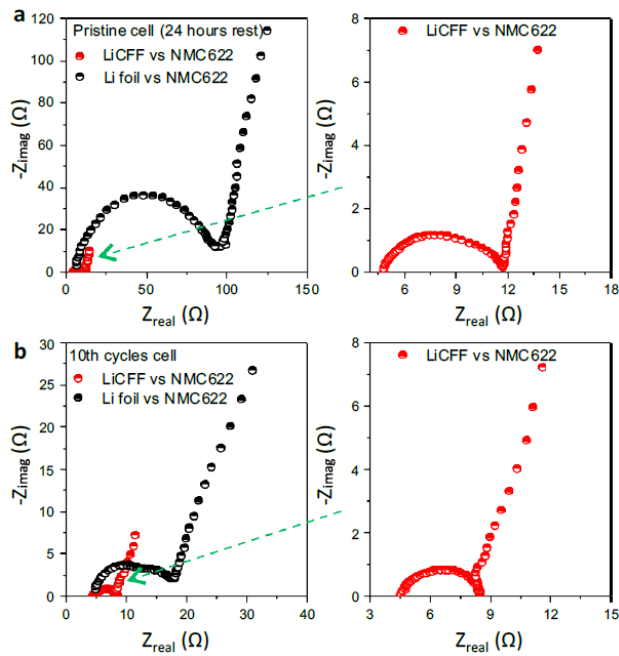


Figure 4. 7 EIS Nyquist plots of pristine and cycled LiCFF/NMC622 and Li foil/NMC622 full cells.

As another application for Li metal anode, Super P-S cathode based Li-S batteries were tested for comparing the LiCFF and Li foil. Specially, a capacity improvement of 44% and

Coulombic efficiency improvement of 19% were observed after 300 cycles at 0.2 C (Fig 2.18a). Same as LiCFF-NMC full cell test, a smoother transition potential and flatter plateau in voltage profile demonstrated a significantly reduced energy barrier for Li plating/stripping (Fig 2.18b). Similar to NMC622, Li-S batteries systems results showed that LiCFF has obvious better performance than Li foil.

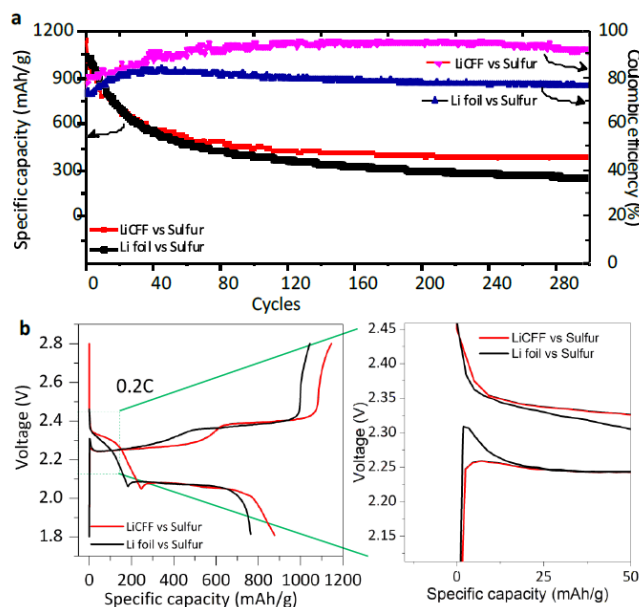


Figure 4. 8 Li-sulfur battery performance by using LiCFF and Li foil.

4.2 Electrochemical characterization and batteries performance of ILC-Li

4.2.1 Electrochemical stability of ILC-Li

Electrochemical stability performance of Li plating and stripping in ILC-Li was investigated via symmetric cells (Figure 3.14a). The overpotential or voltage offset of ILC-Li and Li foil upon cell charging and discharging was tested at various current densities. The ILC-

Li has low overpotential of about ± 35 mV at current densities of $3\text{mA}/\text{cm}^2$ and cycling capacity of $3\text{mAh}/\text{cm}^2$ within initial 10 cycles, then it gradually decreased and stabilized at $\pm 15\text{--}20$ mV after 100 cycles. Similarly, initial overpotential of about ± 120 mV at current densities of $5\text{mA}/\text{cm}^2$ and cycling capacity of $5\text{mAh}/\text{cm}^2$ gradually dropped to ± 80 mV after 100 cycles. Also, initial overpotential of about ± 140 mV at high current densities of $10\text{mA}/\text{cm}^2$ and high cycling capacity of $10\text{mAh}/\text{cm}^2$ was identified to stabilize at ± 120 mV after 100 cycles. However, Li foil performed high overpotential that over ± 350 mV at initial cycles, and significantly increased to over $\pm 1\text{V}$ after 100 cycles. It clearly demonstrated that ILC-Li has excellent reliable reversibility upon Li plating/stripping, while Li foil has obvious reversibility fading. This also indicates that ILC-Li has uniform favorable Li nucleation and controllable Li growth upon MXene nanosheets, while uneven Li nucleation/growth induced increasing barrier for Li plating/stripping. The interfacial resistance comparison of both ILC-Li and Li foil was investigated respectively by using electrochemical impedance spectroscopy (EIS). As shown in Figure 3.14b, EIS Nyquist plots of pristine ILC-Li and Li foil exhibit the low internal resistance of $4.4\ \Omega$ and $5.2\ \Omega$, respectively. However, there are enormous differences in charge transfer resistance, ILC-Li has $11.9\ \Omega$ and Li foil has $112\ \Omega$ respectively. The huge differences are mainly resulted from highly reactive Li foil formed significant SEI layer at electrode electrolyte interface induced large polarization during high frequency charge transfer measurements, and coated MXene upon Li efficiently minimized SEI formation at electrode electrolyte interface. After 10th cycles charging/discharging, charge transfer resistance of ILC-Li slightly decreased to $7.7\ \Omega$ due to stable SEI layer formation (Figure 3.14c). This low charge transfer resistance remained at $8.2\ \Omega$ after 100th cycles, and stable maintaining SEI largely limited active Li consumption in charging/discharging. In contrast to cycled Li foil, even charge transfer resistance decreased to

9.3 Ω after 10th cycles. The transfer resistance increased again to 14.2 Ω after 100th cycles, which correspond to uneven Li plating/stripping induced SEI thickness and porosity increasing. In summary, the MXene coated Li significantly improved electrochemical stability by stabilizing the electrode-electrolyte interface.

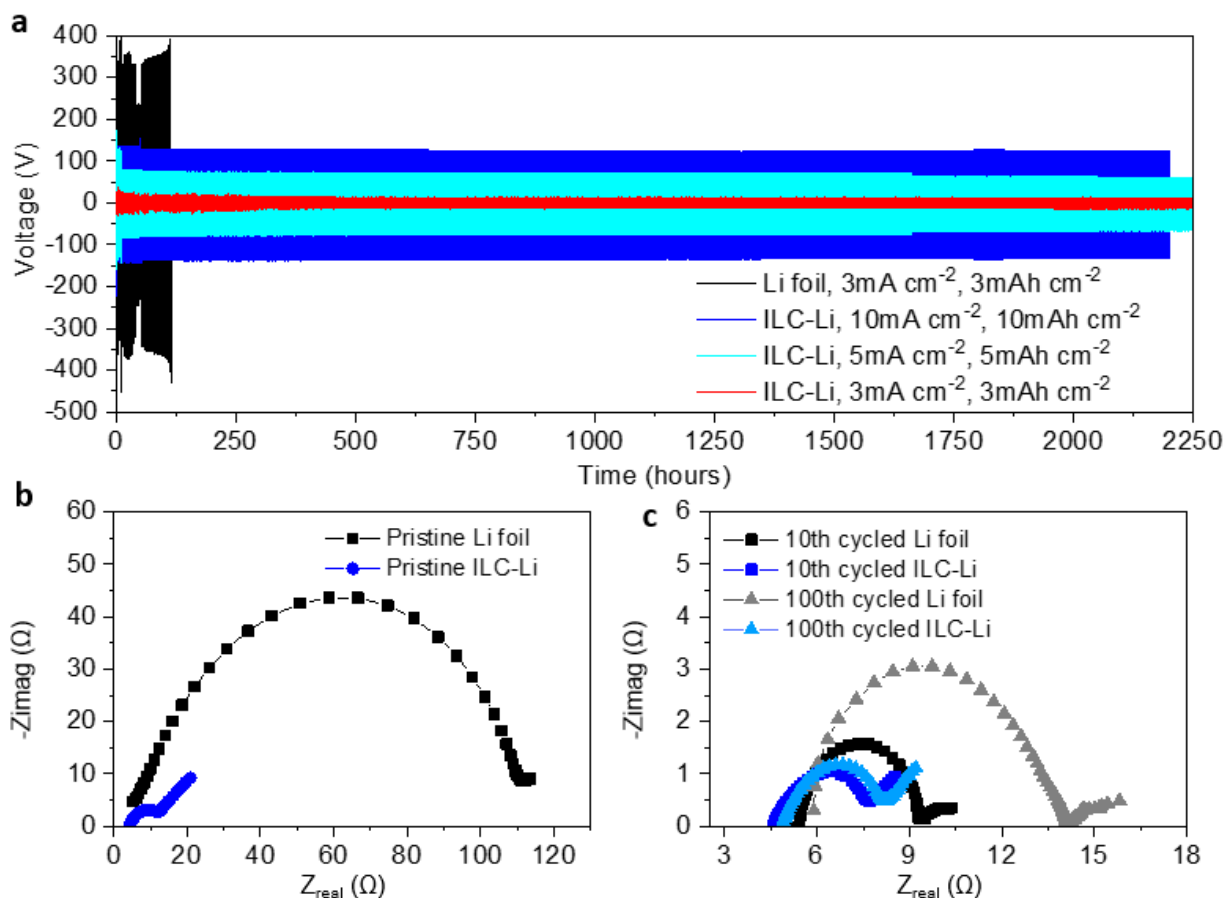


Figure 4. 9 Electrochemical stability of ILC-Li. (a) Galvanostatic cycling of symmetric cells with ILC-Li electrode and Li foil. (b) EIS Nyquist plots in pristine Li foil and ILC-Li. (c) EIS Nyquist plots in 10th cycled and 100th cycled Li foil and ILC-Li.

4.2.2 Full batteries performance of ILC-Li paired with NMC 532

Voltage profiles of different materials including Graphene, multiwall carbon nanotube were compared with MXene (Figure 3.15). It is clearly showed that the 2D MXene exhibited the lowest potential fluctuation at initial Li plating stage, which further showed high electrical conductivity and low energy barrier for Li plating. The full cell of ILC-Li /Li foil anode paired with $\text{LiNi}_{0.5}\text{Mn}_{0.3}\text{Co}_{0.2}\text{O}_2$ (NMC532) as cathode was tested at various charge/discharge conditions. The rate performance in Figure 3.16a exhibited that both ILC-Li and Li foil provided high capacity of 170 mAh g^{-1} at 0.1C, 165 mAh g^{-1} at 0.2C, 157 mAh g^{-1} at 0.5C and 148 mAh g^{-1} at 1C. But as rate up 2C and 5C, the ILC-Li showed higher capacity of 139 mAh g^{-1} at 2C and 45 mAh g^{-1} at 5C while Li foil has 134 mAh g^{-1} at 2C and 26 mAh g^{-1} at 5C, respectively. The NMC capacity retention in Li foil full cell obvious fading faster than ILC-Li after cycling rate back to 0.2C. It indicated that ILC-Li achieved improvement of capacity retention in full cell especially at high rate charge/discharge. To imitate the real battery cycling conditions, the cycling performance in Figure 6b used 0.2 C as charge rate and 0.5 C as discharging rate (Figure 3.16b). The ILC-Li has 92% capacity retention while Li foil only has 72% capacity retention after 100 cycles. Similarly, ILC-Li has initial coulombic efficiency of 90% and stabilized at 99.4-99.7% at following cycles while Li foil has 92% initial coulombic efficiency and significantly fluctuation coulombic efficiency between 96-102%. The Li foil cell failed after 100 cycles while ILC-Li is steadily operating after 200 cycles. The voltage profiles of ILC-Li (Figure 3.16c) with a smooth potential indicated that MXene effectively reduced energy barrier for Li plating at ILC-Li anode. However, voltage profile of Li foil (Figure 3.16d) showed a raised potential which identified larger Li plating/nucleation energy barrier. The appearance of full cell battery differences also was investigated by EIS (Figure 3.16e-f). Both ILC-Li and Li foil full

cell showed internal resistance of $4.9\ \Omega$ before cycling, while ILC-Li has $22.8\ \Omega$ and Li foil has $63.1\ \Omega$ charge transfer resistance respectively. ILC-Li has $21.6\ \Omega$ at 10^{th} cycles to $30.3\ \Omega$ at 100^{th} cycles in transfer resistance while Li foil increased from $19.3\ \Omega$ to $69\ \Omega$ according to 10^{th} cycle to 100^{th} cycles.

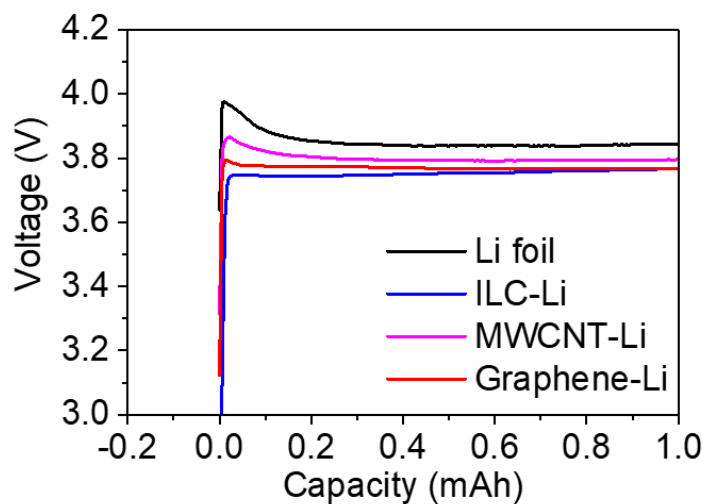


Figure 4. 10 Voltage profile comparison of Li metal with different coatings.

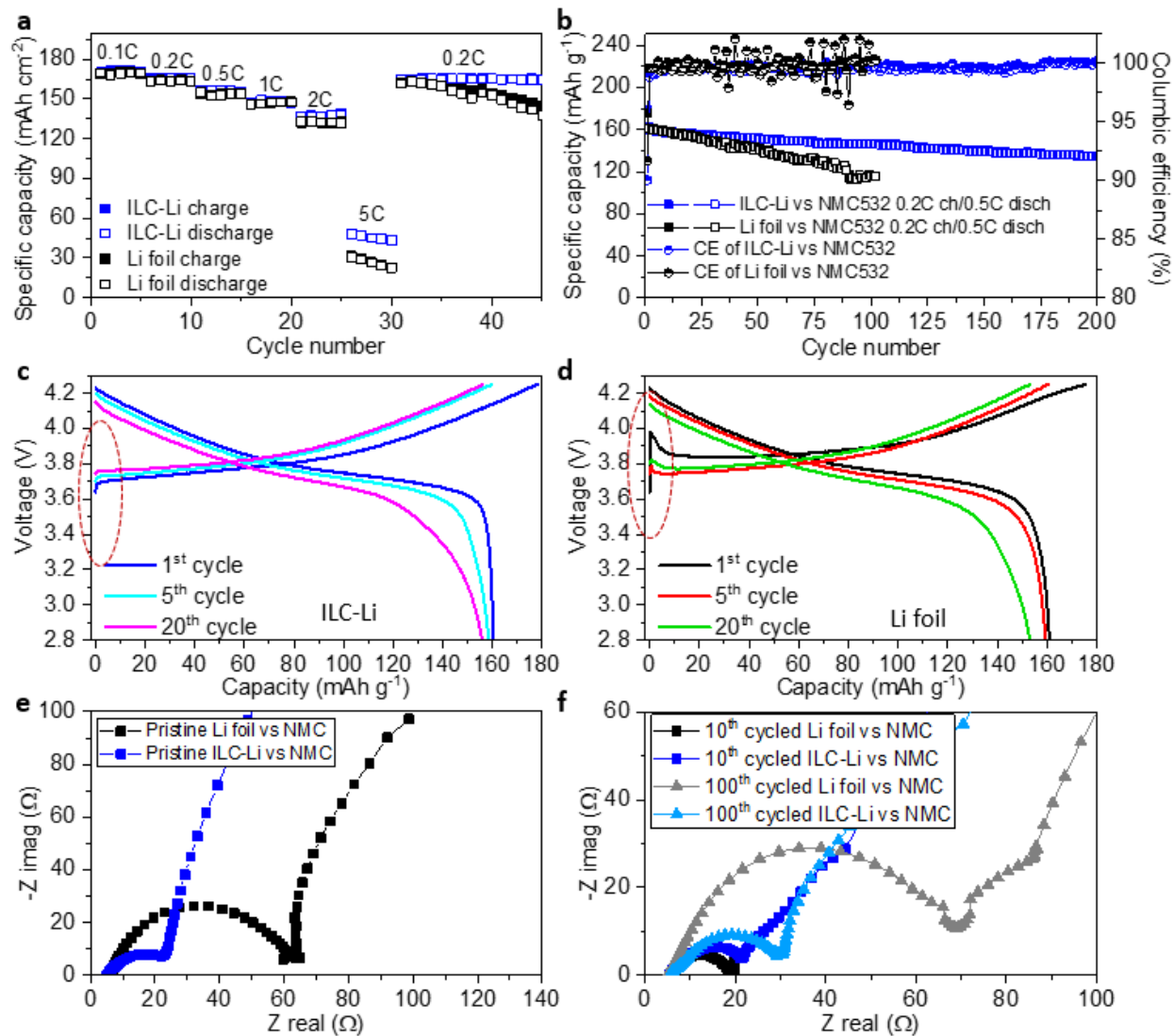


Figure 4. 11 Battery and electrochemical interface performance of ILC-Li/NMC full cells and EIS measurements. NMC622 loading: 10 mg cm⁻².

4.2.3 Full batteries performance of ILC-Li paired with NCA under lean electrolyte condition

For achieving the high energy density over 270 Wh kg⁻¹, both N/P ratio and E/C ratio need to be strictly controlled. The N/P ratio could be controlled within 1.53 by using LiNi_{0.8}Co_{0.15}Al_{0.05}O₂ (NCA) cathode with high areal capacity upon 4 mAh cm⁻² paired with ILC-

Li (30 μm Li foil) anode with areal capacity of 6.18 mAh cm^{-2} . The E/C ratio is able to be restricted within about 6 g (Ah)^{-1} by applying lean electrolyte amount of $5 \mu\text{l mAh}^{-1}$ for cells examination. Herein, the ultrathin ILC-Li | NCA and Li foil | NCA full cells performance at various lean electrolyte condition ($2.5\text{-}10 \mu\text{l mAh}^{-1}$) were collected (Figure 3.17a-d). Lean electrolyte condition of $2.5 \mu\text{l mAh}^{-1}$ has as high as 366.6 Wh kg^{-1} (calculated at Table 3.2), and NCA capacity decay in ILC-Li | NCA cell is obvious slower than Li foil | NCA cell at first 30 cycles. But both cells cannot survive after 30 cycles, it is possibly due to electrolyte components consumption induced electrolyte exhausted at ultralow lean electrolyte condition cycling. As electrolyte increased to $5 \mu\text{l mAh}^{-1}$, ultrathin ILC-Li | NCA has considerable capacity retention of $\sim 75\%$ after 100 cycles based on standard capacity of 185 mAh g^{-1} , while Li foil | NCA cell still had not survived after 30 cycles. At electrolyte increased to $7.5 \mu\text{l mAh}^{-1}$ and $10 \mu\text{l mAh}^{-1}$, ILC-Li | NCA cell exhibit excellent capacity retention of $\sim 87\%$ after 100 cycles, while Li foil | NCA cell has apparent capacity fading after 20 cycles and 45 cycles respectively. Beside lean electrolyte conditions, the large amount of Li involved in plating/stripping due to the practical cell has large areal capacity of 4 mAh cm^{-2} , which also as a result of limiting the performance of Li metal anode. In order to investigate the inactive Li consumption induced Li loss or total capacity loss upon plating/stripping, CE of the MXene coated copper current collector|Li and Cu current collector|Li cell was measured at 0.5 mA/cm^2 and 1 mAh/cm^2 (Figure 3.17e). Li consumption mainly originated from repeated formation of the SEI during mossy/dendritic Li growth and SEI wrapped ‘dead Li’. And Li consumption corresponds to total capacity loss in Cu current collector-ILC|Li and Cu|Li cells. The total Li loss or capacity loss was determined by summing total CE loss at each cycle (Figure 3.17f). CE and the total capacity loss at first cycle of Cu current collector-ILC |Li cell are $\sim 50\%$ and 0.5 mAh cm^2 respectively,

which corresponds to Li consumed by forming $\text{LiC}_x\text{-Ti}$ layers. Except Li consuming of $\text{LiC}_x\text{-Ti}$ forming induced lower CE at first 5 cycles, the Cu current collector-ILC |Li exhibit higher CE than Cu|Li. The total capacity loss in Cu current collector-ILC |Li cell lower than Cu|Li after 20th cycles, and it is 3 times lower after 100th cycles. If the total capacity loss caused by the Li intercalation is excluded in Cu current collector-ILC |Li, the capacity loss is much lower than Cu|Li even at first 5 cycles. It also supported that the cause of Li foil | NCA cell failure at lean electrolyte condition mainly attributed to the excessive consumption of Li and electrolyte components.

Table 4. 1 Energy density estimation based on the ILC-Li | NCA full-cell battery at lean electrolyte conditions.

ILC-Li (30 micron) vs NCA (loading: 20.5mg cm⁻²)		
Cathode areal capacity	4.1 mAh cm ⁻²	4.1 mAh cm ⁻²
Anode areal capacity	6.2 mAh cm ⁻² (~30 micron Li foil)	6.2 mAh cm ⁻² (~30 micron Li foil)
N/P ratio	1.5	1.5
E/C ratio	3.0g (Ah) ⁻¹	6.0g (Ah) ⁻¹
Discharge capacity	~185.0 mAh g ⁻¹	~185.0 mAh g ⁻¹
Average discharge voltage	3.85V	3.85V
<hr/>		
Cathode (D:1.58 cm)	41.0 mg + 2.2 mg (C and Binder)	41.0 mg + 2.2 mg (C and Binder)
Al foil (T: 25µm)	6.6 mg	6.6 mg
Electrolyte	20.0 µl , 24.0 mg, 2.5 µl mAh ⁻¹	40.0 µl, 48.0 mg, 5.0 µl mAh ⁻¹
Separator	3.4mg	3.4mg
Anode (D: 1.56 cm)	4.7mg (1.6mg MXene + 3.1mg Li)	4.7mg (1.6 mg MXene + 3.1mg Li)
Estimated package foil and tabs (~3 wt%)	2.5mg	3.2 mg
Total weight	84.4 mg	109.1 mg
Energy density	366.6 Wh kg ⁻¹	283.6 Wh kg ⁻¹

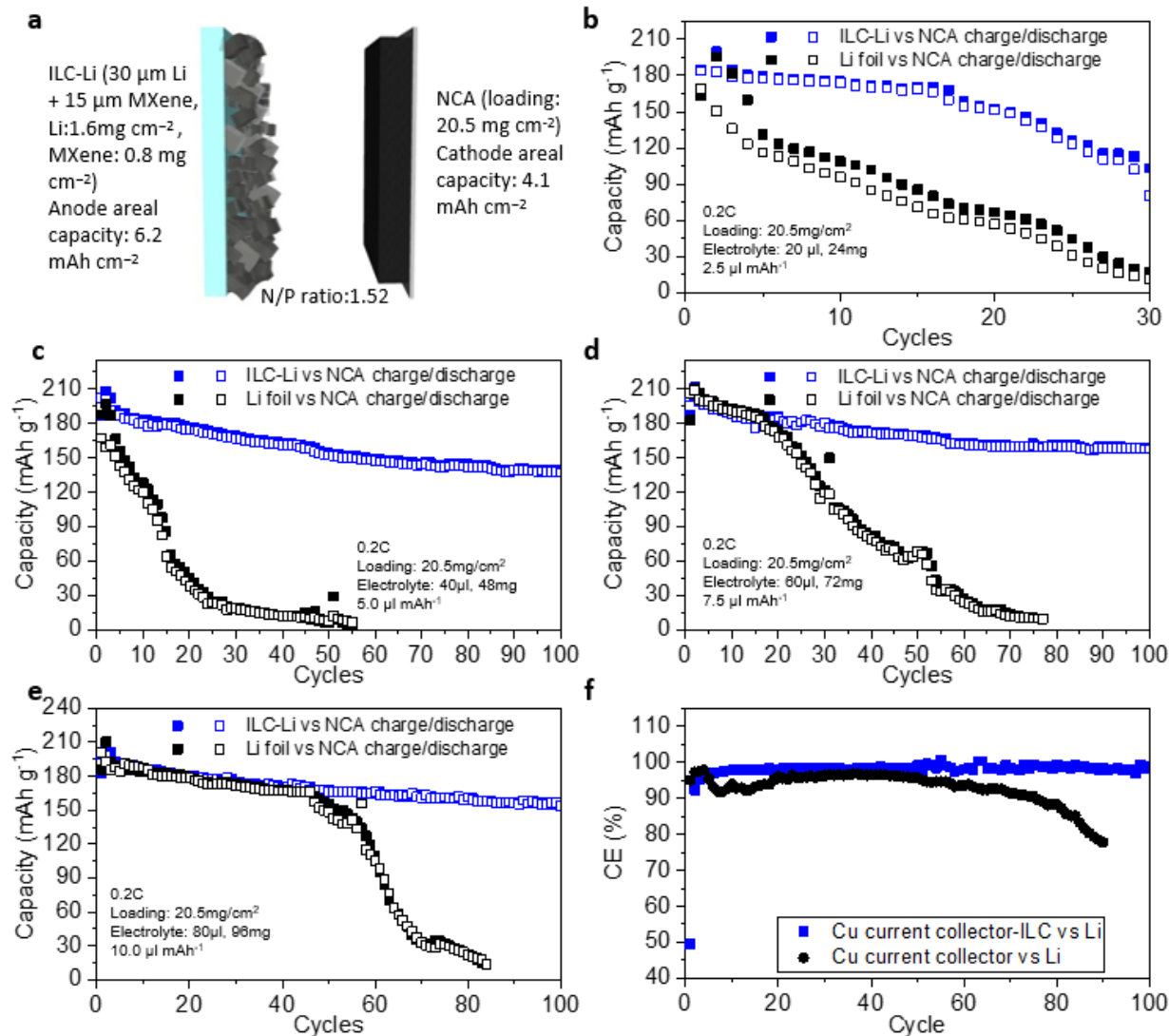


Figure 4. 12 Battery performance at lean electrolyte condition of ILC-Li/NCA full cells and anode free deposition of Li in ILC-Cu/Cu current collector at $0.5\text{mA}/\text{cm}^2$ and $1\text{mAh}/\text{cm}^2$.

4.3 Electrochemical performance of reinforced artificial pre SEI-Li metal anode

4.3.1 Electrochemical stability

Electrochemical stability performance of Li plating and stripping in reinforced artificial SEI-Li was investigated via symmetric cells (Figure 4.8a-d). The overpotential or voltage offset

of reinforced artificial SEI-Li and Li foil upon cell charging and discharging was tested at current densities of $3\text{mA}/\text{cm}^2$ and cycling capacity of $3\text{mAh}/\text{cm}^2$. The reinforced artificial SEI-Li (10% 1M LiTFSI in ACN and 90% HFE precursor) has low overpotential of about $\pm 150\text{ mV}$ at current densities of $3\text{mA}/\text{cm}^2$ and cycling capacity of $3\text{mAh}/\text{cm}^2$ within initial 10 cycles, then it gradually decreased and stabled at about $\pm 75\text{ mV}$ after 150 cycles. Similarly, reinforced artificial SEI-Li (20% 1M LiTFSI in ACN and 90% HFE precursor) has initial overpotential of about $\pm 300\text{ mV}$ and gradually dropped to $\pm 150\text{mV}$ after 150 cycles. Li foil has initial overpotential of about $\pm 80\text{-}100\text{ mV}$, which is lower than reinforced artificial SEI-Li. It indicates the conventional SEI Li foil has lower Li ion transport energy barrier than reinforced artificial SEI-Li, this is possible due to thicker dimension of reinforced artificial SEI. However, Li foil's overpotential gradually increased to $\pm 400\text{-}600\text{ mV}$ after 150 cycles and rise quickly to $\pm 1\text{V}$ after 200 cycles until batteries cannot cycle anymore. Reinforced artificial SEI-Li (both 10% and 20% 1M LiTFSI in ACN and 90% HFE precursor) can stable cycle to 1000 cycles. It clearly demonstrated that reinforced artificial SEI-Li has excellent reliable cycling performance, while Li foil has obvious cycling performance fading. This also indicates that excellent mechanical performance of reinforced artificial SEI successfully suppressed mossy/dendritic Li growth.

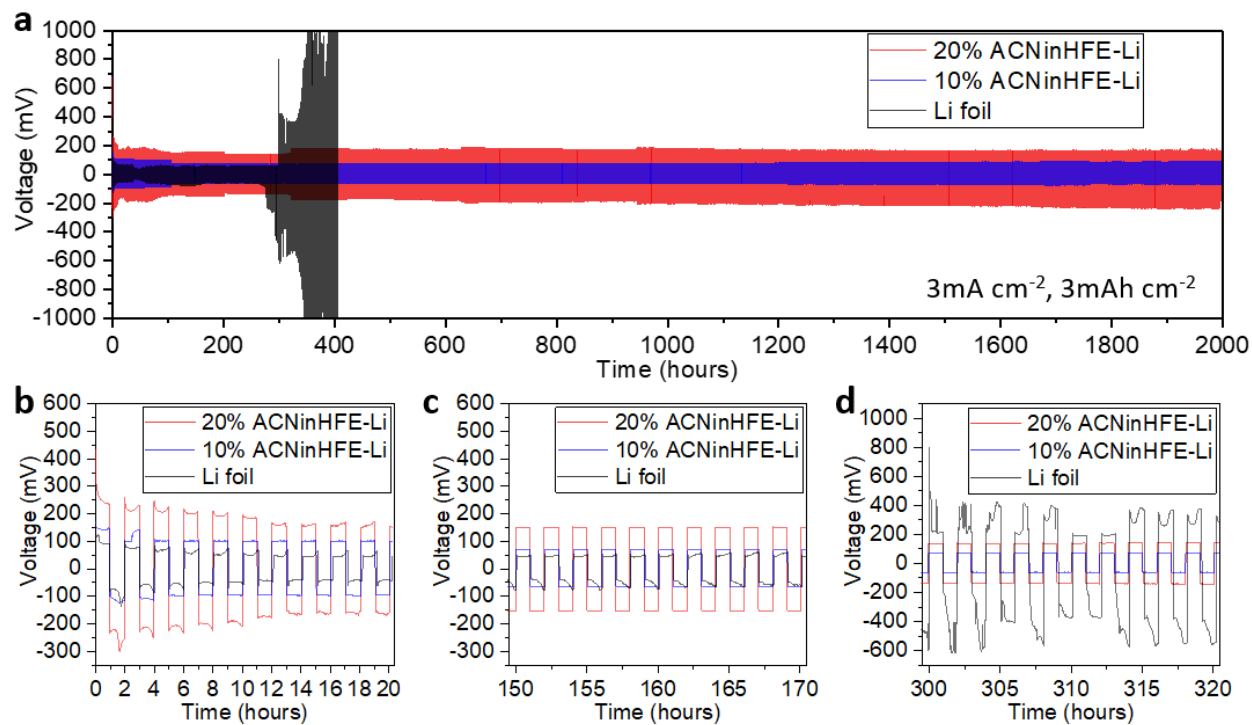


Figure 4. 13 Electrochemical stability of reinforced artificial SEI Li metal. (a) Galvanostatic cycling of symmetric cells with reinforced artificial SEI Li.

4.3.2 Batteries performance under lean electrolyte condition

The full cell (using $\text{LiNi}_{0.8}\text{Co}_{0.15}\text{Al}_{0.05}\text{O}_2$ (NCA) with high areal capacity upon 4.1 mAh cm^{-2} as cathode) batteries performance under lean electrolyte condition was tested paired with reinforced artificial SEI-Li ($30\text{ }\mu\text{m}$ Li foil used) anode with areal capacity of 6.18 mAh cm^{-2} . The aggressive low E/C ratio about 1.5 g (Ah)^{-1} was applied by using lean electrolyte amount of $1.25\text{ }\mu\text{l mAh}^{-1}$ for cells performance testing, which has high energy density of 423.3 Wh kg^{-1} . The ultrathin reinforced artificial SEI-Li | NCA and Li foil | NCA full cells performance at various lean electrolyte condition ($1.25\text{-}5\text{ }\mu\text{l mAh}^{-1}$) were collected (Figure 4.9a, c and e). NCA capacity degradation in reinforced artificial SEI-Li | NCA cell is obvious slower than Li foil | NCA cell at all electrolyte conditions. At electrolyte of $1.25\text{ }\mu\text{l mAh}^{-1}$, Li foil cells can't fully discharge at

first cycles, and 20% 1M LiTFSI in ACN and 80% HFE reacted Li and 10% 1M LiTFSI in ACN and 90% HFE reacted Li start to decay after 20 cycles. It is possibly due to electrolyte components consumption induced electrolyte exhausted at ultralow lean electrolyte condition cycling. As electrolyte increased to $5 \mu\text{l mA}^{-1}$, reinforced artificial SEI-Li (10% 1M LiTFSI in ACN and 90% HFE reacted Li) | NCA has considerable capacity retention of $\sim 85\%$ after 100 cycles based on standard capacity of 185 mA^{-1} , while Li foil | NCA cell cannot survived after 50 cycles. The voltage profiles (Figure 4.9b, d and f) under $5 \mu\text{l mA}^{-1}$ electrolyte condition revealed that Li foil has fast capacity decay according to intersection point of charge and discharge curve left shift.

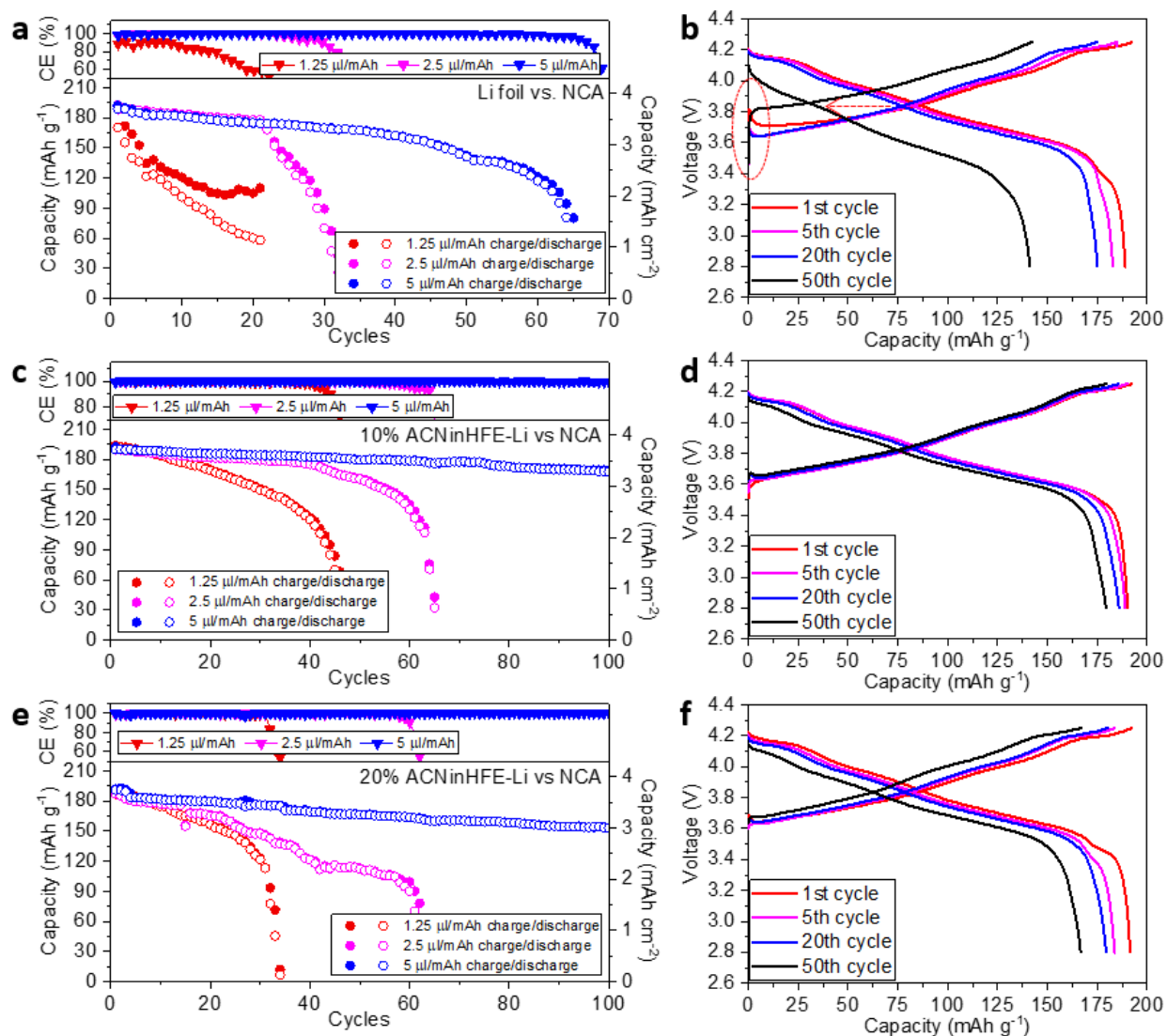


Figure 4.14 Battery performance of full cells at lean electrolyte conditions. Cycling capability and voltage profile of the Li foil/NCA battery and the reinforced artificial SEI Li metal/NCA battery NCA loading: 20.5 mg/cm².

The reinforced artificial SEI-Li full cell showed contact resistance of 11.1 Ω and transfer resistance of 99.6 Ω before cycling, while Li foil has contact resistance of 7.8 Ω and transfer resistance of 82.2 Ω respectively from EIS Nyquist plots (Figure 4.10a-b). Which indicated that reinforced artificial SEI-Li has slightly higher resistance at pristine status before cycling. After first cycle, the reinforced artificial SEI-Li maintained $\sim 10 \Omega$ in contact resistance and $\sim 40 \Omega$ in

transfer resistance, these stable resistances maintained after 50 cycles cycling. However, Li foil has increasing contact resistance $\sim 12 \Omega$ in and $\sim 118 \Omega$ in transfer resistance after 50 cycles. It indicates the reinforced artificial SEI-Li has great improvement in cycling performance in Li metal batteries.

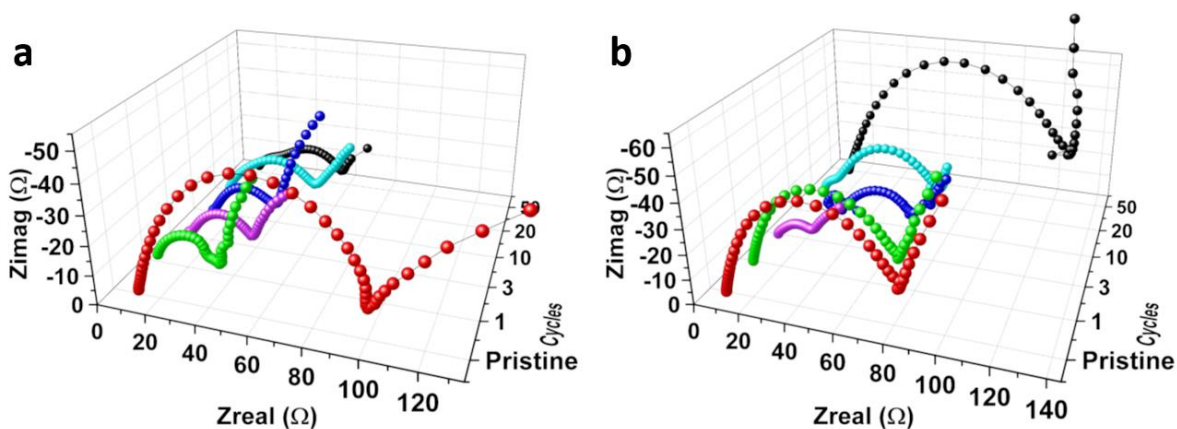


Figure 4. 15 Nyquist plots of pristine reinforced artificial SEI-Li (a) and Li foil (b) vs NMC 532 full cells from EIS measurements.

4.4 Experimental details

4.4.1 Experimental details of LiCFF electrochemical performance.

The electrochemical property and battery cycling performance were checked through symmetric and full coin cells (CR2032, Xingye Co., Ltd.). Specifically the Li plating/stripping was investigated via a symmetric cell that consists of LiCFFs as both anode and cathode electrodes. A symmetric cell with Li foils (99.9%, MTI Corp.) was also used for comparison. For the full cell battery, the slurry of cathode materials was prepared by mixing 85 wt% NMC622 as active material, 10 wt% conductive carbon black (SuperP C65, Timcal), and 5 wt% poly(vinylidene fluoride) (PVDF, average Mn $\sim 71,000$, Sigma-Aldrich) as binder in N-methyl-2-pyrrolidinone solution (NMP, Sigma- Aldrich). The mixture slurry was coated onto an aluminum

foil (thickness: 0.15 mm) with an active material loading of 5.0 mg/cm² until dried at 80 °C for 24 hours in a vacuum oven (Sheldon Manufacturing, Inc.). The LiCFF was directly used as anode electrode without additional slurry-making process. All the coin cells including symmetric and full cells were assembled using 1.0 M LiPF₆ dissolved in ethylene carbonate (EC) and DEC (1:1 volume ratio) as electrolyte (LP47, BASF Corp.) and Celgard 2400 microporous polyethylene film as separator inside the argon-filled glove box. The S cathodes were synthesized by heat treat the sulfur and Super P conductive carbon black mixtures (65:35) under 200 °C for 2 hours in furnace. A mixture of 0.1 M lithium nitrate (anhydrous, 99.999%, Alfa Aesar), 1.0 M lithium bis-trifluoromethane sulfonimide (LiTFSI, BASF Corp) in dioxolane (DOL)/dimethyl ether (DME) (BASF Corp) 1:1 volume ratio was used as electrolyte. The slurry of Super P-S cathode materials was prepared by mixing 90 wt% active material, 10 wt% poly(vinylidene fluoride) (PVDF, average Mn ~71,000, Sigma-Aldrich). The electrochemical impedance spectroscopy (EIS) measurements were carried out via a Gamry 600+ Potentiostat/Galvanostat/ZRA. All the Li plating/stripping and cycling performance of the battery at different current densities was conducted using galvanostatic charge/discharge method on a battery tester system (LANDT 2001CT, Landt Instruments, Inc.).

4.4.2 Experimental details of ILC-Li.

The electrochemical property and galvanostatic cycling performance were examined via symmetric and full CR2032 coin cells. Galvanostatic cycling for Li plating/stripping was investigated via a symmetric cell that constitutes of ILC-Li or rolled Li foil as both anode and cathode. For ILC-Li/Li | NMC532 full cell test, the cathode slurry was prepared by mixing 94 wt% NMC532 as active material, 4 wt% conductive carbon black (SuperP C65, Timcal), and 2 wt% poly(vinylidene fluoride) (PVDF, average Mn ~71,000, Sigma-Aldrich) as binder in N-methyl-2-

pyrrolidinone solution (NMP, Sigma- Aldrich). The mixed slurry was coated onto a 0.15 mm thick aluminum foil with an active material loading of 10 mg cm^{-2} until dried at $80 \text{ }^\circ\text{C}$ for 24 hours in a vacuum oven. For ILC-Li/Li | NCA lean electrolyte full cell test, the cathode used from 18650 types Samsung 35E batteries with active materials loading of 20.45 mg cm^{-2} . The prepared ILC-Li was directly used as anode without additional slurry-mixing process. The galvanostatic cycling and EIS test of ILC-Li/Li symmetric cell and ILC-Li/Li | AC-SiO-Sulfur were assembled using 1.0 M lithium bis-trifluoromethane sulfonimide (LiTFSI, BASF Corp) in dioxolane (DOL)/dimethyl ether (DME) (BASF Corp) 1:1 volume ratio and 0.1 M lithium nitrate (anhydrous, 99.999%, Alfa Aesar) as additive. The ILC-Li/Li | NMC532 and ILC-Li/Li | NCA full cells were assembled by using 1.0 M LiPF_6 dissolved in 3:7 weight ratios of EC and EMC with 2wt% VC as electrolyte. Celgard 2400 microporous polyethylene (PE) film was applied as separator. All cells assembling were carried out inside the argon-filled glove box. ILC-Li used in tests is $300 \mu\text{m}$ Li and $30 \mu\text{m}$ coated MXene, except lean electrolyte condition ILC-Li/Li | NCA full cells test by using $30 \mu\text{m}$ Li and $15 \mu\text{m}$ coated MXene. The sulfur cathode was synthesized by mixing the dissolved sulfur and double-net $\text{SiO}_2@AC$ framework¹⁰⁰ in toluene solution followed by evaporation, the received sample was heated under $200 \text{ }^\circ\text{C}$ for 2 hours in Argon. The double-net enclosed sulfur composite cathode slurry was mixed with carbon blacks and PVDF by ratio of 8:1:1. The sulfur loading in Aluminum foil is 2 mg cm^{-2} . The electrochemical impedance spectroscopy (EIS) measurements were checked by Gamry 600+ Potentiostat/Galvanostat/ZRA. All the Li plating/stripping and cycling performance of the battery at different current densities was conducted using galvanostatic charge/discharge method on a battery tester system (LANDT 2001CT, Landt Instruments, Inc.). CE of the MXene coated Cu current collector|Li and Cu current collector|Li cell was measured at 0.5 mA/cm^2 and

1mAh/cm². The Li stripping cutting off voltage is 2.5 V for MXene Cu current collector, 1V for Cu current collector. Electrolyte using is 1M LiTFSI.

4.4.3 Experimental details of reinforced artificial pre SEI

The electrochemical property and galvanostatic cycling performance were examined via symmetric and full CR2032 coin cells. Galvanostatic cycling for Li plating/stripping was investigated via a symmetric cell that constructed of reinforced artificial SEI-Li or Li foil as both anode and cathode. For reinforced artificial SEI-Li/Li foil | NMC532 full cell test, the cathode slurry was prepared by mixing 94 wt% NMC532 as active material, 4 wt% conductive carbon black (SuperP C65, Timcal), and 2 wt% poly(vinylidene fluoride) (PVDF, average Mn ~71,000, Sigma-Aldrich) as binder in N-methyl-2-pyrrolidinone solution (NMP, Sigma- Aldrich). The mixed slurry was coated onto a 0.15 mm thick aluminum foil with an active material loading of 10 mg cm⁻² until dried at 80 °C for 24 hours in a vacuum oven. For reinforced artificial SEI-Li/Li | NCA lean electrolyte full cell test, the cathode used from 18650 types Samsung 35E batteries with active materials loading of 20.45mg cm⁻². The prepared reinforced artificial SEI-Li was directly used as anode without additional slurry-mixing process. The galvanostatic cycling and EIS test of reinforced artificial SEI-Li/Li symmetric cell were assembled using 1.0 M LiPF₆ dissolved in 3:7 weight ratios of EC and EMC with 2wt% vinylene carbonate (VC) and 10% fluoroethylene carbonate (FEC) as electrolyte. Reinforced artificial SEI-Li/Li | NMC532 and reinforced artificial SEI-Li/Li | NCA full cells were assembled by using 1.0 M LiPF₆ dissolved in 3:7 weight ratios of EC and EMC with 2wt% VC and 10% FEC as electrolyte. Celgard 2400 microporous polyethylene (PE) film was applied as separator. All cells assembling were carried out inside the argon-filled glove box. Reinforced artificial SEI-Li used in tests is 10% 1M LiTFSI in ACN and 90% HFE mixture and 20% 1M LiTFSI in ACN and 80% HFE mixture for

lean electrolyte condition reinforced artificial SEI-Li/Li|NCA full cells test. The electrochemical impedance spectroscopy (EIS) measurements were checked by Gamry 600+ Potentiostat/Galvanostat/ZRA. All the Li plating/stripping and cycling performance of the battery at different current densities was conducted using galvanostatic charge/discharge method on a battery tester system (LANDT 2001CT, Landt Instruments, Inc.).

4.5 Conclusion

In Fig 2.19, the single-side LiCFF displayed ~1.5 times volumetric capacity, ~4 times gravimetric capacity, and ~9.6 times areal capacity of graphite, respectively. The LiCFF/NMC cell energy density estimation can reach to 258.9 W h/kg by considering 175 mA h/cm² as discharge capacity for NMC and NMC cathode loading of 20 mg/cm². It also needs to gain the 5 mg mass loading at Li-metal anode.

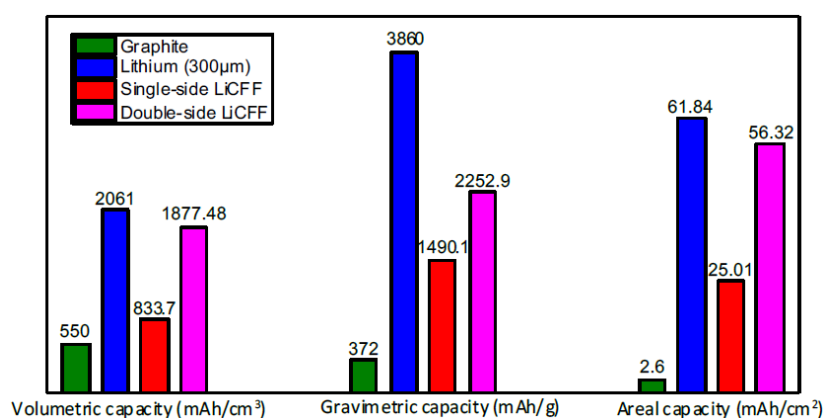


Figure 4. 16 Anode volume capacity, gravimetric capacity and areal capacity estimation in Graphite, Li foil single-side and double side LiCFF.

In this work, we designed a LiCFF composite with lithium-rich and lithium-poor sides as an novel “all-in-one” lithium metal anode. The lithiotropic commercial available carbon fiber was used to partially pre-store the molten lithium by ironing process. The ultimate simple fabrication process gives it possibility for large-scale production. The conductive 3D framework CFF protection on lithium metal comprehensive solved several challenges in conventional lithium metal. Single carbon fibers deliver an excellent electrical conductivity and Li⁺ transportation, thus diminishing the energy barrier for Li nucleation/growth and reducing the

polarization at LiCFF-electrolyte interface. Through electrochemical test and morphology characterization, LiCFF showed that it can minimize the mossy/dendritic lithium growth induced infinite volume change. LiCFF also improve the coulombic efficiency and stabilize the solid electrolyte interface as a Li metal anode. The electrochemical characterization including symmetric and full-cell batteries provides a reliable cyclability under very low overpotential at high current densities and operation capacities. The controllable mass loading of Li metal make the LiCFF based full batteries has ability to control the N/P ratio, thus boosting the energy density of Li metal batteries. Its outstanding performance provides a rational design of high energy density lithium ion battery for electrical vehicles and portable electrical devices applications.

In conclusion, a self-exfoliated MXene coated 30 μm ultrathin Li metal anode was developed by facile rolling process. The multilayer lamination nanosheets architecture with excellent conductivity enabled fast Li^+/e^- migration and Li deposition preference interface, which reduced local effect current densities, for Li plating/stripping. In addition, lamination configuration physic-chemically regulated Li growth among interlayer and inter-block space. Therefore, dendritic/mossy type Li growth was effectively suppressed via homogeneous Li growth upon MXene nanosheets. Besides, ILC-Li minimized the Li and electrolyte components during cycling resulting a notable thinner inorganic-rich SEI than Li foil. As an ultrathin low N/C ratio, dendrite free and high robustness Li metal anode, ILC-Li is a great potential anode in high energy density Li-metal batteries over 366.6 Wh kg^{-1} . Stable and reliable performance in both symmetric and full cell batteries with ILC-Li as anode under different current densities and lean electrolyte condition displayed future practical application in energy storage in portable devices and electric vehicles.

To summarize, a facile drop coating made reinforced artificial SEI ultrathin Li metal anode was developed to suppress mossy/dendritic Li. The 1M LiTFSI in ACN and HFE mixed solvent was carried out to *in-situ* react at Li metal surface. The reaction produced a reliable electro-chemo-mechanical stable Li metal electrode with a highly reversible Li plating/stripping under large current density of 3 mA cm⁻². The synthetic artificial SEI has successfully modified the components and composition in traditional SEI. The thicker organic components embedded with less than 5nm inorganic components enhanced the mechanical properties and Li ion transport ability. The excellent uniform Li distribution after Li cycling revealed that the reinforced artificial SEI lead to a homogeneous deposition/dissolution of Li with less volume change. In parallel, both symmetric cell and full cell batteries by using reinforced artificial SEI-Li electrode showed a high capacity retention under lean electrolyte condition. Especially, a full Li metal battery paired with NCA showed an high energy density of ~423.3 Wh/kg can running over 50 cycles. Capacity retention maintained over 90% after 100 cycles in 280.8 Wh/kg energy density level cell. This reinforced artificial SEI-Li electrode greatly provide an innovate method for artificial SEI developments.

Chapter 4 is a reprint of the publication “Chen, X., Lv, Y., Shang, M. & Niu, J. Ironing Controllable Lithium into Lithiotropic Carbon Fiber Fabric: A Novel Li-Metal Anode with Improved Cyclability and Dendrite Suppression. *ACS Applied Materials & Interfaces* 11, 21584–21592 (2019)” and “Chen, X., Shang, M. & Niu, J. Inter-layer-calated Thin Li Metal Electrode with Improved Battery Capacity Retention and Dendrite Suppression. *Nano Lett.* **20**, 2639–2646 (2020)”, copyright of American Chemical Society. The dissertation author is the first author and co-writer of this publication. Chapter 4 is also a reprint of the manuscript under preparation “Chen, X., Shang, M. & Niu, J. An electro-chemo-mechanical stable artificial pre

SEI design for Li metal anode with enhanced batteries performance.”, The dissertation author is the first author and co-writer of this manuscript.

CHAPTER 5 Li Metal-LiPON Interface Evolution

Observation by *in-situ* TEM

5.1 Introduction

Instable Li-SSE interface induced interfacial impedance issues are one of the most dominated challenges for Li metal based all solid-state battery system. At interface between Li metal and oxide and sulfide based inorganic solid state electrolyte (SSE), the SSE decomposed to Li-contained compounds which has low ionic conductivity.^{10,61} The sluggishness of Li ion transport kinetic at these passivated interfaces will lead to high overpotential and resistance in electrochemical measurements. When passivated SEI is formed to a certain thickness and reached reaction dynamic equilibrium, it mitigates interface reaction and protects the SSE from further decompositions. Therefore, it formed high energy barrier for Li ion transport and sluggish the charging/discharging. On the other hand, Li dendrites formation induced safety concerns and all solid state batteries failure are one of the major issues.¹⁰¹ In typical SSE Li dendrites form from void flaws at Li-SSE interface and grew into grain boundaries at most inorganic SSE.¹⁰²⁻¹⁰⁴ In organic based SSE particular Poly Ethylene Oxide (PEO) electrolyte exhibit high stability paired with Li metal anode.^{105,106} But it also suffered from interface passivation after cycling, instabilities under high voltage and dendrite formation issues. Hence, solving the comprehensive electro-chemo-mechanical problems at interface will be one of most important research direction related SSE.

Among the most successful solid electrolyte candidates, Li phosphorus oxynitride (LiPON) exhibit superior electrochemical stability high volumetric/gravimetric energy density

and relatively high ionic conductivity (10^{-6} S/cm²).¹⁸ Excellent compatibility with a variety of anode/cathode materials and wide electrochemical stable windows during cycling are recognized as its most outstanding advantages, since LiPON was invented in early 1990s at Oak Ridge National Laboratory.⁵⁵ LiPON was illustrated to be stable from 0V to 5V with respect to Li/Li⁺ references by impedance spectra.¹⁰⁷ Also, LiPON is chemically stable with lithium by measuring impedance spectra under three electrode cell scales.¹⁰⁷ Then, metallic lithium and LiPON (Li/LiPON) based thin film batteries system were successfully fabricated, such as Li/LiPON/LiCoO₂,^{108,109} Li/LiPON/LiMn₂O₄,¹¹⁰ Li/LiPON/Li_x(Ni_yMn_{1-y})_{2-x}O₂ systems.¹¹¹ Furthermore, LiPON was introduced to be a stable electrolyte and artificial SEI for enabling the high voltage batteries with Li as anode and LiNi_{0.5}Mn_{1.5}O₄ as 5V cathode materials.¹¹² Up to 10000 cycles of cycling performance and 99.99% columbic efficiency also indicate ultimate high stability of LiPON under such high voltages.¹⁹ Moreover, LiPON was utilized as protective layer for metallic Li to prolong the lifespan and improved Li plating/stripping efficiency in pouch cell as well.¹¹³ Nevertheless, a large amount of experimental results displayed exceptional stability performance in Li/LiPON based SSE batteries and the mechanism about its excellent stability performance is not well known. Thus, using the advanced microscopy techniques to elucidate the LiPON-Li metal interface evolution is the importance of this work.

5.2 Experiments details

200 mesh copper grids were cut to a half grid, and it was carefully mounted with melting epoxy. To prepare the wedged half grid, the epoxy mounted half grid was polished by TechprepTM polisher under spinning speed of 140rpm. Then, the epoxy on half grid was removed by acetone and methanol accompanying by sonication process. Next, the half grid was ion milled by a Fischione Instruments low angle ion milling and polishing system. The ion milling operation parameter is 6kV, 5mA and ~0.5 sccm, 4.0×10^{-4} Torr, 15° milling angles and 15 minutes milling time. The LiPON deposition was performed via radio frequency magnetron sputtering method.¹¹⁴ The Li_3PO_4 was sputtered onto copper half grid with N_2 flow under pressure of $\sim 3 \times 10^{-6}$ Torr. The ~100nm LiPON was deposited onto the copper half grid tips.

The LiPON deposited copper half grids were placed in a double tilt Nanofactory holder for in-situ TEM experiments (Figure 5.1). A tungsten wire was used to scratch the Li metal surface, then it was mounted onto a piezo controlled STM tip. The holder was transferred to TEM with less than 1 minute air exposure time. To get a pure Li metal for in-situ TEM experiments, the electron beam was used to remove the surface LiOH and Li_2CO_3 . The Li metal containing tips were carefully derived by piezo-tube to contact LiPON. The in-situ holder was then applied bias between LiPON-Li for further observation.

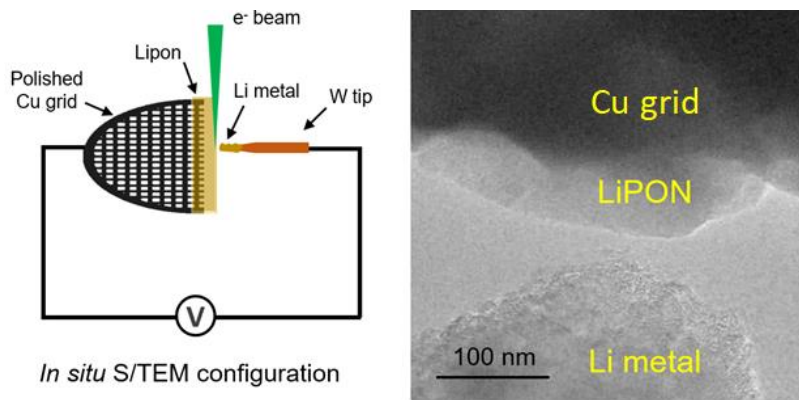


Figure 5. 1 Experimental setup for observing the interface between metallic Li and LiPON by using *in-situ* S/TEM and TEM images.

5.3 results and analysis

Here, we demonstrated a dynamic Li/LiPON interface formation by using *in-situ* scanning/transmission electron microscope(S/TEM) coupled with electron energy loss spectroscopy (EELS) characterization. The real time Li/LiPON interfacial morphology evolutions with simultaneous galvanostatic biasing from 0V to 5V were monitored by using our previous Li/SSE interface in-situ experimental setup.¹¹⁵ Additionally, the interfacial decomposition reactions induced interfacial elemental distribution change were evaluated based on EELS analysis. Moreover, the extremely sluggish or discontinuous in interfacial reactions kinetics was verified after certain period of visible interfacial reactions. To evaluate the interfacial morphological and elemental distribution evolutions before and after Li/LiPON interface formation, the traditional focused ion beam multi-layer samples are not idea sample preparation method for this experiment. Amorphous LiPON were coated at specific edge in copper-based TEM half grids forked tips with hundreds nanometer thickness by radio frequency magnetron sputtering. Considering that lithium metal is easily oxidized in the air environment, possible contaminants on the surface of Li metal (attached in a tungsten tip) was vanished by highly convergent electron beam. Then, piezotube controlled accurate tip movement enable the Li/LiPON contact by using Nanofactory in-situ biasing holder. All the interface growth and chemistry evolution kinetics were analyzed as functions of real time.

The dynamic interfacial evolution of the LiPON/Li interface was elucidated by *in-situ* TEM. The LiPON-Li potential interfacial reaction processes based on distinctive reaction processes which lead to different volume changes as the reaction progresses (Figure 5.2).

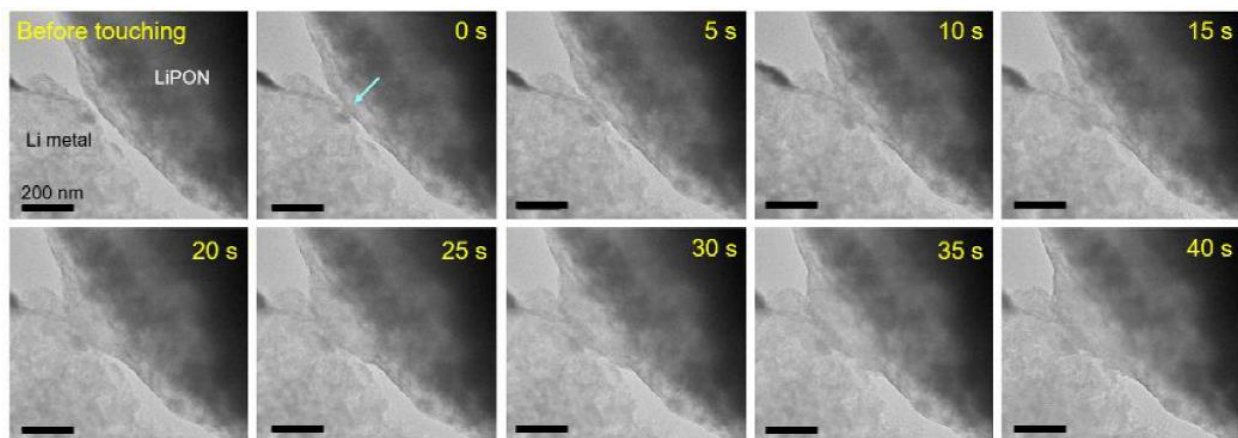


Figure 5. 2 The TEM images of interfacial reaction of LiPON-Li, which start from pristine LiPON and Li metal before contacting, after contacting to 40 seconds.

The interface area expansion ratio, which is calculated based on pre-defined area of pristine LiPON before contacting. The area based on ImageJ pixel was applied to estimate the volume evolution of the interfacial reaction area. The area expansion ratio based on highlighted pre-defined LiPON area (Figure 5.3), was evaluated as a function of time to reveal interface reaction progresses. Our experimental result showed that the volume increases almost linearly from 1.0 to ~ 1.5 during the first 40 seconds of touching LiPON with Li metal. It eventually approaches stable and no further evolution after the interfacial layer becomes ~ 60 nm thick. It suggests the interfacial reaction reaches equilibrium around 45 seconds. In reaction zone after 45 seconds, the interface reaction almost stopped and falls into dynamic equilibrium, even after an external bias of 5V was applied. The discontinuous reaction phenomenon results suggest that the formation of an passivation interlayer is the key to a wide electrochemical stability of LiPON with Li metal anode.

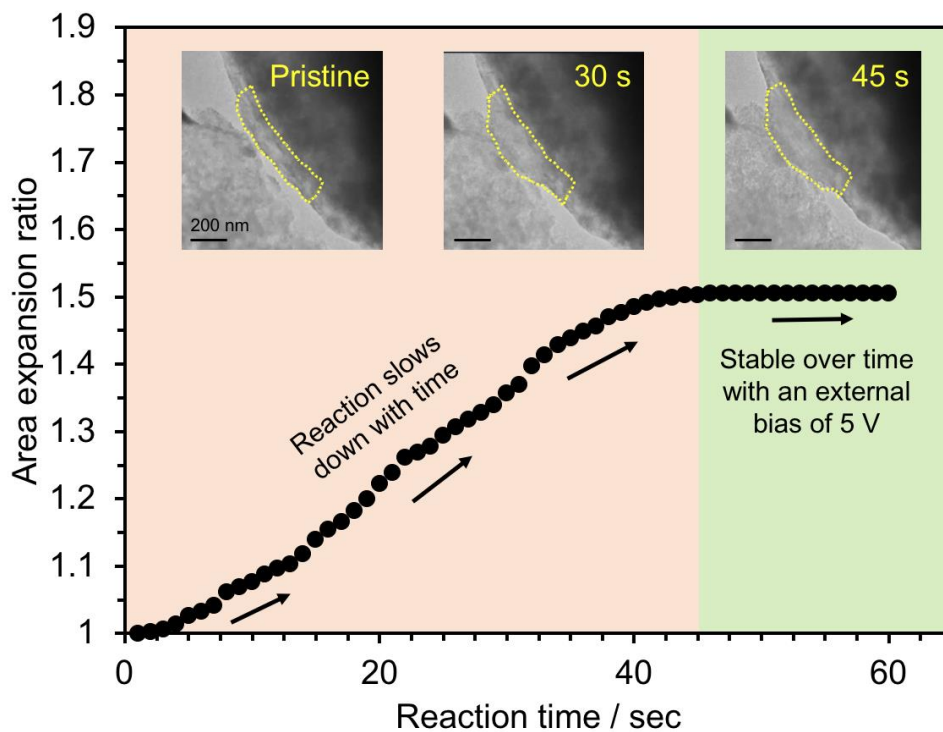


Figure 5. 3 LiPON-Li interfacial reaction area expansion ratio as a function of time.

Estimation based on stoichiometry of LiPON is $\text{Li}_{2.9}\text{PO}_{3.3}\text{N}_{0.46}$. The Table S1 displayed the volume of Li_3P , Li_3N and Li_2O as reaction products. There is a 203.5% volume change based on the density and molar mass of the LiPON and reaction products. If we simplify the Li/LiPON interface topography to a semi-cylindrical model, and half-arc surface in semi-cylindrical model as observation direction. The estimated area expansion ratio is 1.43. This also coincides with the observed areal expansion ratio (~1.5).

Table 5. 1 Volume of $\text{Li}_{2.9}\text{PO}_{3.3}\text{N}_{0.46}$, Li_3P , Li_3N and Li_2O based on standard molar mass and density.

	Molar mass (g/mol)	Density (g/cm ³)	Mole	Volume (cm ³)
$\text{Li}_{2.9}\text{PO}_{3.3}\text{N}_{0.46}$	110.342	2.3	1	47.974783
Li_3P	51.796	1.44	1	35.969444
Li_3N	34.823	1.27	0.46	12.613055
Li_2O	29.882	2.01	3.3	49.06

Recent computational studies have illustrated the electrochemical stability for the Li/LiPON interface and other typical SSE interface by First Principle calculations and Density Functional Theory (DFT) calculations.^{116,117,118} These studies indicate that excellent stability of SSE is not inherent thermodynamically stable but kinetic stabilization. Exteriorly wide electrochemical window observed in many experimental results are due to sluggish kinetics of the interfacial decomposition reactions induced high overpotentials. Besides, the voltage ranges where the Li/LiPON interface and possible interfacial decomposition products are thermodynamically stable and unstable were included in these computational simulations as well. In addition, experimental studies based on in-situ XPS verified that existence of Li/LiPON interfacial chemical reactions lead to the decomposition into smaller units like Li_3PO_4 , Li_3P , Li_3N , and Li_2O .¹¹⁹ However, there are limited experimental reports detailing the atomic-level understanding of the interface between metallic lithium and LiPON, yet this understanding is important for enhancing the performance of LiPON-based all-solid-state thin film batteries.

The chemical composition of LiPON-Li reaction interlayer at interface was further identified via EELS spectra acquisition. EELS spectra including Li K-edge, P K-edge, N K-edge and O K-edge were collected for both interlayer after reaction and pristine LiPON samples. There are significantly differences between pristine LiPON and interlayer at interface showed in

Li K-edge. There are several distinct peaks in pristine LiPON, which corresponding to multiple nearest neighbors of Li atoms in LiPON. However, only 2 characteristic peaks showed in interface after reaction, which indicating overlapped multiple lithium compounds peaks. According to the Li K-edge spectra differentiation of Li bonding configuration, the LiPON decomposition and chemical reaction induced phase change is very likely occurred after contacting with Li.

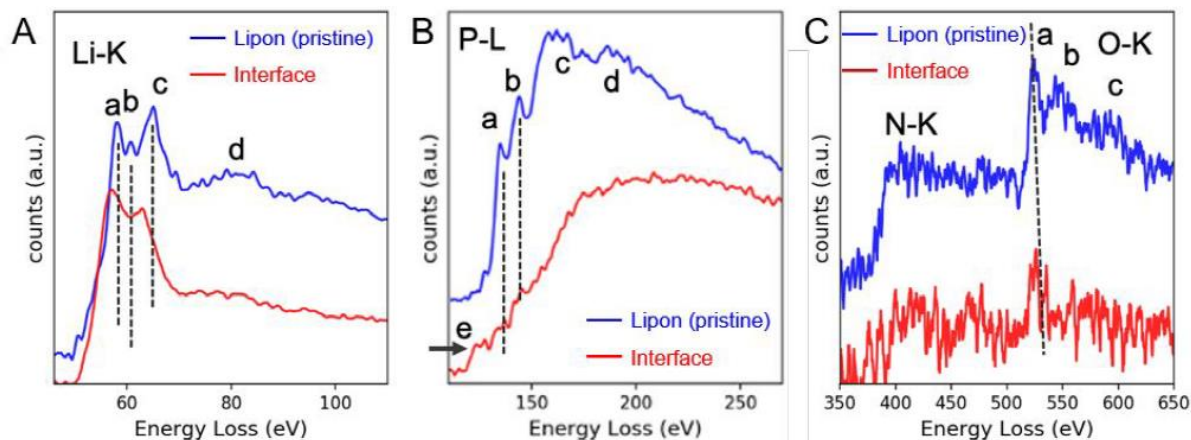


Figure 5. 4 EELS Li K-edge, P K-edge, N K-edge and O K-edge spectra analysis of pristine LiPON and LiPON-Li interface after interfacial reaction.

5.4 Conclusion

LiPON is known as its stability among all SSE candidates. We reported a nano-scale reaction observation at interface of lithium metal anode and LiPON in a real time, high spatial resolution by using in-situ S/TEM. The results showed that Li metal will react with LiPON after a ~45 seconds by contacting each other. This interfacial reaction formed intermediate phases with a thickness of about 60 nm. The intermediate phases that is both Li⁺ conductive and electrically insulating. It was found to be stable under an external bias of 5V without further passivation or growing. It is precisely because this intermediate layer brings excellent stability performance at Li metal LiPON interface. This work highlighted the key role of interphase formation between lithium metal anodes and advanced solid electrolytes. Therefore, the chemical composition, morphology, and comprehensive properties of the interphases can be connected to battery performance and shed light for better engineering interphase designing in future Li metal batteries.

Chapter 5 is a reprint of the submitted manuscript “Hood, Z.*, Chen, X.*(Co-first author), Liu, X., Sacci, R., Dudney, N., Niu, J. & Chi, M. Elucidating Interfacial Stability between Lithium Metal Anode and LiPON via In-Situ Electron Microscopy.”, which under 3rd round revision at Nano Letter, Copyright of American Chemical Society. The dissertation author is the co-first author and co-writer of this manuscript.

CHAPTER 6 Summary and Outlooks

The two primary challenges including mossy/dendritic Li dendrites growing and low Coulomb efficiency were widely regarded as obstacles for development of practical lithium metal batteries. Being motivated to push lithium metal batteries into a practical application, it provides several Li metal-electrolyte interface treatment methods by using novel advanced materials and surface reaction reagents. Several Li metal treatment methods have significantly improved the cycling performance of lithium metal anode under high energy density batteries operation conditions. The revelation of the mechanism also can provide help for subsequent research. In this Li metal batteries related dissertation with main title of ‘Developing highly reversible Li metal anode with mossy/dendritic Li suppression in high energy density batteries’, the scientific contributions are summarized here:

A dual-sides (Li-rich, Li-poor sides) conductive Li host-CFF structure was firstly applied on Li metal host for dendritic Li suppression and SEI stabilization. The excellent Li^+/e^- conductivity of CFF host enabling a drastically lowered energy barrier for Li nucleation/growth were revealed by electrochemical characterization. A uniform current distribution results in forming a homogeneous Li layer instead of forming dendrite were exhibited by in-situ capillary cell and ex-situ SEM morphology evolution characterization. Even if part of the energy density is sacrificed by introducing the CFF, the anode gravimetric capacity of LiCFF can achieve about 4-10 times of commercial Graphite. The practical cell by using LiCFF paired with NMC cathode has energy density of 258.9 W h/kg. It provides a successful model by using commercialized carbon fiber fabrics to design the lithium-carbon composites anode materials.

A novel 2D nanomaterials MXene stacks were applied to suppress Li dendrites growth on Li metal anode by simple rolling process. An interesting inter-layer-calated mechanism was found that Li metal can be stored inside both primary and secondary interlayers of MXene stacks. ILC-Li electrode perform excellent Li^+/e^- conductivity and high accommodation for Li plating/stripping. The high surface area ILC-Li significantly reduced local effect current densities resulting in a uniform Li deposition/dissolution and Li dendrites suppression. Through an advanced XPS depth profiling analysis, the ILC-Li electrode exhibited excellent Li ion transport kinetics which owing to thinner inorganic-SEI formation. In full batteries operation, the N/P ratio and electrolyte amount is strictly controlled by using ultrathin Li ($30\mu\text{m}$) in ILC-Li. The high energy density of 366.6 Wh/kg was achieved in a long cycling ILC-Li. This novel approach provides a successful scalable rolling process to design the 2D materials MXene lithium composites anode materials.

A chemical surface treatment method was applied to develop artificial SEI for highly reversible Li metal anode. The facile one step solution drop coating methods was used to construct a reinforced artificial SEI at Li metal surface. The reinforced artificial SEI was characterized to have a uniformly distribution of several nanometer inorganic lithium compounds among organic SEI substrate, which was known to be electro-chemo-mechanical stable in Li plating/stripping. The full cell batteries by using ultrathin reinforced artificial SEI-Li provide an over 423.3 Wh/kg level energy density under ultra-lean electrolyte conditions. This novel method deliver an idea to redesign SEI in conventional lithium metal batteries which can enhance the cyclability and boost the energy density.

LiPON, a widely known conventional solid-state electrolytes with is regarded as wide-range electrochemical stable window and excellent compatibility with many electrode materials.

Reasons for its high stability was studied at LiPON and Li metal interface by using advanced in-situ TEM biasing setup. The interface was observed no further reaction after contacting 45 seconds by even at an external bias of 5V. The possibly forming of lithium compounds such as Li_3P , Li_3N and Li_2O at thin passivation layer, which was considered as root cause of prevention for further reactions at interface. This passivation interlayer was characterized with ~60 nm dimension which is Li ion conducting and electron insulating for Li dendrites suppression. It revealed the mechanism of LiPON-Li metal interface stability, hence provide a possible designing ideal for future Li metal batteries.

Collectively, several methods were conducted to achieve a high reversible Li metal anode. The laboratory-grade made batteries with comprehensive electrochemical performance, materials characterization results and mechanism analysis have instructive meaning for developing practical high energy lithium metal batteries in future.

REFERENCES

1. Tarascon, J.-M. & Armand, M. Issues and challenges facing rechargeable lithium batteries. *Nature* **414**, 359–367 (2001).
2. Armand, M. & Tarascon, J.-M. Building better batteries. *Nature* **451**, 652–657 (2008).
3. Liu, J. *et al.* Pathways for practical high-energy long-cycling lithium metal batteries. *Nat Energy* **4**, 180–186 (2019).
4. Niu, C. *et al.* High-energy lithium metal pouch cells with limited anode swelling and long stable cycles. *Nat Energy* **4**, 551–559 (2019).
5. Weber, R. *et al.* Long cycle life and dendrite-free lithium morphology in anode-free lithium pouch cells enabled by a dual-salt liquid electrolyte. *Nat Energy* **4**, 683–689 (2019).
6. Louli, A. J. *et al.* Diagnosing and correcting anode-free cell failure via electrolyte and morphological analysis. *Nat Energy* **5**, 693–702 (2020).
7. Xu, W. *et al.* Lithium metal anodes for rechargeable batteries. *Energy Environ. Sci.* **7**, 513–537 (2014).
8. Lin, D., Liu, Y. & Cui, Y. Reviving the lithium metal anode for high-energy batteries. *Nature Nanotechnology* **12**, 194–206 (2017).
9. Winter, M., Barnett, B. & Xu, K. Before Li Ion Batteries. *Chem. Rev.* **118**, 11433–11456 (2018).
10. Cheng, X.-B., Zhang, R., Zhao, C.-Z. & Zhang, Q. Toward Safe Lithium Metal Anode in Rechargeable Batteries: A Review. *Chemical Reviews* **117**, 10403–10473 (2017).
11. Cohen, Y. S., Cohen, Y. & Aurbach, D. Micromorphological Studies of Lithium Electrodes in Alkyl Carbonate Solutions Using in Situ Atomic Force Microscopy. *The Journal of Physical Chemistry B* **104**, 12282–12291 (2000).

12. Bai, P., Li, J., Brushett, F. R. & Bazant, M. Z. Transition of lithium growth mechanisms in liquid electrolytes. *Energy & Environmental Science* **9**, 3221–3229 (2016).
13. Ding, F. *et al.* Dendrite-Free Lithium Deposition via Self-Healing Electrostatic Shield Mechanism. *Journal of the American Chemical Society* **135**, 4450–4456 (2013).
14. Li, W. *et al.* The synergetic effect of lithium polysulfide and lithium nitrate to prevent lithium dendrite growth. *Nature Communications* **6**, (2015).
15. Qian, J. *et al.* High rate and stable cycling of lithium metal anode. *Nature Communications* **6**, (2015).
16. Zheng, J. *et al.* Electrolyte additive enabled fast charging and stable cycling lithium metal batteries. *Nature Energy* **2**, (2017).
17. Zhang, X.-Q., Cheng, X.-B., Chen, X., Yan, C. & Zhang, Q. Fluoroethylene Carbonate Additives to Render Uniform Li Deposits in Lithium Metal Batteries. *Advanced Functional Materials* **27**, 1605989 (2017).
18. Dudney, N. J. Solid-state thin-film rechargeable batteries. *Materials Science and Engineering: B* **116**, 245–249 (2005).
19. Li, J., Ma, C., Chi, M., Liang, C. & Dudney, N. J. Solid Electrolyte: the Key for High-Voltage Lithium Batteries. *Advanced Energy Materials* **5**, 1401408 (2015).
20. Zhou, W. *et al.* Plating a Dendrite-Free Lithium Anode with a Polymer/Ceramic/Polymer Sandwich Electrolyte. *Journal of the American Chemical Society* **138**, 9385–9388 (2016).
21. Zheng, G. *et al.* Interconnected hollow carbon nanospheres for stable lithium metal anodes. *Nature Nanotechnology* **9**, 618–623 (2014).
22. Liang, X. *et al.* A facile surface chemistry route to a stabilized lithium metal anode. *Nature Energy* **2**, (2017).

23. Liu, Y. *et al.* Making Li-metal electrodes rechargeable by controlling the dendrite growth direction. *Nature Energy* **2**, (2017).
24. Liang, Z. *et al.* Composite lithium metal anode by melt infusion of lithium into a 3D conducting scaffold with lithiophilic coating. *Proceedings of the National Academy of Sciences* **113**, 2862–2867 (2016).
25. Lin, D. *et al.* Layered reduced graphene oxide with nanoscale interlayer gaps as a stable host for lithium metal anodes. *Nature Nanotechnology* **11**, 626–632 (2016).
26. Liu, Y. *et al.* Lithium-coated polymeric matrix as a minimum volume-change and dendrite-free lithium metal anode. *Nature Communications* **7**, (2016).
27. Yang, C. *et al.* Ultrafine Silver Nanoparticles for Seeded Lithium Deposition toward Stable Lithium Metal Anode. *Advanced Functional Materials* **29**, 1702714 (2017).
28. Yang, C.-P., Yin, Y.-X., Zhang, S.-F., Li, N.-W. & Guo, Y.-G. Accommodating lithium into 3D current collectors with a submicron skeleton towards long-life lithium metal anodes. *Nature Communications* **6**, (2015).
29. Lu, L.-L. *et al.* Free-Standing Copper Nanowire Network Current Collector for Improving Lithium Anode Performance. *Nano Letters* **16**, 4431–4437 (2016).
30. Wood, K. N. *et al.* Dendrites and Pits: Untangling the Complex Behavior of Lithium Metal Anodes through Operando Video Microscopy. *ACS Central Science* **2**, 790–801 (2016).
31. Bai, P. *et al.* Interactions between Lithium Growths and Nanoporous Ceramic Separators. *Joule* **2**, 2434–2449 (2018).
32. Kushima, A. *et al.* Liquid cell transmission electron microscopy observation of lithium metal growth and dissolution: Root growth, dead lithium and lithium flotsams. *Nano Energy* **32**, 271–279 (2017).

33. Lu, D. *et al.* Failure Mechanism for Fast-Charged Lithium Metal Batteries with Liquid Electrolytes. *Advanced Energy Materials* **5**, 1400993 (2015).
34. Liu, K., Liu, Y., Lin, D., Pei, A. & Cui, Y. Materials for lithium-ion battery safety. *SCIENCE ADVANCES* **12** (2018).
35. Peled, E. & Menkin, S. Review—SEI: Past, Present and Future. *Journal of The Electrochemical Society* **164**, A1703–A1719 (2017).
36. Pinson, M. B. & Bazant, M. Z. Theory of SEI Formation in Rechargeable Batteries: Capacity Fade, Accelerated Aging and Lifetime Prediction. *Journal of The Electrochemical Society* **160**, A243–A250 (2013).
37. Wu, B., Lochala, J., Taverne, T. & Xiao, J. The interplay between solid electrolyte interface (SEI) and dendritic lithium growth. *Nano Energy* **40**, 34–41 (2017).
38. Pei, A., Zheng, G., Shi, F., Li, Y. & Cui, Y. Nanoscale Nucleation and Growth of Electrodeposited Lithium Metal. *Nano Letters* **17**, 1132–1139 (2017).
39. Chandrashekar, S. *et al.* ⁷Li MRI of Li batteries reveals location of microstructural lithium. *Nature Materials* **11**, 311–315 (2012).
40. Chen, K.-H. *et al.* Dead lithium: mass transport effects on voltage, capacity, and failure of lithium metal anodes. *Journal of Materials Chemistry A* **5**, 11671–11681 (2017).
41. Chen, X., Lv, Y., Shang, M. & Niu, J. Ironing Controllable Lithium into Lithiotropic Carbon Fiber Fabric: A Novel Li-Metal Anode with Improved Cyclability and Dendrite Suppression. *ACS Applied Materials & Interfaces* **11**, 21584–21592 (2019).
42. Wood, K. N., Noked, M. & Dasgupta, N. P. Lithium Metal Anodes: Toward an Improved Understanding of Coupled Morphological, Electrochemical, and Mechanical Behavior. *ACS Energy Letters* **2**, 664–672 (2017).

43. Li, Y. *et al.* Atomic structure of sensitive battery materials and interfaces revealed by cryo-electron microscopy. *Science* **358**, 506–510 (2017).
44. An, S. J. *et al.* The state of understanding of the lithium-ion-battery graphite solid electrolyte interphase (SEI) and its relationship to formation cycling. *Carbon* **105**, 52–76 (2016).
45. Peled, E., Golodnitsky, D. & Ardel, G. Advanced Model for Solid Electrolyte Interphase Electrodes in Liquid and Polymer Electrolytes. *J. Electrochem. Soc.* **144**, L208–L210 (1997).
46. Fang, C. *et al.* Quantifying inactive lithium in lithium metal batteries. *Nature* **572**, 511–515 (2019).
47. Zhou, Y. *et al.* Real-time mass spectrometric characterization of the solid–electrolyte interphase of a lithium-ion battery. *Nat. Nanotechnol.* **15**, 224–230 (2020).
48. Lang, J., Qi, L., Luo, Y. & Wu, H. High performance lithium metal anode: Progress and prospects. *Energy Storage Materials* **7**, 115–129 (2017).
49. Yan, C. *et al.* Dual-Layered Film Protected Lithium Metal Anode to Enable Dendrite-Free Lithium Deposition. *Advanced Materials* **30**, 1707629 (2018).
50. Shiraishi, S. Surface Condition Changes in Lithium Metal Deposited in Nonaqueous Electrolyte Containing HF by Dissolution-Deposition Cycles. *Journal of The Electrochemical Society* **146**, 1633 (1999).
51. Suo, L., Hu, Y.-S., Li, H., Armand, M. & Chen, L. A new class of Solvent-in-Salt electrolyte for high-energy rechargeable metallic lithium batteries. *Nature Communications* **4**, (2013).
52. Pang, Q. *et al.* Tuning the electrolyte network structure to invoke quasi-solid state sulfur conversion and suppress lithium dendrite formation in Li–S batteries. *Nature Energy* **3**, 783–791 (2018).

53. Manthiram, A., Yu, X. & Wang, S. Lithium battery chemistries enabled by solid-state electrolytes. *Nature Reviews Materials* **2**, (2017).
54. Croce, F., Appetecchi, G. B., Persi, L. & Scrosati, B. Nanocomposite polymer electrolytes for lithium batteries. **394**, 3 (1998).
55. Bates, J. B. *et al.* Fabrication and characterization of amorphous lithium electrolyte thin films and rechargeable thin-film batteries. *Journal of Power Sources* **43**, 103–110 (1993).
56. Stramare, S., Thangadurai, V. & Weppner, W. Lithium Lanthanum Titanates: A Review. *Chemistry of Materials* **15**, 3974–3990 (2003).
57. Park, H., Jung, K., Nezafati, M., Kim, C.-S. & Kang, B. Sodium Ion Diffusion in Nasicon ($\text{Na}_3\text{Zr}_2\text{Si}_2\text{PO}_{12}$) Solid Electrolytes: Effects of Excess Sodium. *ACS Applied Materials & Interfaces* **8**, 27814–27824 (2016).
58. Nagao, M. *et al.* All-solid-state Li–sulfur batteries with mesoporous electrode and thio-LISICON solid electrolyte. *Journal of Power Sources* **222**, 237–242 (2013).
59. Cussen, E. J. The structure of lithium garnets: cation disorder and clustering in a new family of fast Li^+ conductors. *Chem. Commun.* 412–413 (2006) doi:10.1039/B514640B.
60. Tatsumisago, M., Nagao, M. & Hayashi, A. Recent development of sulfide solid electrolytes and interfacial modification for all-solid-state rechargeable lithium batteries. *Journal of Asian Ceramic Societies* **1**, 17–25 (2013).
61. Manthiram, A., Yu, X. & Wang, S. Lithium battery chemistries enabled by solid-state electrolytes. *Nature Reviews Materials* **2**, (2017).
62. Kim, M. S. *et al.* Langmuir–Blodgett artificial solid-electrolyte interphases for practical lithium metal batteries. *Nature Energy* **3**, 889–898 (2018).

63. Xu, R. *et al.* Artificial Soft-Rigid Protective Layer for Dendrite-Free Lithium Metal Anode. *Advanced Functional Materials* **28**, 1705838 (2018).
64. Kazyak, E., Wood, K. N. & Dasgupta, N. P. Improved Cycle Life and Stability of Lithium Metal Anodes through Ultrathin Atomic Layer Deposition Surface Treatments. *Chemistry of Materials* **27**, 6457–6462 (2015).
65. Wang, L. *et al.* Li metal coated with amorphous Li₃PO₄ via magnetron sputtering for stable and long-cycle life lithium metal batteries. *Journal of Power Sources* **342**, 175–182 (2017).
66. Lin, D. *et al.* Conformal Lithium Fluoride Protection Layer on Three-Dimensional Lithium by Nonhazardous Gaseous Reagent Freon. *Nano Letters* **17**, 3731–3737 (2017).
67. Pang, Q., Liang, X., Shyamsunder, A. & Nazar, L. F. An In Vivo Formed Solid Electrolyte Surface Layer Enables Stable Plating of Li Metal. *Joule* **1**, 871–886 (2017).
68. Liang, J. *et al.* In Situ Li₃PS₄ Solid-State Electrolyte Protection Layers for Superior Long-Life and High-Rate Lithium-Metal Anodes. *Advanced Materials* **30**, 1804684 (2018).
69. Chi, S.-S., Liu, Y., Song, W.-L., Fan, L.-Z. & Zhang, Q. Prestoring Lithium into Stable 3D Nickel Foam Host as Dendrite-Free Lithium Metal Anode. *Advanced Functional Materials* **27**, 1700348 (2017).
70. Jin, S. *et al.* High Areal Capacity and Lithium Utilization in Anodes Made of Covalently Connected Graphite Microtubes. *Advanced Materials* **29**, 1700783 (2017).
71. Lin, D. *et al.* Three-dimensional stable lithium metal anode with nanoscale lithium islands embedded in ionically conductive solid matrix. *Proceedings of the National Academy of Sciences* **114**, 4613–4618 (2017).

72. Liu, W., Lin, D., Pei, A. & Cui, Y. Stabilizing Lithium Metal Anodes by Uniform Li-Ion Flux Distribution in Nanochannel Confinement. *Journal of the American Chemical Society* **138**, 15443–15450 (2016).
73. Manthiram, A., Fu, Y., Chung, S.-H., Zu, C. & Su, Y.-S. Rechargeable Lithium–Sulfur Batteries. *Chemical Reviews* **114**, 11751–11787 (2014).
74. Girishkumar, G., McCloskey, B., Luntz, A. C., Swanson, S. & Wilcke, W. Lithium–Air Battery: Promise and Challenges. *The Journal of Physical Chemistry Letters* **1**, 2193–2203 (2010).
75. Zhang, Y. *et al.* High-capacity, low-tortuosity, and channel-guided lithium metal anode. *Proceedings of the National Academy of Sciences* **114**, 3584–3589 (2017).
76. Liu, L. *et al.* Uniform Lithium Nucleation/Growth Induced by Lightweight Nitrogen-Doped Graphitic Carbon Foams for High-Performance Lithium Metal Anodes. *Advanced Materials* **30**, 1706216 (2018).
77. Liang, Z. *et al.* Polymer Nanofiber-Guided Uniform Lithium Deposition for Battery Electrodes. *Nano Letters* **15**, 2910–2916 (2015).
78. Xie, K. *et al.* Toward Dendrite-Free Lithium Deposition via Structural and Interfacial Synergistic Effects of 3D Graphene@Ni Scaffold. *ACS Applied Materials & Interfaces* **8**, 26091–26097 (2016).
79. Ye, H. *et al.* Stable Li Plating/Stripping Electrochemistry Realized by a Hybrid Li Reservoir in Spherical Carbon Granules with 3D Conducting Skeletons. *Journal of the American Chemical Society* **139**, 5916–5922 (2017).
80. Sun, Z. *et al.* Robust Expandable Carbon Nanotube Scaffold for Ultrahigh-Capacity Lithium-Metal Anodes. *Advanced Materials* **30**, 1800884 (2018).

81. Zhang, R. *et al.* Coralloid Carbon Fiber-Based Composite Lithium Anode for Robust Lithium Metal Batteries. *Joule* **2**, 764–777 (2018).
82. Shi, P. *et al.* Lithiophilic LiC₆ Layers on Carbon Hosts Enabling Stable Li Metal Anode in Working Batteries. *Advanced Materials* **31**, 1807131 (2019).
83. Lin, D. *et al.* Fast galvanic lithium corrosion involving a Kirkendall-type mechanism. *Nature Chemistry* **11**, 382–389 (2019).
84. Anasori, B., Lukatskaya, M. R. & Gogotsi, Y. 2D metal carbides and nitrides (MXenes) for energy storage. *Nature Reviews Materials* **2**, (2017).
85. Naguib, M. *et al.* Two-Dimensional Nanocrystals Produced by Exfoliation of Ti₃AlC₂. *Advanced Materials* **23**, 4248–4253 (2011).
86. Er, D., Li, J., Naguib, M., Gogotsi, Y. & Shenoy, V. B. Ti₃C₂ MXene as a High Capacity Electrode Material for Metal (Li, Na, K, Ca) Ion Batteries. *ACS Applied Materials & Interfaces* **6**, 11173–11179 (2014).
87. Naguib, M. *et al.* MXene: a promising transition metal carbide anode for lithium-ion batteries. *Electrochemistry Communications* **16**, 61–64 (2012).
88. Lukatskaya, M. R. *et al.* Cation Intercalation and High Volumetric Capacitance of Two-Dimensional Titanium Carbide. *Science* **341**, 1502–1505 (2013).
89. Zhang, D., Wang, S., Li, B., Gong, Y. & Yang, S. Horizontal Growth of Lithium on Parallely Aligned MXene Layers towards Dendrite-Free Metallic Lithium Anodes. *Advanced Materials* **31**, 1901820 (2019).
90. Chen, X., Shang, M. & Niu, J. Inter-layer-calated Thin Li Metal Electrode with Improved Battery Capacity Retention and Dendrite Suppression. *Nano Lett.* **20**, 2639–2646 (2020).

91. Gao, Y. *et al.* Polymer–inorganic solid–electrolyte interphase for stable lithium metal batteries under lean electrolyte conditions. *Nat. Mater.* **18**, 384–389 (2019).
92. Fan, X. *et al.* Fluorinated solid electrolyte interphase enables highly reversible solid-state Li metal battery. *Sci. Adv.* **4**, eaau9245 (2018).
93. Pathak, R. *et al.* Fluorinated hybrid solid-electrolyte-interphase for dendrite-free lithium deposition. *Nat Commun* **11**, 93 (2020).
94. Suo, L. *et al.* Fluorine-donating electrolytes enable highly reversible 5-V-class Li metal batteries. *Proc Natl Acad Sci USA* **115**, 1156–1161 (2018).
95. Zhu, Y., He, X. & Mo, Y. Strategies Based on Nitride Materials Chemistry to Stabilize Li Metal Anode. *Adv. Sci.* **4**, 1600517 (2017).
96. Li, Y. *et al.* Robust Pinhole-free Li₃N Solid Electrolyte Grown from Molten Lithium. *ACS Central Science* **4**, 97–104 (2018).
97. Huang, W., Wang, H., Boyle, D. T., Li, Y. & Cui, Y. Resolving Nanoscopic and Mesoscopic Heterogeneity of Fluorinated Species in Battery Solid-Electrolyte Interphases by Cryogenic Electron Microscopy. *ACS Energy Lett.* **5**, 1128–1135 (2020).
98. Gao, Y. *et al.* Low-temperature and high-rate-charging lithium metal batteries enabled by an electrochemically active monolayer-regulated interface. *Nat Energy* **5**, 534–542 (2020).
99. Rupich, M. W. & Abraham, K. M. Characterization of Reactions and Products of the Discharge and Forced Overdischarge of Li/SO₂ Cells. **129**, 5 (1982).
100. Lv, Y., Shang, M., Chen, X. & Niu, J. Double-Net Enclosed Sulfur Composite as a New Cathode in Lithium Sulfur Batteries. *The Journal of Physical Chemistry C* **123**, 17719–17727 (2019).

101. Zhao, Q., Stalin, S., Zhao, C.-Z. & Archer, L. A. Designing solid-state electrolytes for safe, energy-dense batteries. *Nat Rev Mater* **5**, 229–252 (2020).
102. Han, F. *et al.* High electronic conductivity as the origin of lithium dendrite formation within solid electrolytes. *Nature Energy* **4**, 187–196 (2019).
103. Schmidt, R. D. & Sakamoto, J. In-situ, non-destructive acoustic characterization of solid state electrolyte cells. *Journal of Power Sources* **324**, 126–133 (2016).
104. Sharafi, A., Meyer, H. M., Nanda, J., Wolfenstine, J. & Sakamoto, J. Characterizing the Li–Li₇La₃Zr₂O₁₂ interface stability and kinetics as a function of temperature and current density. *Journal of Power Sources* **302**, 135–139 (2016).
105. Ebadi, M., Marchiori, C., Mindemark, J., Brandell, D. & Araujo, C. M. Assessing structure and stability of polymer/lithium-metal interfaces from first-principles calculations. *J. Mater. Chem. A* **7**, 8394–8404 (2019).
106. Wang, C. *et al.* Differentiated Lithium Salt Design for Multilayered PEO Electrolyte Enables a High-Voltage Solid-State Lithium Metal Battery. *Adv. Sci.* **6**, 1901036 (2019).
107. Yu, X. A Stable Thin-Film Lithium Electrolyte: Lithium Phosphorus Oxynitride. *Journal of The Electrochemical Society* **144**, 524 (1997).
108. Neudecker, B. J., Dudney, N. J. & Bates, J. B. “Lithium-Free” Thin-Film Battery with In Situ Plated Li Anode. *Journal of The Electrochemical Society* **147**, 517 (2000).
109. Wang, B. Characterization of Thin-Film Rechargeable Lithium Batteries with Lithium Cobalt Oxide Cathodes. *Journal of The Electrochemical Society* **143**, 3203 (1996).
110. Dudney, N. J. *et al.* Nanocrystalline Li_xMn₂X_yO₄ Cathodes for Solid-State Thin-Film Rechargeable Lithium Batteries. *Journal of The Electrochemical Society* **10** (1999).

111. Neudecker, B. J., Zuhr, R. A. & Robertson, J. D. Lithium Manganese Nickel Oxides $\text{Li}(\text{MnNi}_{1-x})_2\text{O}_2$. *J. Electrochem. Soc.* **145**, 9 (1998).
112. Li, J. *et al.* An Artificial Solid Electrolyte Interphase Enables the Use of a $\text{LiNi}_{0.5}\text{Mn}_{1.5}\text{O}_4$ 5 V Cathode with Conventional Electrolytes. *Advanced Energy Materials* **3**, 1275–1278 (2013).
113. Liu, W. *et al.* Artificial Solid Electrolyte Interphase Layer for Lithium Metal Anode in High-Energy Lithium Secondary Pouch Cells. *ACS Applied Energy Materials* **1**, 1674–1679 (2018).
114. Lacivita, V. *et al.* Resolving the Amorphous Structure of Lithium Phosphorus Oxynitride (Lipon). *J. Am. Chem. Soc.* **140**, 11029–11038 (2018).
115. Ma, C. *et al.* Interfacial Stability of Li Metal–Solid Electrolyte Elucidated via in Situ Electron Microscopy. *Nano Letters* **16**, 7030–7036 (2016).
116. Zhu, Y., He, X. & Mo, Y. Origin of Outstanding Stability in the Lithium Solid Electrolyte Materials: Insights from Thermodynamic Analyses Based on First-Principles Calculations. *ACS Applied Materials & Interfaces* **7**, 23685–23693 (2015).
117. Richards, W. D., Miara, L. J., Wang, Y., Kim, J. C. & Ceder, G. Interface Stability in Solid-State Batteries. *Chemistry of Materials* **28**, 266–273 (2016).
118. Zhu, Y., He, X. & Mo, Y. First principles study on electrochemical and chemical stability of solid electrolyte–electrode interfaces in all-solid-state Li-ion batteries. *Journal of Materials Chemistry A* **4**, 3253–3266 (2016).
119. Schwöbel, A., Hausbrand, R. & Jaegermann, W. Interface reactions between LiPON and lithium studied by in-situ X-ray photoemission. *Solid State Ionics* **273**, 51–54 (2015).

CURRICULUM VITAE

Xi Chen

Place of birth: Kunming, Yunnan, China

EDUCATION

Ph.D. Sep.2016-present Advisor: Junjie Niu

Materials Science and Engineering (Major), Mechanical Engineering (Minor)

CEAS, University of Wisconsin - Milwaukee

Dissertation Title: Developing highly reversible Li metal anode with mossy/dendritic Li suppression in high energy density batteries

M.S. Jan.2014-Aug.2016 Advisor: Junjie Niu

Materials Science and Engineering (Major)

CEAS, University of Wisconsin - Milwaukee

B.S. Sep.2009-Jun.2013

Materials Science and Engineering (Major)

College of Materials Science and Engineering, Chongqing University, China

RESEARCH INTERESTS

Li metal anodes, *in-situ* TEM, Sn/SnO₂ anode, characterization of SEI, application of MXene in batteries, sulfide based solid state electrolyte, Li-S batteries

PUBLICATIONS

Chen, X., Shang, M. & Niu, J. Inter-layer-calated thin Li metal electrode with improved battery capacity retention and dendrite suppression. *Nano Letter*, 2020, 20, 2639–2646.

Chen, X., Lv, Y., Shang, M. & Niu, J. Ironing Controllable Lithium into Lithiotropic Carbon Fiber Fabric: A Novel Li-Metal Anode with Improved Cyclability and Dendrite Suppression. *ACS Applied Materials & Interfaces*, 2019, 11, 21584–21592.

Shang, M., **Chen, X.** & Niu, J. A Fast Charge/Discharge and Wide-Temperature Battery with a Germanium Oxide Layer on a Ti₃C₂ MXene Matrix as Anode. *ACS Nano*, 2020, 14, 3678–3686.

Kang, S., **Chen, X.** & Niu, J. Sn Wears Super Skin: A New Design for Long Cycling Batteries. *Nano Letter*, 2018, 18, 467–474.

Liu, J., **Chen, X.**, Kim, J., Zheng, Q., Ning, H., Sun, P., Huang, X., Liu, J., Niu, J. & Braun, P. High Volumetric Capacity Three-Dimensionally Sphere-Caged Secondary Battery Anodes. *Nano Letter*, 2016, 16, 4501–4507.

Lv, Y., Shang, M., **Chen, X.**, Nezhad, P. S. & Niu, J. Largely Improved Battery Performance Using a Microsized Silicon Skeleton Caged by Polypyrrole as Anode. *ACS Nano*, 2019, 13, 12032–1204.

Lv, Y., Shang, M., **Chen, X.** & Niu, J. Double-Net Enclosed Sulfur Composite as a New Cathode in Lithium Sulfur Batteries. *Journal Physical Chemistry C*, 2019, 123, 17719–17727.

Liu, J., Lin, X., **Chen, X.**, Shen, Z., Chi, M., Niu, J., Zhang, H., Huang, J. & Li, J. A novel tin hybrid nano-composite with double nets of carbon matrixes as a stable anode in lithium ion batteries. *Chemical Communication*, 2017, 53, 13125–13128.

Liu, J., Lin, X., Han, T., Lu, Q., Long, J., Zhang, H., **Chen, X.**, Niu, J., & Li, J. An Artificial Sea Urchin with Hollow Spines: Improved Mechanical and Electrochemical Stability in High-Capacity Li-Ge Batteries. *Nanoscale*, 2020, 12, 5812–5816.

Liu, J., Zhou, P., Zhang, W., **Chen, X.**, Huang, J., Li, J., Chi, M. & Niu, J. An all-in-one Sn–Co alloy as a binder-free anode for high-capacity batteries and its dynamic lithiation in situ. *Chemical Communication*, 55, 529–532 (2019).

Ding, Y., Han, T., Zhang, H., Cheng, M., Wu, Y., **Chen, X.**, Chi, M., Niu, J., & Liu, J. A Hollow Co₂SiO₄ Nanosheet Li-Ion Battery Anode with High Electrochemical Performance and Its Dynamic Lithiation/Delithiation Using in Situ Transmission Electron Microscopy Technology. *Applied Surface Science*, 2019, 490, 510–515.

RESEARCH EXPERIENCES

Research/Teaching Assistant for Professor Junjie Niu, CEAS, UW-Milwaukee, Jan. 2015-present.

Selected projects participated:

Developing highly reversible Li metal anode with mossy/dendritic Li suppression in high energy density batteries.

Developing Li metal electrode for both liquid LIBs and all-solid-state lithium batteries by creating artificial SEI buffer layer on Li metal.

A rational design for ultra-long cycling Sn/SnO₂ anode in LIBs.

Nickel-rich layered transition metal oxide high energy density cathode for LIBs.

Observation of electrode lithiation process and interfacial evolution in lithium-ion battery Sn anode by *in-situ* TEM technique.

Rational design of cathode materials for high performance lithium-sulfur batteries.

First author manuscripts under preparation: **Chen, X.**, Shang, M. & Niu, J. A scalable electrochemo-mechanical stable artificial SEI design for Li metal anode with enhanced batteries performance.

Visiting Students for Senior Staff Scientist Miaofang Chi, Oak Ridge National Laboratory, Jun. – Aug. 2017, Jun. – Aug. 2018.

Project involved:

In-situ S/TEM and EELS analysis of the interfacial evolution between metallic lithium anode and LiPON solid electrolyte during electrochemical cycling.

Paper submitted:

Hood, Z.*, **Chen, X.***(Co-first author), Liu, X., Sacci, R., Dudney, N., Niu, J. & Chi, M. Elucidating Interfacial Stability between Lithium Metal Anode and LiPON via *In-Situ* Electron Microscopy. (3rd round revision at *Nano Letter*)

TEACHING EXPERIENCES

Teaching Assistant for Engineering Materials Lab at UWM

Teaching Assistant for Materials and Processes in Manufacturing Lab at UWM

SKILL

Familiar with conventional electrochemical characterization: CV, EIS, LSV, GITT

Experienced on materials characterization methods: TEM (JEOL JEM-ARM200CF 200 kV STEM/TEM (long term user at UIC and Northwestern University)), aberration-corrected FEI Titan S 80-300 TEM/STEM (Trained at ORNL microscopy group), JEOL-2010F TEM, Hitachi H-9000NAR 300kV TEM); Nanofactory STM-TEM *in-situ* holder (trained by Dr.Kushima at MIT), Protonchips *in-situ* heating holder; XPS (Thermo Scientific ESCALAB 250Xi); SEM (Hitachi S-4800); XRD (Bruker D8 Discover); Raman (HORIBA XploRA Plus)

AWARDS

UW-Milwaukee Chancellor Award Scholarship-Spring 2020

UW-Milwaukee Chancellor Award Scholarship-Spring 2014